SYNTHESIS AND CHARACTERIZATION OF $Gd_5Si_2Ge_2$-Al COMPOSITE FOR AUTOMOBILE APPLICATIONS

A Thesis

by

BRADY CURTIS BARKLEY

Submitted to the Office of Graduate Studies of
Texas A&M University
in partial fulfillment of the requirements for the degree of

MASTER OF SCIENCE

May 2010

Major Subject: Mechanical Engineering

SYNTHESIS AND CHARACTERIZATION OF $Gd_5Si_2Ge_2$-Al COMPOSITE FOR AUTOMOBILE APPLICATIONS

A Thesis

by

BRADY CURTIS BARKLEY

Submitted to the Office of Graduate Studies of
Texas A&M University
in partial fulfillment of the requirements for the degree of

MASTER OF SCIENCE

Approved by:

Chair of Committee,	Hong Liang
Committee Members,	Timothy Jacobs
	Sean McDeavitt
Head of Department,	Dennis O'Neal

May 2010

Major Subject: Mechanical Engineering

ABSTRACT

Synthesis and Characterization of $Gd_5Si_2Ge_2$-Al Composite for Automobile
Applications. (May 2010)
Brady Curtis Barkley, B.S., Oklahoma Christian University
Chair of Advisory Committee: Dr. Hong Liang

This thesis research synthesizes a new class of composite materials and investigates their properties, performance, and potential applications. The new materials that are multi-phase and multifunctional are considered for use in car cooling systems, internal combustion engine waste-heat-power generators, and engine crack healing which are major problems plaguing the auto industry. This research uses primarily experimental approaches to study the magnetocaloric compound, $Ge_5Si_2Ge_2$ (GSG), that has large strain effects. Such a material was formed into a composite using Al as a substrate. The newly developed composite, GSG-Al, is the first material of its kind that possesses self-healing effects in cracks.

X-ray diffraction was used to determine the crystal structures that existed within the material. It is found that the sintering process used to create the composite caused the formation of GdAlGe that is a magnetic compound with a high Curie temperature. The GSG-Al has a wide variety of crystal structures, ranging from face centered cubic for aluminum phases to monoclinic and orthorhombic phases for GSG. The discovery of GdAlGe confirmed that α-ThSi-type tetragonal and YAlGe-type orthorhombic crystal structures existed. Transmission electron microscopy (TEM) was used to analyze the wear debris collected during tribo-testing. The debris were also analyzed using energy-dispersive X-ray spectroscopy (EDS) for chemical analysis.

The GSG-Al was put through tribological studies at several different temperatures to determine the thermal effects on the composite. The GSG-Al, although found to be ductile, showed high resistance to wear when compared to a common aluminum alloy, Al 6061-T651. The wear rate decreased with increasing temperature when the temperature was increased from the room temperature to 150°C. Results showed that with GSG, the composite did not show cracking common in Al alloys. This was due to the unique thermal expansion properties of the GSG-Al. The phase transformation induced a significant volume expansion in the material and thus a giant strain effect.

This research opens new approaches in energy conversion and improving efficiency of automobile engines. The composite developed here is important for future scientific investigation in the area of multifunctional materials as well as materials that exhibit self-healing tendencies.

ACKNOWLEDGEMENTS

I would like to thank my committee chair, Dr. Hong Liang, and my committee members, Dr. Timothy Jacobs and Dr. Sean McDeavitt, for their guidance and time so that this thesis could be completed.

Special thanks go to the students in my research group for all of their assistance and support in performing the experiments, and aiding me in my thought processes in the analysis of different properties and discoveries. Specifically, I would like to thank Michael Cleveland for creating the samples of GSG to use in formation of the composites under study in this paper and performing XRD scans. I would like to thank Subrate Kundu and Huisung Yun for performing TEM and EDS studies on my samples. I would like to thank Rodrigo Cooper for his aid in performing data acquisition during thermal expansion tests and for proofreading my thesis. I would like to thank David Huitink for proofreading my thesis and offering valuable insights. I would like to thank Scott McCall from Lawrence Livermore National Laboratory for performing the magnetic tests on the GSG-Al and GSG samples.

I would like to thank my family for their unwavering support of my studies and their guidance of me to this point in my life. It is because of them that I am able to attend Texas A&M University and because of them that I have been successful. Finally, I would like to thank my Lord Jesus Christ for His guidance in my life and the burdens that He has carried for me as I walked through it. May this paper be a modest tribute to His Name.

NOMENCLATURE

GSG	Gadolinium Silicon Germanium ($Gd_5Si_2Ge_2$)
GSG-Al	Gadolinium Silicon Germanium and Aluminum Composite
XRD	X-ray Diffraction
AlGdGe or GdAlGe	Aluminum Gadolinium Germanium
TEM	Transmission Electron Microscope
EDS	Energy-Dispersive X-ray Spectroscopy
SQUID	Superconducting Quantum Identification Device
MCE	Magnetocaloric Effect
TE	Thermoelectric
IR	Infrared
LED	Light Emitting Diode
DAQ	Data Acquisition
AC	Air Conditioning
IC	Internal Combustion
FSMA	Ferromagnetic Shape-Memory Alloys

TABLE OF CONTENTS

Page

CHAPTER

LIST OF FIGURES

Page

Page

Page

LIST OF TABLES

CHAPTER I

INTRODUCTION

This chapter serves as an introduction to issues considered in automobiles such as power generation, cooling systems, wear, and fatigue. In addition, it will discuss multifunctional materials that can potentially be used in automobile applications. Some basics about such materials like their functions and uniqueness will be provided.

1.1 Automobiles: Cooling Systems, Efficiency, Wear, and Fatigue

Automobiles are an important part of the world economy. The internal combustion (IC) engines within the cars are a mechanical marvel due to their influence on how humankind has progressed from the 19th century. [1,2] The IC engine, although very important, is not highly efficient. The problem that all IC engines have in common is energy lost in the form of waste heat. Waste heat poses two problems: cooling and efficiency.[3] Engines do run better at elevated temperatures, but cooling systems are needed to remove excess heat so that the engine will not be damaged. [4] Engine cooling has long been controlled by liquid or gas cooling systems and new coolants and thermoelectric devices are now being developed. [5,6] The other problem with waste heat is the decreased fuel economy of the vehicle. [3] In order to obtain an understanding of these issues, a review in methods of reducing the waste heat will be provided here.

A common issue affecting IC engines is material cracking as fatigue failure. [7-10]

This thesis follows the style of the Journal of Applied Physics.

IC engines have many moving parts that are put through thousands of loading cycles. Revolutionary changes are always being researched in materials. In this chapter, an introduction to materials that exhibit high strain properties is provided. This knowledge serves as the basis for the materials development carried out in this research.

1.1.1 Engine Cooling Systems and Efficiency

This section will discuss issues with automobile efficiencies and methods of heat removal from the car. Automobile engines are a main focus for efficiency improvements due to the vast amounts of cars on the road and diesel engines involved in powering equipment. Only a small fraction of the chemical energy within the gasoline/diesel is able to be converted within the engine to mechanical energy. [2,3] This is due to energy losses in the form of waste heat, piston friction, and inefficient air-fuel ratios. [3] Improvements have been made to both diesel and gasoline engines in order to increase engine efficiency. [3,7,8] Each system within a car takes energy from the limited amount converted from the fuel.

In analysis of average automobiles today, 40% of the fuel energy is being wasted through the exhaust as unspent fuel and waste heat, 30% of the energy going toward cooling the engine, 5% of the energy being used up by engine friction and radiated heat, and 25% of energy going towards propulsion and electric systems. [3] Since 30% of the fuel's energy goes toward cooling the engine, better methods of cooling should be considered in order to divert more energy away from cooling and into the car's propulsion.

Most cars today feature a liquid cooling system. [9] The liquid cooling system involves a process of pumping a liquid, often a refrigerant, throughout the engine and then into a finned radiator. [9,10] The radiator, pictured in Figure 1, is used to exchange the refrigerant heat with the air flowing over the tubes and fins of the radiator.

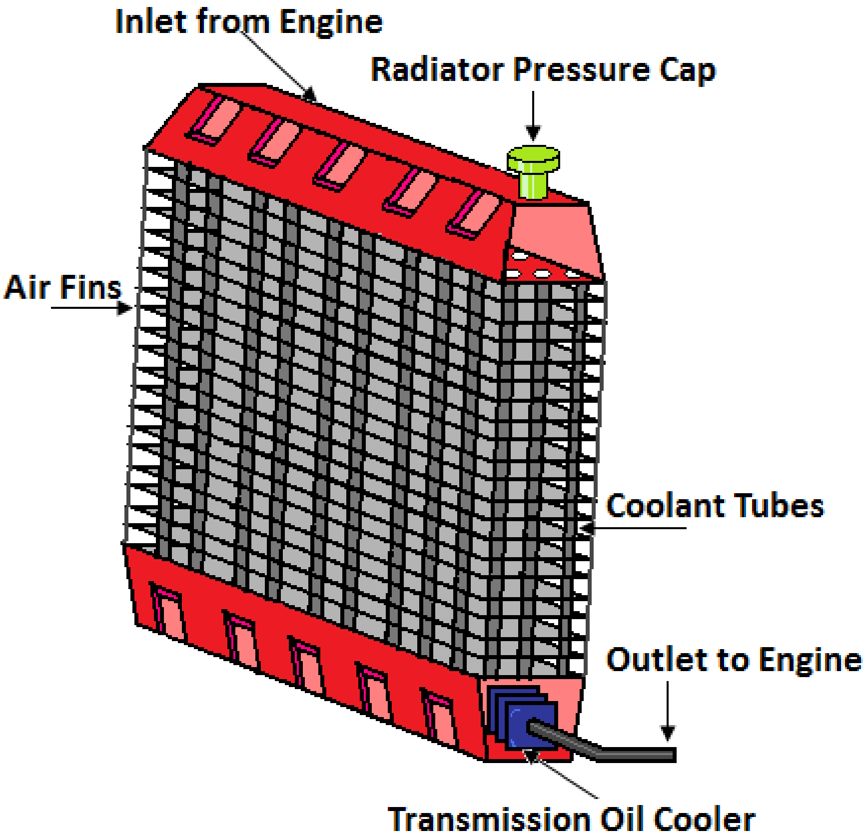

Figure 1 Schematic of radiator used as a part of an automotive liquid cooling system

The refrigerant is cooled in the system and repeats the process of removing heat from the engine. [10] Air flow can either be accomplished by the movement of the car and the air passing through the radiator at the same velocity as the car or by being brought into car via a fan behind the radiator. [10-12] Air cooling is another cooling system that is now less common. Such a system relies completely on the air flowing over the engine and not on other fluids specialized in absorbing heat. An air cooled engine is characterized by aluminum finned motor components that direct heat out of the core portions of the engine and out to the surface. The fins provide an enlarged surface area where convection heat transfer can be better utilized to cool the engine. Air cooled engines are more common in motorcycles and yard equipment. [13]

Engines function better in warmer temperatures than in cold. However, finding the “Goldilocks Zone” of engine temperature is an important part in achieving optimal engine efficiency. [4,14,15] Cold engines do not burn sufficient fuel in the combustion chambers and often cause sludge to form within the crankcase. [16,17] Most cars tend to function well around 100°C although the exhaust gas in the engine is far hotter at around 500°C. [3,4,17] Liquid-cooled engines have many advantages, but they do not make the engine cool homogeneously. [10] The fluid flow may not contact and remove all hot spots from the engine and if the coolant’s boiling point is reached, the coolant may boil and evaporate. Boiling coolant may cause vapor to inhibit the flow of the fluid to the hot spot exacerbating the problem. [4] Typically an easy fix would be an adjustment to the coolant, but the coolant cannot be brought to all areas of the engine. [5,6] Having high temperature extremes can harm the engine and shorten the life of its parts and induce thermal fatigue. [18,19]

Research has been done on improving the old engine cooling technologies. Focus has been ranged from coolant types to different engine materials. [5,6,18] Nanofluids for use as engine coolants are among the recent new technologies to be developed. [6] The research focuses on the effect of the nanoparticle's shape, size, additives, and base fluids on the thermal conductivity and viscosity of the fluid so that an improved heat transfer coefficient can be obtained. [6] Effective heat transfer would allow for the fluid to absorb more heat from the engine in fewer cycles. As the number of cycles decrease, the amount of fuel saved by the engine increases. The nanofluid composed of boehmite alumina in an EG-H_2O solution was studied for its thermal conductivity and viscosity properties as a function of particle shape, base fluids, and pH. [6] Diamond nanofluids have also been investigated for their cooling effects due to diamond having the highest thermal transport capacity in nature. [5] It was found that increasing the concentration of the nano-particles in a solution greatly enhanced the coolant's thermal transport capabilities. [5] Incorporating diamond and copper nanoparticles into coolants for heat sinks has shown promising results. The particles both decreased the thermal resistance and the thermal gradient between the sink and the coolant. [20] The nanofluids show promise as highly efficient coolants for engines. [5,20]

Another form of cooling system is rarely, if at all, used in cars and is known as a Peltier device. The Peltier device is a mechanism that uses the thermoelectric effect. [21,22] The details of this effect are described in detail in section 1.1.5.1. The Peltier device has the ability to use a thermoelectric semiconductor and a power source in order to make one side of the device warm and the other side cool by forcing the flow of electrons in a material to transfer heat in one direction determined by the direction of current.[21-23] The problem with this type of device is that it is very inefficient with a Carnot efficiency of around 5-10%, while vapor compression cooling systems are closer to 50% efficient when the coefficient of performance is changed to the Carnot scale.[22]

1.1.2 Organic Rankine Cycle Power Generation

The Rankine cycle has long been used as the appropriate cycle for steam power plants powered by coal.[24] The cycle consists of a liquid that is pumped into a boiler. Steam then leaves the boiler and rotates a turbine connected to an electric generator. Once steam has passed through the generator, the steam condenses back to a liquid in a condenser. The cycle then begins again with the liquid being pumped back into the boiler.[7,25] The cycle is shown in Figure 2.

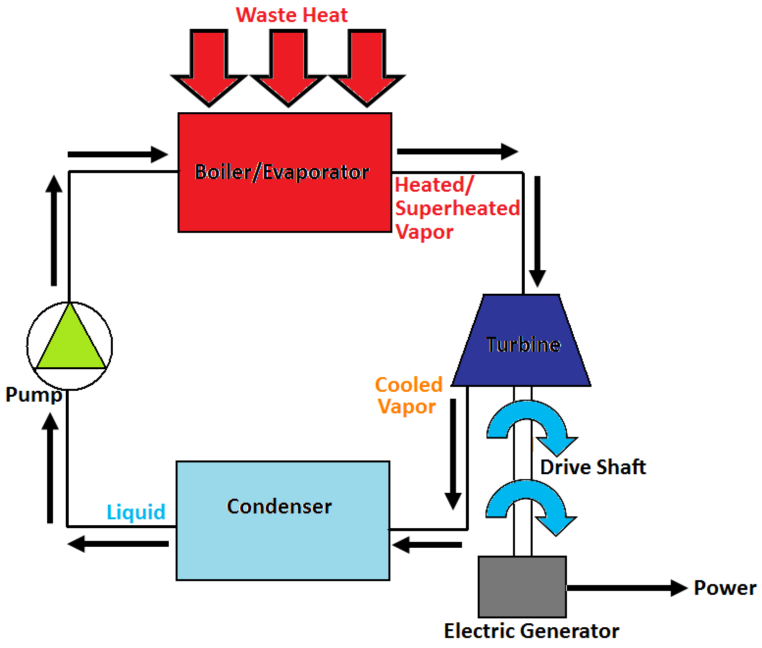

Figure 2 Organic Rankine cycle used to convert waste heat into electricity

The efficiency of this cycle is directly tied to the working fluid since it is the fluid that determines the achievable pressures and temperatures of the steam. Water is the most common fluid used due to its abundance, low cost, and ease of access from rivers and reservoirs. [7,24,26,27]

Waste heat recovery is a big issue for many industries. [28] The problem with the Rankine cycle is that once the steam leaves the turbine, the energy within the fluid is wasted as it cools in the condenser. [28,29] In order to increase the energy absorbed, several industries stack turbines so that once steam leaves one turbine, it enters another one that requires less energy to turn. [24] Eventually the steam reaches a temperature and pressure that is no longer useful; at this point it is condensed back into a liquid. Another form of Rankine cycle is known as the organic Rankine cycle (ORC). [8,27,29,30] This cycle uses organic fluids that boil at lower temperatures than water. [29,31] The low boiling point is important because this cycle can be used to generate work from low temperature heat sources. [26] While coal power plants typically have steam at 165.5 kPa (2400 psi) and 528°C (1000°F), the organic liquids could function at much lower temperatures. [32]

Hydrocarbons and refrigerants are the typical working fluids in the ORC due to their low boiling points. [26,33] The working fluids of an ORC engine are divided into 3 groups: wet, isentropic, and dry. The group of the fluid depends upon the slope of the temperature – entropy plot of the fluid. [26,30] Wet, isentropic, and dry fluids have a negative, infinite, or positive slope respectively. [26] Examples of these T-s diagrams are shown in Figure 3.

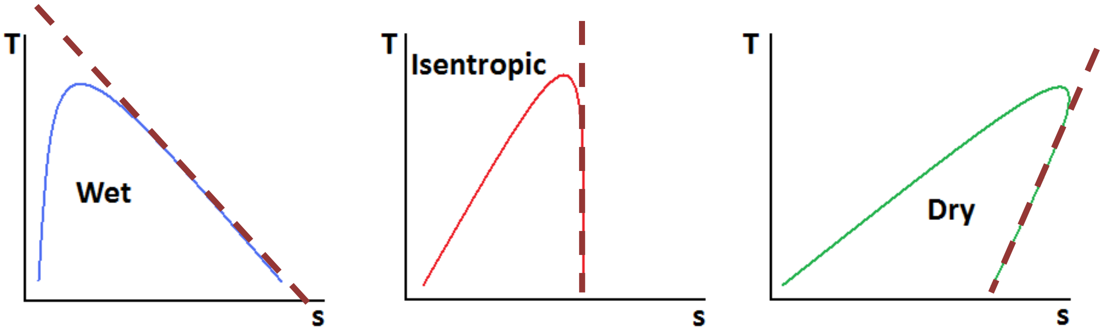

Figure 3 T-s diagrams of wet fluids (left), isentropic fluids (center), and dry fluids (right)

ORC engines run best when they run with dry or isentropic fluids due to them being superheated after isentropic expansion.[8] The superheated fluids will not form droplets and therefore will not harm the turbine blades and will remove the need for a super heater. [26] Hydrocarbons such as toluene and p-xylene have been found to have among the highest potential so far. [26] Choosing the correct fluids along with increasing the temperature gradient improves upon the exergy of the ORC. The efficiency of the ORC engine functions better in the range of temperatures between the inlet waste heat temperature and the fluid condensation temperatures and increases as the critical temperature of the fluid increases. [26]

The use of the ORC to reclaim heat from a car's exhaust is an option, albeit that it adds some potential problems. The addition of a turbine of acceptable power generation will add weight to the car, thus reducing the car's fuel economy. [8] Another problem would be successfully transferring the heat from the exhaust to a boiler. If the transition is done incorrectly, a large amount of heat would be wasted. Further analysis into smaller and more compact ORC engines could be done in order to adapt this technology to automobiles.

1.1.3 Fatigue, Cracking, and Wear in Automobiles

Modern engine designs are substituting aluminum alloys for steel engine blocks and pistons due to aluminum's high strength-to-weight ratio. Since aluminum is 1/3 the density of steel it aids the automobile in fuel economy in weight reduction. [34-38]

In order for an aluminum alloy to be functional as a part of the engine, it needs to exhibit four properties: high toughness, a well determined thermal expansion coefficient, high wear and corrosion resistance, and strength over a broad temperature range (up to

300°C). [18,39] Within a car there are multiple components and materials in constant contact with each other or under cyclic loading. The use of aluminum alloys and composites to aid in engine, transmission, and bearing applications is sought. [18,37] Using aluminum matrix composites involving Si and other metals are being used to increase the wear resistance of the engine components. [18] The U.S. Department of Energy sees wear reduction in automobiles as a step to higher efficiencies with a savings of $120 billion per year if the high wear resistance goals are met. [14] The smallest steps taken to improve upon the wear resistance of the engine components can produce a major effect throughout the world due to the great number of cars on the road today. [14]

The reduction of friction in the interfaces between piston and the engine's cylinder wall poses difficulties due to the complexity and unpredictability of the factors involved in wear. The sliding rate, force, plastic deformation, and roughness are all variables in a difficult equation. [40] Steps are being taken to decrease the wear and friction between the piston ring and cylinder including improved surface coatings, better surface finishes, and surface texture control. [14,36] Tests on aluminum alloys and composites have resulted in the analysis of wear rate as a function of temperature. Aluminum wear rate markedly improves as the temperature increases to around 150°C, but beyond that the primary wear mechanism of the material transitions from abrasive to adhesive and wear is highly exacerbated. [36,41-43] The addition of higher concentrations of Si and other additives is being investigated for wear rate improvement at higher temperatures. [18] Investigations into both hard and soft coatings have shown that they potentially protect the aluminum from wear. [40]

Engine wear is predominantly controlled by the characteristics of the lubricant used. [36,43] Formulation of better lubricants is an important step to reducing friction and wear. A problem exists, however, in the fact that most lubricants in supply today are formulated for use with steel engine components rather than with aluminum or magnesium alloyed engine parts. [14] If aluminum engine blocks are to be made the dominant form, specialized lubricants need to be made.

The problem with using aluminum to make an engine block or piston lies in aluminum's susceptibility to fatigue and cracking over relatively short loading cycles and smaller loads than steel. [36,42,44] In order to overcome this drawback, aluminum is alloyed with copper in order to improve its fatigue strength properties. [14] Introduction of aluminum matrix composites has also aided in the reduction of cracking in the engine parts and through the use of heat treatment techniques as well as reinforcement, the aluminum alloys and composites are showing signs of improved resilience to fatigue. [18,44]

1.1.4 Giant Strain Effect

High strain has been detected in a large variety of materials. The large strain is typically confined within a particular temperature range, voltage, or magnetic field. Magnetocaloric materials, ferromagnetic shape-memory alloys, piezoelectric materials, and materials with large thermal expansion coefficients all exhibit high amounts of strain.[45-53] Thermal expansion for many materials is a mostly linear trend with increasing temperature. The linear trend is more prominent at higher temperatures and degrades at lower temperatures. [48,50,52,53] Some materials experience a negative thermal expansion coefficient due to compression or contraction with increasing temperature. [54] There are, however, several types of materials that experience a jump in their expansion due to a phase change within the material. The composite ternary compounds, $La_{0.7}Ca_{0.3-x}Sr_xCrO_3$, for example experience a phase changes brought on by thermal gradients that cause large jumps in the strain in the material. [50] The phase shifts and expansion are dependent upon the value of x. $Rb_4LiH_3(SO_4)_4$ and $K_4LiH_3(SO_4)_4$ also experience large thermal expansion coefficients and change from isomorphic crystal structures at room temperatures and experience ferroelastic phase transitions at lower temperatures. [52]

Magnetocaloric materials can exhibit high strain due to two reasons: magnetostriction and phase changes. [48,55,56] Magnetostriction is the expansion and strain in a material due to the movement and alignment of the magnetic moments in a material when subject to an external magnetic field. [49] Phase changes on the other hand can be related to both the temperature and the magnetic field and thus magnetocaloric materials can also be greatly affected by thermal expansion. [48] When both magnetostriction due to paramagnetic-ferromagnetic shifts and phase changes occur at the same temperature or transition point, a giant magnetocaloric effect occurs and induces substantial strain in the material. [48] Magnetocaloric materials will be discussed in detail later on.

Materials can exhibit strain under a magnetic field even without being magnetocaloric. NiMnGa experiences a strain of 9.5% at ambient temperature when a magnetic field is applied to it. [57] This type of material forms another class of material beyond the magnetically controlled magnetostrictives that are seen in magnetocaloric materials. NiMnGa is a ferromagnetic shape-memory alloy (FSMA) and can thus return to its origin shape once the magnetic field is cut-off. [46] In contrast to magnetostrictive materials, the strain is tied to the crystal structure and not the direction of magnetization. Magnetostrictive materials exhibit strain as the magnetization causes magnetic moment rotation relative to the crystal structure. [46] Both material classes do rely on temperature, however, each is activated at its own distinct type: Curie temperature for magnetostrictive and martinsitic temperature for FSMA. [46]

Piezoelectric materials are materials that can change their dimensions based on the input voltage or change in output voltage based on their dimensional changes. [45,58] A model of a piezoelectric material is shown in Figure 4.

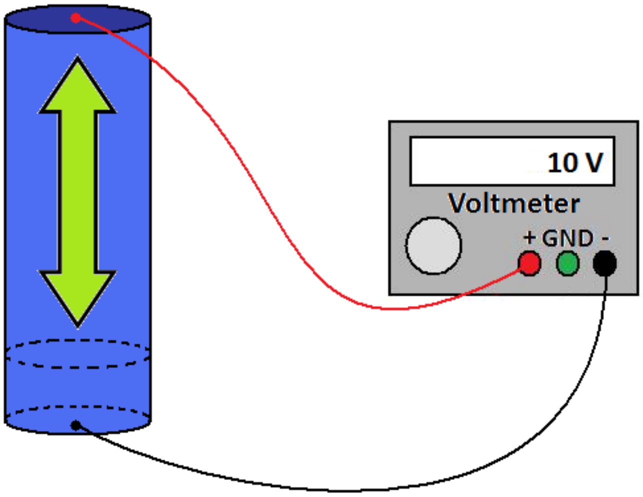

Figure 4 Example of a piezoelectric material being stretched and compressed and the resulting voltage that this strain generates

There have been wide interests in understanding strain effects and their power generation in sensors and actuators.[58] For example, the piezoelectric effect is reversible and is being used in conjunction with many different forms of materials such as nanowires, plastics, crystals, ceramics, and composites. [58-60] The piezoelectric effect is caused by the movement and alignment of electric dipoles. Dipoles near each other are aligned in Weiss domains and can be further aligned with each other as well as other domains when poled. [59] Poling is where an electric field is applied across the material at high temperatures and the domains of the material align in a particular direction. This will allow for an applied force to create a voltage or for an applied current to produce a strain in the material changing its dimensions. [59] An example of this form of material is a $PbZr_{0.2}Ti_{0.8}O_3$ nanowire. These nanowires have been reported to produce stains of upwards of 4.2% when an electrical current is applied. [61] Piezoelectic materials have been used as actuators and are commonly used as part of the stylus's used in atomic force microscopy (AFM). [45,62]

1.1.5 Multifunctional Materials

Two types of multifunctional materials are investigated in this section. A multifunctional material can bear mechanical loads and stresses and exhibit at least one other performance-linked function. [63] Strong magnetic, electric, thermal, strain, or healing properties are among the possible functions. This section will discuss thermoelectric and magnetocaloric materials.

1.1.5.1 Thermoelectric Materials

This section discusses the theory behind thermoelectric systems and materials. The history of this type of material as well as its possible applications in the automotive industry are discussed in order to differentiate this group of materials from a vastly different form that may be used for similar applications in the areas of engine cooling and power generation.

Thermoelectric materials have been used in several applications, but have had their greatest impacts in space technology. [21,64] The materials are a modification of the technology used in thermocouples. Thermocouples work by using a junction of two different materials to determine the temperature of a certain environment. [65] The process by which thermocouples function is that two different materials generate a voltage upon materials that exhibit predictable and repeatable relationships between the potential changes and the temperature changes. [21,66,67]

The thermoelectric effect can best be understood by observing its function at the atomic level. [66-68] When a material experiences a temperature gradient, the electrons, electron holes, or ions within the material move from the hot side of the material to the cold side. This movement of electrons results in a current being produced in the material. Having two different materials means that two different currents will be produced along the same temperature gradient and connecting these materials would result in a potential across them. [21,67]

Thomas Seebeck discovered the thermoelectric effect in 1821, even though at the time he referred to it as the thermomagnetic effect. [66] Seebeck produced a closed circuit made up of two dissimilar metals that were connected in two locations and placed under similar temperature gradients. When this circuit was brought close to a compass, the needle began to spin. Seebeck noticed that a magnetic field had been created. At that time, however, he did not observe that such a field is created by the electric current produced by the circuit. [66] The scientist Hans Christian Oersted had only determined the link between electricity and magnetism in 1820 and this theory turned the thermomagnetic effect into the thermoelectric effect. [21]

The Seebeck effect is a method of converting a temperature difference in materials into electrical units. [67] In order to determine a voltage created between two different materials connected across a temperature gradient, each material needs to have its Seebeck coefficient determined. The Seebeck coefficient must be found for a combination of two materials and cannot be determined for one material alone. The difference between the Seebeck coefficients of both materials is determined by calculating the electric potential across each material and then dividing it by the temperature gradient. [21] This value is then used for the material set to calculate the voltage in the closed loop. The simplified Seebeck effect equation is as follows [21,67]:

$$V = (S_B - S_A) \cdot (T_2 - T_1) \qquad (1)$$

where V is the voltage across the materials, S_B is the Seebeck coefficient for material B, S_A is the Seebeck coefficient for material A, and T_2 and T_1 are the temperatures at opposing sides of the temperature gradient.

Further research into the thermoelectric effect was conducted in 1834 by Jean-Charles Peltier. [23,66,67] He noticed that when an external current was applied across the thermocouple junction of bismuth and antimony, the junction was cooled and began absorbing heat from its surroundings. [21] This occurred when current passed in one direction; when the current direction was reversed, the junction was heated and began to release the heat to the environment. This anomaly is known as the Peltier effect and is represented by the following equation. [21,67]

$$Q_{Rate} = (\Pi_B - \Pi_A) \cdot I \qquad (2)$$

where Q_{Rate} is the amount of heat absorbed at the junction per unit time, Π (Peltier coefficient) represents the proportionality constant specific to a material that relates the heat rate to current, and I is the current applied across the junction. This effect can best be understood by describing the actions of the electrons. As the electrons flow, they go from an area of higher density to lower density within the material, in effect expanding the material. This expansion results in a temperature change, cooling the material. [23,67] The applied current causes the material to go to a non-equilibrium state. The Peltier effect is driven by the potential of materials absorbing and releasing heat at the junctions. [21]

In 1854, William Thomson (Lord Kelvin) furthered the study of the thermoelectric effect by realizing that if an electric current in a material resulted in only Peltier heating, the Peltier and Seebeck voltages must be equal and linearly proportional to the temperature gradient at the thermocouple junctionsl.[21,66,69] This reasoning, however, is contrary to reality. Thomson thus gathered that there must be a reversible absorption or evolution of heat within a conductor that has a maintained temperature gradient. [21] The Thomson effect is represented by the following equation. [21,67]

$$q = \rho \cdot J_2 - \mu \cdot J \cdot dT/dx \qquad (3)$$

where q is the heat production per unit volume, ρ is the resistivity of the material, μ is the Thomson coefficient, J is the current density, and dT/dx is the temperature gradient along a wire. While $\rho \cdot J^2$ is not reversible, the $\mu \cdot J \cdot dT/dx$ term is reversible. The Thomson effect is unique in that unlike the Seebeck and Peltier effects, the Thomson coefficient can be determined for a single material rather than a combination of two materials. [69]

The Thomson effect can either be positive or negative. A positive Thomson effect is characterized by a material that has a hotter end at a higher potential and a cooler end at lower potential. When an electric current is applied and it moves from the hotter end to the cooler end, the current is moving from a high potential to a low potential, resulting in heat being released from the material. A negative Thomas effect experiences the exact opposite by a material having a higher potential at its cooler end and a lower potential at its hotter end. [66,68] As current moves from the hotter end to the colder end it moves from a low potential to a high potential, resulting in heat being absorbed from the environment. [21]

In order to aid in determining the best materials and material combinations for use as thermoelectric materials, a value known as the coefficient or figure of merit (Z) has been developed. The equation used to determine the combined figure of merit value is shown below. [21,67]

$$Z = (S_1 - S_2)^2 / [(\rho_1 \cdot \Lambda)^{1/2} + (\rho_2 \cdot \Lambda)^{1/2}]^2 \qquad (4)$$

where S1 and S2 are the Seebeck coefficients for the combined materials, ρ is the electrical resistivity, and Λ is the thermal conductivity. Materials that have an adequate thermoelectric effect have a high figure of merit, a large operating temperature range, and metallurgical and thermal characteristics suitable for practical applications. [3] Metals and semiconductors have both been experimented with in order to determine their suitability for different thermoelectric applications. [70] Metals are commonly used in thermocouples; however, they are not seen as being useful for power generation applications. [21,70] For the future of power generation, semiconductors are being seen as having the highest potential. [70] Two types of semiconductors are being studied for their thermoelectric properties: broad-band gap semiconductors and narrow-band gap semiconductors. [21] Broad-band semiconductors are characterized by electron transfer due to itinerant motion of nearly free charged carriers, while narrow-band semiconductors transfer electrons by there being enough thermal energy for the electron to “hop” to the next energy band. The semiconductors are quite different and require different methods of optimizing their figures of merit. [66,68]

An issue that thermoelectric material study needs to consider is phonon drag. Phonon drag is the tendency for phonons to interact with other phonons, electrons, defects, and boundaries. [21] A phonon is a quantum of energy that deals with the vibration modes of a rigid crystal lattice. When phonons interact with parts of the crystal lattice, the mobility of electrons is hindered. Electron hindrance reduces the thermal conductivity of the material and enhances the material's Seebeck coefficient and figure of merit. [66,71] Phonon-electron interaction causes electrons to be pushed to one end of the material and move in a direction opposite the thermal gradient. [21] This push of electrons contributes to the thermoelectric effect that already exists in the material and is most beneficial within a narrow temperature range centered around one-fifth the Debye temperature. Phonon interactions vary by material and by temperature. [65] While phonon-phonon interactions may be dominant at one temperature, photon-electron interactions may be dominant at another. Phonon-electron interactions are more beneficial since electron migration increases current, but this mode tends to fare better at lower temperatures. [21] Increasing the temperature range of these interactions in thermoelectric materials is key to the effect's improvement. [72] Materials that exhibit high phonon interactions are the most promising in their potential for the enhancement of thermoelectric generation. [21]

Thermoelectric generator use and study exploded in the 1950's. The earliest TE generators were used to convert either solar heat or heat from fossil fuel burners into electricity. These generators were inefficient (4%) and generated 100 W. [73] The space industry grew interested in them during this time and saw the advantages of their high energy-to-generator weight ratio since launching heavy generators into space is very expensive. [21] The advantages went beyond mass and due to the absence of moving parts in these generators, reliability is very high. The primary modes of heating these generators are radioisotopes, nuclear reactors, and solar heating. Solar heating is used more in missions that are closer to the sun and within the orbit of Venus.[73] Radioisotope heating has been the most used in the space industry due to the low power requirements of many of the spacecraft made in the past 6 decades. [73] The space industry has produced generators capable of generating several hundred watts all the way to the kilowatt range. TE generators have been further studied with varying heat sources such as fossil fuels and waste heat from automobiles. [21] Recent developments in thermoelectric materials have increased the figure of merit greatly and the rate of the figure's growth has increased by a factor of twenty. The newer materials also have a far broader temperature range. [3,71] Many materials have been studied for their use in thermoelectric generation. Group IV chalcogenides, group V chalcogenides, ternary compounds involving chalcogenides, group I, group V elements, Group III through V compounds, group IV elements, and rare earth chalcogenides have all been studied. [21] Each of the materials has varying figures of merit, phonon interaction abilities, and temperature ranges. Some work well within a large temperature range while some do well in small.

Thermoelectric generators are being used in cars, yet not on a large scale. [74] In order to gain the most energy, a high temperature gradient is preferable. [75] The exhaust gas has the highest temperature in a car and would be preferable as the heat source.

Automobile engine exhaust gas temperature is typically around 500°C, but due to problems stemming from extracting a flowing gas's temperature to the surface of a heat exchanger cause the temperature to be reduced to somewhere between 100°C and 400°C. [3] This temperature range is representative of the high temperature source (T_H) of the TE generator, while the car's radiator coolant serves as the low temperature sink (T_C). [71] Testing of the TE materials known as n-type and p-type skutterudite semiconductors yielded energy conversion efficiencies of 6.7%. [3]

Other TE materials such as thin film-based Bi_2Te_3/Sb_2Te_3 superlattices and $PbSe_{1-x}Te_x/PbTe$ quantum dots have been studied and have been found to yield the highest figures of merit. [3] The trouble with these compounds is that they have steep slopes when their figures of merit are plotted versus temperature and they have a small temperature range. This drawback limits the Carnot efficiency of the use of these materials in a generator to only 19.6%. [3]

TE devices are being studied for several applications. Automotive applications are not limited only to power generation, but cooling as well. [22,66,76] In order to generate power from the waste heat of the car engine, energy must be removed from a heat source and converted to electricity. This absorption of energy decreases the temperature of the engine. If these TE devices are used enough and are tied in to appropriate spots on the engine, the engine's normal cooling system may require less energy. [77] The narrow-band semiconductor known as bismuth telluride is a highly efficient thermoelectric material used for thermoelectric generation as well as cooling. The issue is, however, that bismuth telluride is an efficient thermoelectric material, yet compared to the vapor compression cycle it has a lower efficiency. [78] Two-stage thermoelectric generators have also been considered for the enhancement of the power generation efficiency. [79]

The thermoelectric generation system has several possibilities for use in automobiles and could be used to eliminate many of the parasitic loads that the engine has to endure through its alternator. [68] With the removal of these loads, more power and torque will go into propelling the vehicle rather than powering the cooling system, AC, and other electrical systems in the car. [3] Challenges still exist for TE technology in cars due to the need to evaluate the thermal stability of the TE materials, development of more efficient heat exchangers, integration of TE subsystems into the cars for use in power management, and the need to study the TE generator's effect on fuel economy. [3]

A large issue when it comes to acquiring energy from the waste heat of an engine is exergy. Exergy is the maximum amount of useful work that can be gathered during a process. [24,71,75] This process involves its transition to thermal equilibrium with a heat reservoir or source. As the temperature difference between the high and low temperature reservoirs decreases, the exergy of the system decreases and the ability to do work drops correspondingly. Low temperature energy reclamation is difficult due to inherently low exergy of systems having temperatures close to the surrounding's temperature. Development of better material and systems as well as enlarging the temperature differences between source and sink will have to be done in order to tap more energy from waste heat. [80,81]

1.1.5.2 Magnetocaloric Materials

This section discusses the general theory behind a phenomenon known as the magnetocaloric effect, its current applications, and its potential use as a multifunctional material. The magneto-thermodynamic tendency known as the magnetocaloric effect exhibits interesting property changes as changes occur in temperature, magnetic field, or pressure [82]. Magnetic materials are characterized by having two reservoirs of energy [83]. One such reservoir has phonon excitations that are connected to lattice degrees of freedom. The second energy reservoir consists of magnetic excitations that are connected to spin degrees of freedom. [83] When an external magnetic field is applied, the spin degrees of freedom are highly affected by a reduction in the spin system's disorder. This reduction in disorder results in a reduction in the magnetic entropy of the material. [83] This effect commonly occurs when a magnetic field is applied to a paramagnetic material that is near absolute zero or a ferromagnetic material near the Curie temperature. [84] A paramagnetic material is one that exhibits magnetism only in the presence of an externally applied magnetic field. These types of material cannot maintain this magnetism once the field is removed. Paramagnetic materials have a disordered magnetic moment structure, meaning that the magnetic moments are not aligned in any way with the magnetic domains. Ferromagnetic materials, however, can maintain magnetism even without an external magnetic field. [84,85] A common material that exhibits this property is iron. Iron can be easily made into permanent magnets. Ferromagnetic materials have magnetic moments aligned parallel to the magnetic domains. The Curie temperature is an important parameter in magnetism. It is the temperature above which the material changes from a ferromagnetic structure to a paramagnetic structure. At this point, the material undergoes a considerable change in volume and entropy due to the realignment of the molecules.[82,85] Materials that exhibit the magnetocaloric effect have received a large amount of study in recent decades due to their applications in magnetic refrigeration.[82] In order to illustrate the process by which the magnetocaloric effect is used as a refrigeration system, a schematic is shown in Figure 5.

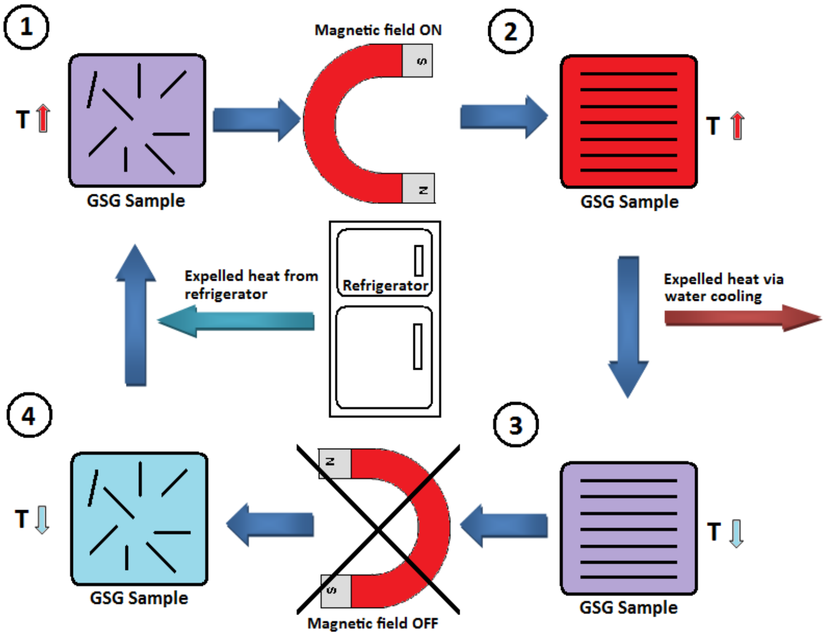

Figure 5 Magnetic refrigeration cycle consisting of a magnetocaloric material that is placed inside a magnetic field which reorders the magnetic dipoles

A magnetocaloric material initially has its magnetic moments randomly oriented with its temperature in sync with the surroundings. The adiabatic application of a magnetic field aligns these magnetic moments, but at the same time the material is heated due to no loss in energy or total entropy. [83] With the magnetic field still applied, the material is cooled by means of a liquid or gas to a temperature close to that of the surroundings. Once cooled, the magnetic field is removed while the material is kept adiabatically isolated. The removal of the field results in the thermal entropy of the material being converted to the magnetic entropy, yet at the same time the overall entropy of the material remains constant. This entropy transition causes the magnetic moments of the material to become disordered once again. [83,84] Since the thermal entropy was reduced, the temperature of the material decreases. This decrease enables the material to absorb heat from the refrigerator's chambers causing an increase in temperature for the magnetocaloric material, but a decrease in temperature for the refrigerator. This cycle is continued until the refrigerator is cooled to the appropriate temperature. [83]

The magnetic refrigerator is seen as a good replacement for the vapor compression refrigerators for several reasons. The most important reason lies in the magnetic refrigerator's potential for having a high efficiency and coefficient of performance. [84] Researchers at the University of Amsterdam anticipate efficiencies that approach close to the Carnot refrigeration efficiency and an overall increase in efficiency of 30% over a vapor compression refrigerator. [82,83] Magnetic refrigerators have also been made using permanent magnets as the source for the magnetic field. The inclusion of permanent magnets reduces the energy consumption the system would have needed if electromagnets were employed. [86] Magnetic refrigerators also reduce or eliminate the production of gases and chemicals that are harmful to the environment. Vapor compression refrigerators are known for their use of CFC's, ammonias, greenhouse gases HFCs and HCFCs, and CO_2. Reduction of these chemicals is beneficial for the environment and human health, and makes the magnetic refrigerator a design that fits well within government guidelines. [83]

The discovery of the magnetocaloric effect dates back to the late 19th Century (1881). The discoverer, Emil Warburg, found the effect in a sample of iron [82]. The study of the principle behind this effect for use in refrigeration, however, was not developed until the 1920's. At that time, Debye and Giauque proposed cooling by adiabatic demagnetization in materials that yielded this effect, but did not see the proposal through to the design until the 1930's. [82] In 1933, Giauque and MacDougall achieved a temperature of 0.25 K by using the magnetic refrigeration system. The low temperature achieved showed the potential of magnetic refrigeration systems. [82] Advancement in magnetocaloric technology increased until a breakthrough in 1997, when a magnetocaloric material was made with a Curie temperature close to room temperature. [82,84] This breakthrough allows the material to be brought to the ferromagnetic-paramagnetic transition point with less energy than was previously used. Prior magnetocaloric material had much lower Curie temperatures which required more energy to achieve the magnetic transition. In the same year, another breakthrough was made with the discovery of the giant magnetocaloric effect in the magnetocaloric material $Gd_5Si_2Ge_2$. The giant magnetocaloric effect is characterized by a simultaneous magnetic and chemical phase transition. This double effect is known as the first order magnetic-structural transformation and leads to a higher magnetic entropy change compared to common magnetocaloric materials that show a Curie temperature below room temperature. [56,82,87] A first order phase transition is transition that occurs in a material that releases or absorbs a fixed amount of energy. During this energy exchange the temperature of the material remains constant and thus has a latent heat. In comparison, during a second-order phase transition there is no latent heat and the entropy is constantly changing. [56] Second order phase transitions occur typically at the Curie temperature in ferromagnetic materials due to the high amount of entropy changes in this region; however, there are exceptions to this rule which will be discussed later. [56]

Waste heat recovery and cooling is an important issue and the unique qualities of magnetocaloric materials present an intriguing possibility for a solution to this issue. Magnetocaloric materials being used in magnetic refrigerators presents an opportunity cooling aspect while the magnetic – thermal interaction of the materials may be a key to converting heat to another form of energy due to electro magnetism. The strain properties of the magnetocaloric materials are also important and could find potential use in piezoelectric materials or crack healing applications.

1.1.5.3 Magnetocaloric and Magnetic Materials

This section discusses the performance of the magnetocaloric material and magnetic material used in this research and explains the physical, magnetic, and thermal properties that make these materials special.

1.1.5.3.1 $Gd_5(Si_{1-x}Ge_x)_4$ Compounds

The $Gd_5(Si_{1-x}Ge_x)_4$ compounds have been studied greatly in recent years due to the existence of the giant magnetocaloric effect found in $Gd_5Si_2Ge_2$ (GSG). GSG has been found to have a high amount of magnetostriction and magnetoresistance as a side-effect of the giant magnetocaloric effect. [83] Magnetostriction is an effect that ferromagnetic materials undergo when it is in a magnetic field. The magnetic domains of the material shift and rotate to conform to the applied magnetic field and cause stresses to increase in the material. Magnetoresistance is the tendency for the electrical resistance of a material to change as a magnetic field is applied. [88] Resistance in the material is maximized when the current runs parallel to the magnetic field applied to the material. Researchers have taken interests in these properties and have sought to control them. [88] The cause of the giant magnetocaloric effect in these compounds is the combined structural-magnetic phase transition. Below the Curie temperature, GSG exists as a ferromagnetic material with an orthorhombic crystal structure. [82] Once the Curie temperature is reached, the material transforms into a paramagnetic material with a monoclinic crystal structure. These crystal structures along with other structures mentioned in this thesis are shown in Figure 6.

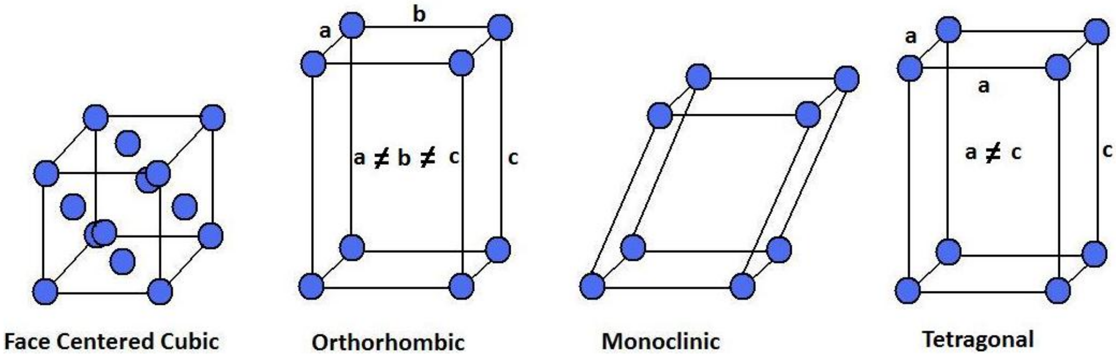

Face Centered Cubic Orthorhombic Monoclinic Tetragonal

Figure 6 Different crystalline structures within the GSG-Al composite with the Al structure at the far left, then low temperature GSG and low temperature GdAlGe, then high temperature GSG, and the high temperature GdAlGe

This sudden phase change results in the rapid expansion of the material within only a few degrees Celsius. [54] The expansion is caused by a 0.5 Å shift of the Gd atoms and a combination of the Ge and Si atoms with respect to each other along the a-axis of the material. [56] This shift, when it occurs throughout the material, causes a 1% increase in the volume at the first order magnetic transition temperature within a small temperature change. [82] The change is normally a result of a second order magnetic transition; however, due to an abrupt strain change at the Curie temperature, the first order transition exists. [48] This process, unlike many other magnetocaloric materials, is reversible. This means that the material can expand and contract and experience magnetic entropy increase and decrease as long as the material's structure is maintained. However, there does exist some hysteresis between the expansion and contraction of the material. [55,56] The hysteresis at the transition temperature is caused by the latent heat of the first order transition, which creates an average difference of 2 K between an increasing and decreasing temperature gradient across the Curie temperature. [48] The first order magnetic transition temperature of $Gd_5(Si_{1-x}Ge_x)_4$ type materials is strongly dependent on the molar ratio between silicon and germanium. [82] It was found that materials with a range of x = 0.5 to 0.76 tend to have the giant magnetocaloric effect, while values of x below that value tend to have a reduction in the magnetocaloric effect due to the elimination of the structural second order magnetic transition. [82] Having an x value greater than or equal to 0.5 results in the ability to fine tune the transition temperature from between 30 K to 276 K. However, a compromise between adjusting the Curie temperature and altering the magnetocaloric effect must be taken into account. [82,89] Research is being conducted in order to increase the transition temperatures of the $Gd_5(Si_{1-x}Ge_x)_4$ compound without inhibiting the magnetocaloric effect. In order to accomplish this, researchers are alloying the material will elements such as Fe, Co, Ni, Cu, C, Al, and Ga. The elements are often substituted in place of the germanium or silicon. However, most of the elements tend to have a negative impact on the magnetocaloric effect of the compound; but gallium seems the most promising of the elements [89]. The magnetocaloric effect in the compound as well as the hysteresis depends upon the purity of the materials that are used to form the compound. If the elements are not pure enough, the formation of the monoclinic structure near room temperature may be suppressed. Oxygen, carbon, and iron are common impurities present in the compound, and they can drastically alter the beneficial properties. [82] Impure compounds tend to show a slightly higher second order phase transition temperature, but a reduction in the magnetocaloric effect. The effect of impurities is an obstacle for researchers to overcome. [83] Some researchers have discovered ways of using impure substances and still gleaning the benefits of the magnetocaloric effect. Researchers have found a way to use impure Gd by employing a method of rapid quenching to remove impure phases from the material. This research brings about step to use less pure materials and thus lower the cost of material production. [90]

1.1.5.3.2 Gd($Al_{1-x}M_x$)$_2$ Alloys

Gd($Al_{1-x}M_x$)$_2$ alloys have been studied in recent years for their magnetic properties and their property of transitioning from ferromagnetic to paramagnetic phases at relatively high Curie temperatures. The Curie temperature is defined as the temperature at which a material changes from a ferromagnetic state to a paramagnetic state. The alloy is normally studied in an atomic ratio range that yields a C15 crystal structure for temperatures ranging from 4.2 to 300 K; however, if the alloy were equiatomic, the crystal structure would change to the YAlGe-type crystal structure (for low temperatures only). [91,92] The M-element is representative of many non-magnetic materials such as Si, Ge, Ga, Pd, Pb, In, and Sn. Similar to magnetocaloric materials, Gd($Al_{1-x}M_x$)$_2$ alloys exhibit a paramagnetic to ferromagnetic transition with a large magnetization susceptibility shift. Studies have shown a noticeable change in temperature dependence of electrical resistivity at this Curie temperature. The atomic ratio, x, within the alloys have been limited to values between 0 and 0.15 when M = Si or Ge and between 0 and 0.2 when M = Pb. [91] A plot of Curie temperature as a function of atomic ratio for each M-element is shown in Figure 7.

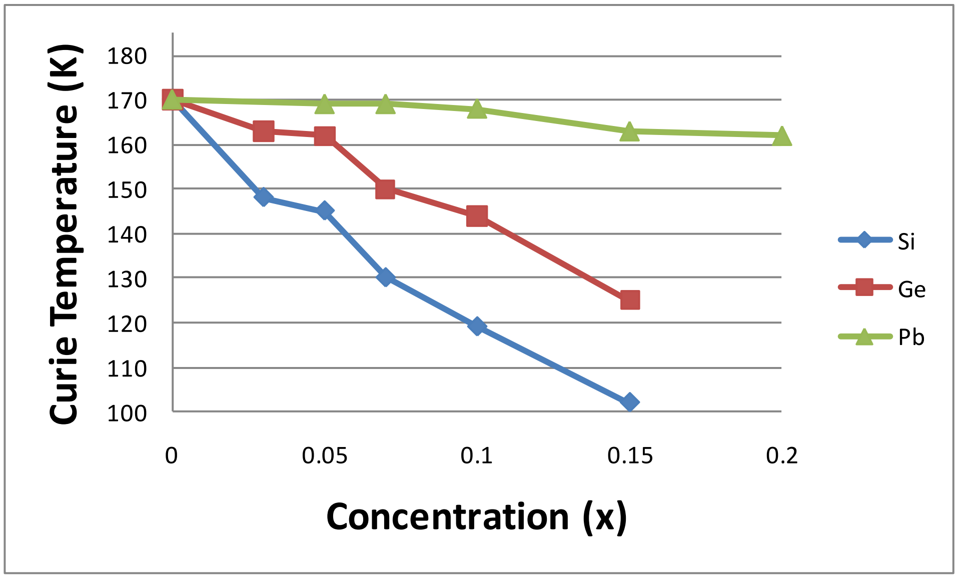

Figure 7 Plot of the Curie temperature as a function of atomic ratio of the M-elements Si, Ge, and Pb in the alloy Gd($Al_{1-x}M_x$)$_2$ (this figure is remade from [91])

When the M-element represents Sn, Ge, or Si, the atomic ratio x causes a large decrease in Curie temperature as it is increased, while not exhibiting such a large change with M-elements of Ga, Pb, or In. [92] A change in the atomic ratio does not noticeably influence the effective magnetic moment for Ge as an element; however it does increase with the atomic ratio for such elements of Pb and Si. [91] A comparison between Gd($Al_{1-x}M_x$)$_2$ and GSG is shown in Table 1.

Table 1 Characteristics of GSG and $Gd(Al_{1-x}M_x)_2$ materials

Alloy	**Crystal Structure**		**Magnetic**	**Temperature Dependent**	**Magnetocaloric**	**Best x**	**T_c**
	<T_c	**>T_c**	**?**	**?**	**?**		
$Gd5(Si_{1-x}Ge_x)_4$	Orthorhombic	Monoclinic	Yes	Yes	Yes	0.42-0.52	Varies
$Gd(Al_{1-x}M_x)_2$	Orthorhombic	Tetragonal	Yes	Yes	No	0-0.2	Varies

CHAPTER II

MOTIVATION AND OBJECTIVES

As discussed in the Chapter 1, the automobile industry has two problems that stem from waste heat through their IC engines: engine cooling and exhaust energy. There are critical needs in developing novel techniques and materials to improve the energy efficiency for the next generation of automobiles. IC engines, particularly ones made from aluminum alloys and composites are prone to fatigue and cracking. Fatigue resistant materials are needed. The present research has two major objectives:

(1) Development of novel materials that are multifunctional

(2) Obtaining fundamental understanding of microstructure-properties of a new class of composite

In order to accomplish the objectives, experimental approaches will be utilized. In synthesis of the multifunction material, a powder metallurgy method will be adapted for the process. A sintering process will be used to combine the constituent materials that make up the composite in order to not eliminate the beneficial properties of the 2 combined metals and to derive potentially new beneficial properties. The revolutionary material known as $Ge_5Si_2Ge_2$ (GSG) has long been studied for its magnetocaloric effect and phase changes. The development of multifunctional materials should start with materials that exhibit multiple phases and properties that can be controlled by or generate an energetic medium. The magnetocaloric material GSG was combined with aluminum in order to study this newly formed material and so that both materials may benefit from the properties of the other.

A broad range of experiments will be performed on the composite to determine the composite's physical and mechanical properties. The physical nature of the material will be characterized through using series techniques. The techniques include X-ray diffraction, transmission electron microscopy, and energy-dispersive X-ray spectroscopy to analyze the phases that exist within the composite as well the elemental makeup of these phases and the form of the microstructure. Knowing the form of the microstructure will either tie this material to another or may define a new micro-structural form. Analysis of these phases will give rise to insights into both the physical and mechanical properties of the composite and give reasoning to its performance under differing conditions such as gradients in temperature, magnetic field, and load.

The mechanical properties and tribological properties will be examined using techniques such as thermal expansion experimentation, magnetic property analysis, hardness studies, and tribology studies using tribometers and profilometers to gage wear rate. This data will determine the potential of the composite for energy applications as well as structural applications in various industries including the automobile industry. It is by these experiments that the multifunctional properties of the GSG and Al composite will be realized.

CHAPTER III

EXPERIMENTAL PROCEDURES

This chapter discusses the materials and procedures involved in creating and testing the magnetocaloric composite $Ge_5Si_2Ge_2$ in Al matrix ($Ge_5Si_2Ge_2$-Al). The procedure of the composite formation is followed by various characterization techniques to determine the physical, mechanical, thermodynamic, and magnetic properties of the material. This chapter covers the methods of testing as well as their necessary backgrounds.

3.1 Materials and Sample Preparation

This section describes the properties of the constituent materials used in the research of GSG-Al. The section then goes on to describe the formation of GSG and GSG-Al samples step-by-step. The magnetocaloric material $Gd_5Si_2Ge_2$ (GSG) was synthesized. Specimens were formed using an arc melting method with specific concentrations of Gd, Si, and Ge. Elements needed to form GSG samples were purchased from ESPI Metals Inc. and Sigma Aldrich. The properties of the metals used in this research are presented in Table 2. [93]

Table 2 Mechanical, physical, and thermal properties of elements

	Units	**Aluminum**	**Aluminum 6061-T651**	**Gadolinium**	**Silicon**	**Germanium**
Symbol	-	Al	Al	Gd	Si	Ge
Density	g/cm^3	2.7	2.7	7.9	2.329	5.323
Purity	%	>99	-	99.9	99.9999	99.999
Melting Point	°C	660.32	582-652	1312	1414	938.25
Modulus of Elasticity	GPa	70	689	54.8	185	
Coeff. Of Linear Thermal Expansion	1/°C	2.31E-05	2.36E-05	9.40E-06	2.60E-06	6.00E-06
Thermal Conductivity	W/m-K	237	167	10.6	149	60.2
Crystal Structure	-	FCC	FCC	HCP	Diam. Cubic	Diam. Cubic

3.1.1 Synthesis of GSG

The elements were mixed in a glass holding container and stirred by hand in a circular motion at a speed of 3 rev/sec. The samples were then arc melted in an arc furnace. The furnace was composed of an arc melting electrode, a vacuum chamber, a water cooling system, and an argon gas supply. The sample chamber was evacuated twice to a gauge pressure of -207 kPa (-30 psig) in order to allow the sample to be melted in a low combustible atmosphere. The chamber was then refilled with an atmosphere of high purity argon. The arc melting system is shown in Figure 8.

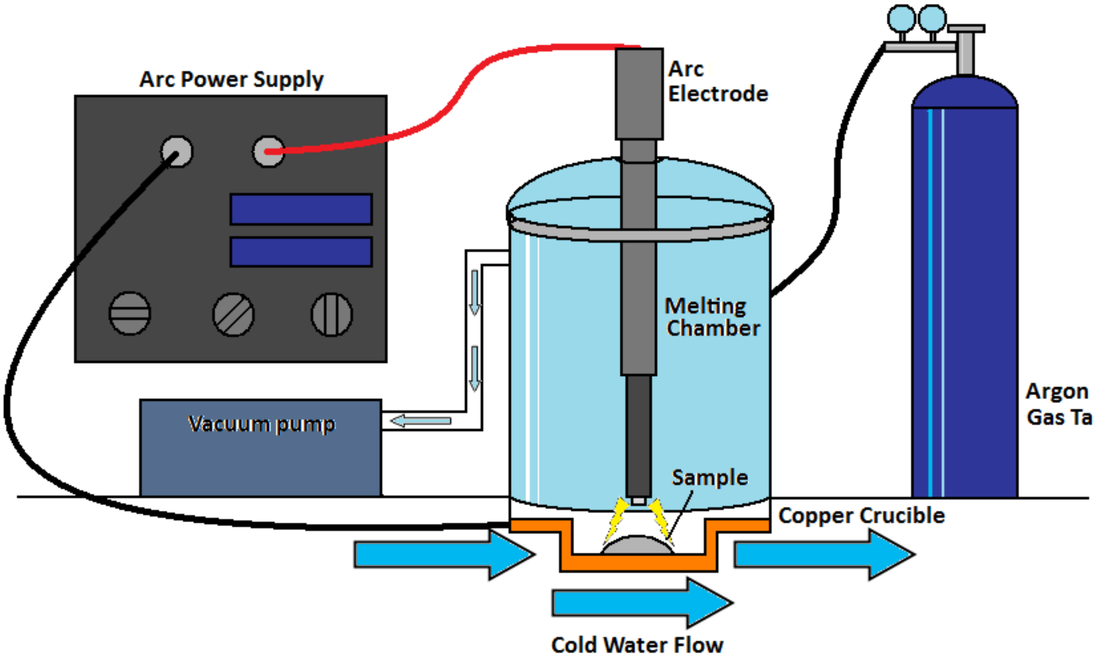

Figure 8 Arc melting system used to melt Gd, Si, and Ge and form GSG in a non-combustible environment

The GSG samples were arc-melted with a tungsten electrode in a circular pattern in order to ensure an even heating along the powders and chunks of materials. The circular pattern was started on the sides of the powdered materials and gradually spiraled in towards the material's center.

In order to make sure that the sample was properly mixed, the sample of GSG was flipped once cooled and then re-melted. The process of heating, flipping, and remelting of the GSG was repeated four times in order to improve upon the mixing of the GSG. The GSG formed yielded a density of 5.7 g/mL according to its homogeneity and specs provided by suppliers of pure GSG samples (Sigma Aldrich).

3.1.2 Synthesis of GSG-Al Composites

In order to obtain a similar magnetocaloric effect, the ratio of GSG to Al was set at 1:1. The GSG samples were crushed to an equal particulate consistency using both a rolling press for the large pieces and a mortar and pestle for smaller pieces. The rolling press was in the form of two large rollers whose distance from each other was adjustable. The GSG pieces were placed between two quarter inch steel plates and fed through the rollers. The press is shown in Figure 9.

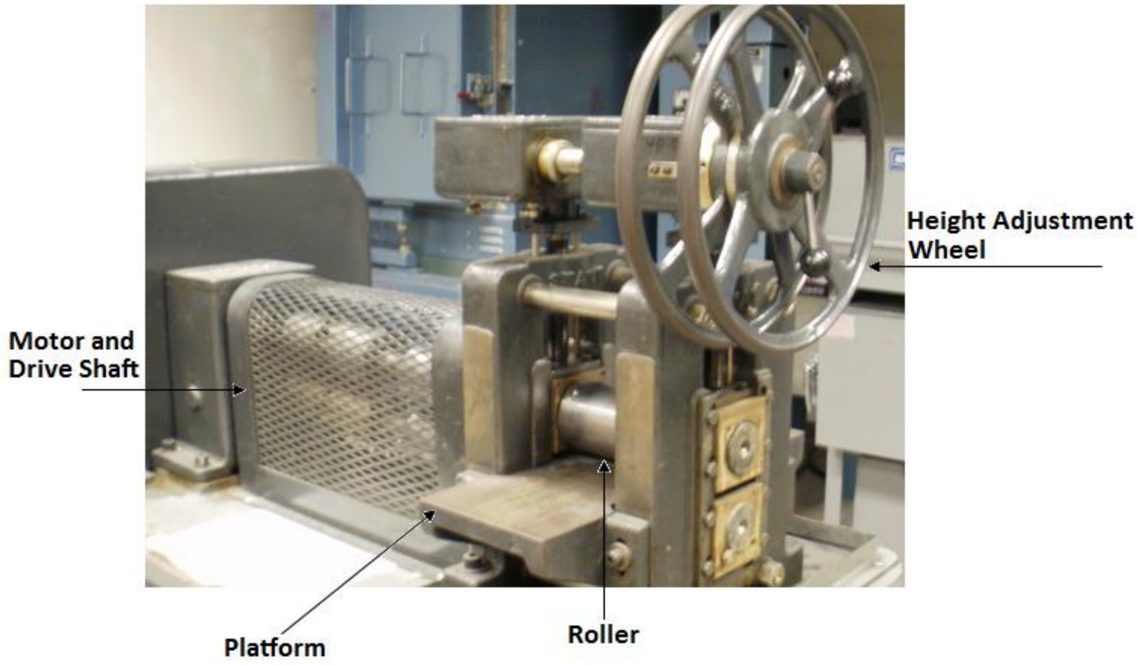

Figure 9 Roller press used to crush samples of GSG for use in making a GSG-Al composite

The smaller bits of GSG were then placed in a mortar and ground by hand with a pestle. The pestle was pushed and twisted hard into the material in order to crush the

GSG further. The samples were mixed with aluminum powders that were 20 micron spheres with >99% purity (Sigma Aldrich). The mixer used was Schatz 88 Mixer tumbler shown in Figure 10.

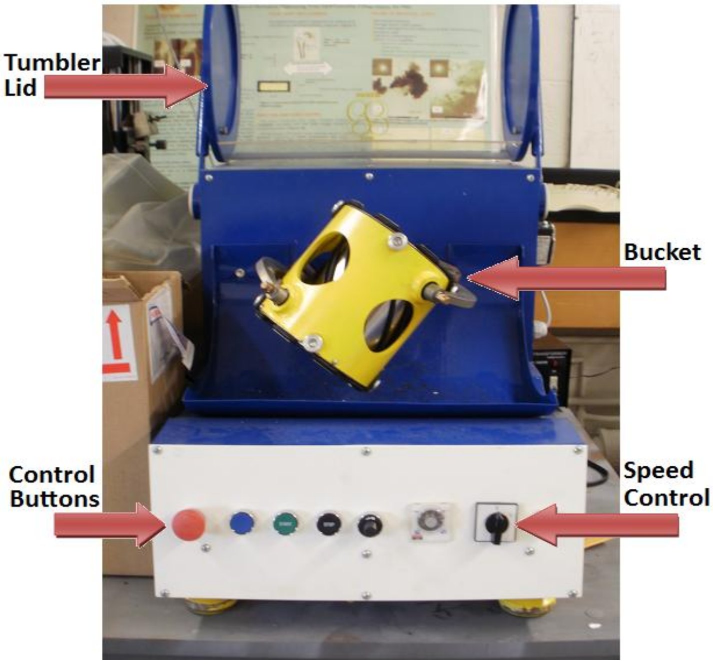

Figure 10 Tumbler used to thoroughly mix the powders of GSG and aluminum into a uniform consistency

The powders were added to glass vials in equal mass ratios and enclosed within the tumbler bucket. The bucket was rotated in a biaxial fashion as to better mix the samples and was done so at a rotational speed of around 2 revolutions per second for one hour. Once thoroughly mixed, the samples were mixed with small amounts of water, typically no more than 2 large drops per gram of powder, to aid in the compression process since the dry powder tended to not adhere as well. The powder samples, now clay-like in consistency, were then poured into a cylindrical die with a 16 mm diameter and placed in a press under a load of 20 tons (U.S. pressure gauge) which produced a pressure of 0.885 GPa. The compressed samples were then put in a quartz tube furnace with an argon rich atmosphere to reduce the oxidation process. The tube furnace is shown in Figure 11.

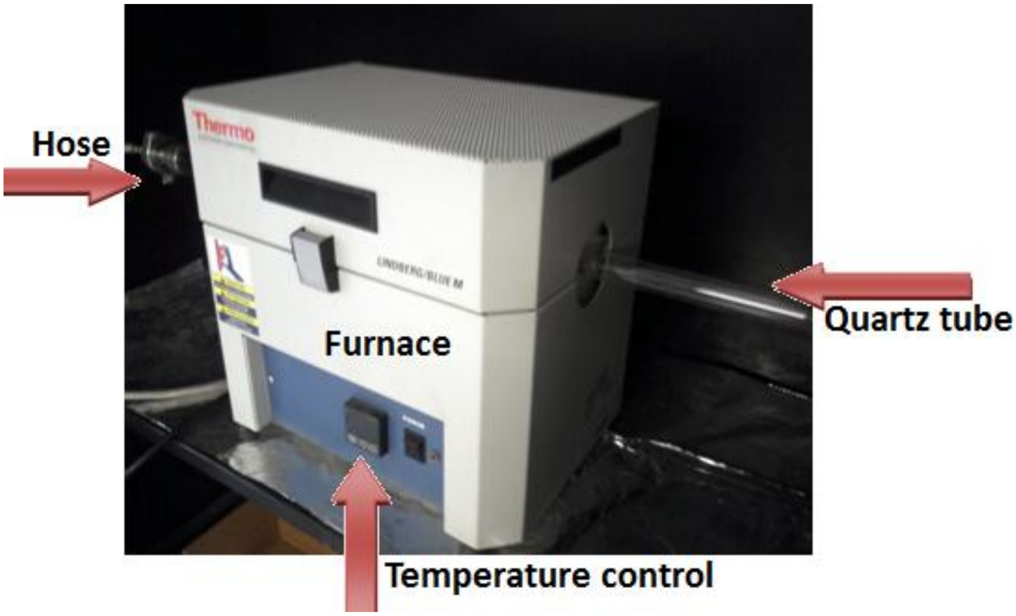

Figure 11 Tube furnace used to sinter the composite GSG-Al at 850°C

The tube furnace allows for a continuous flow of argon over the samples from a compressed gas tank. The samples were sintered by quickly heating the samples to 850°C at a rate of 0.5°C/s, letting the samples set for 8 hours, and then allowing the samples to be cooled in the air until they were at room temperature.

Sintering is a process in which the sample is made from combined powders of elements that are heated in a furnace to a temperature below the melting point of the newly formed mixture. [94] This process causes the powdered elements to adhere to one another making a solid sample in a similar shape to what was placed into the furnace. The sintering process was used to prepare the samples. The preheating and cooling path for the process is shown in Figure 12.

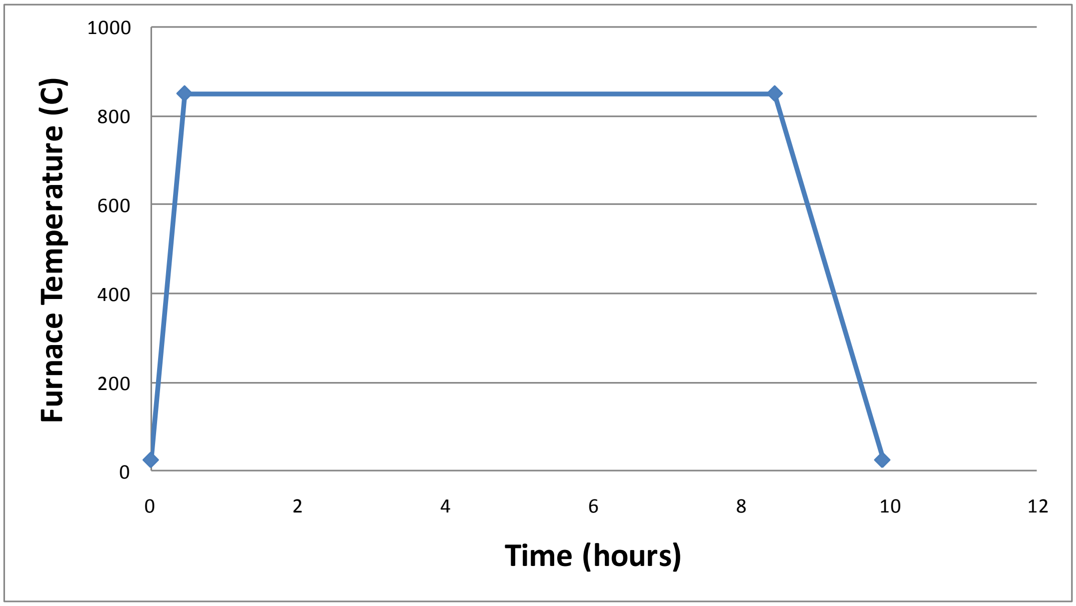

Figure 12 Preheating and cooling path for the tube furnace when sintering GSG-Al

There are several advantages to this type of metallurgical procedure; one is that the original powders maintain their chemical composition. The sintering process also can allow the sample's compounds to maintain their individual characteristic properties as long as the temperature is kept within correct parameters pertaining to the constituent elements. [94] This is an important property since it is desired for the magnetocaloric properties of the GSG to be maintained and the structural properties of the aluminum to be put into effect. The sintering process allows for properties of composites to be built into the composite. In the current research, strength, magnetic, and thermal properties of two materials are expected to be added to the composite.

3.2 Sample Polishing

This section describes the process involved in polishing samples of GSG-Al and Al 6061-T651. The samples were polished in preparation for wear testing and hardness testing. The samples were hand polished with six sand paper levels with differing grit concentrations. The grit sizes were 280, 320, 400, 600, 800, and 1200, and the sanding progressed through in that order (course sanding to fine). The sander used was a Bueler Ecomet II rotating sander that allowed for water to drain. The samples were sanded on each grit size paper for 20 minutes and were done so with water being constantly poured onto the sanding surface. In order to aid in the reduction of sanding lines on the sample, the material was rotated by hand back and forth by hand at a rate of around 2 times per second. Once the sanding was completed, the samples were cleaned with acetone followed by a rinse in deionized water and then wiped with clean tissue paper.

3.3 X-Ray Diffraction

The process by which the X-Ray Diffraction tests were performed on samples of GSG-Al is described below. The theory behind the diffraction process as well as the reason for the testing is also described in this section. In order to ensure that the material formed has the optimum structure and phases, an X-Ray Diffraction test (XRD) was performed. X-rays are used for probing the crystal structure of solids. X-rays are also energetic in order to penetrate most solids enough to gain information on their composition and structure. [95]

X-rays mostly interact with the electrons in atoms. Once the X-ray beam hits the sample, the beam is deflected by the electrons in the sample. The diffractometer used in this research measures only elastically scattered beams or beams that maintain the same wavelength as the incident beam and that did not lose any energy. [95]

The data obtained from diffraction consists of plots of counts or intensities versus the diffraction angle 2θ. An effect can be seen from the interference of diffracted beams from different atoms. This effect is noticeable in the intensity distribution when the diffracted beam is analyzed. When the material has crystalline structures, this effect is magnified and results in sharp intensity peaks. The peaks in X-ray diffraction are directly related to the atomic distances and are formed when the Bragg diffraction condition is satisfied. This condition is defined by Bragg's Law below. [95]

$$n \cdot \lambda = 2 \cdot d \cdot \sin(\theta) \qquad (5)$$

In the equation, θ is the diffraction angle of the X-ray incident beam with the sample, λ is the X-ray wavelength, d is the distance between planes in the atomic lattice, and n is the order of reflection. A schematic of Bragg's Law applied to a 2D model is shown in Figure 13.

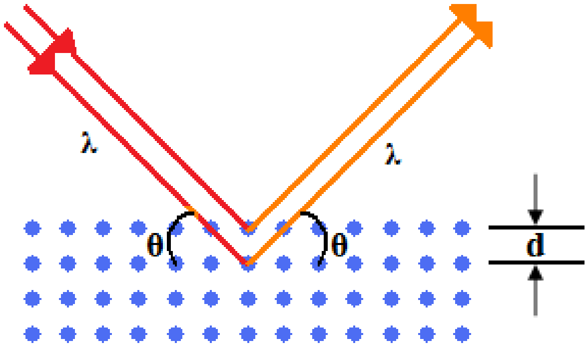

Figure 13 Two dimensional representation of an atomic structure being hit with and reflecting X-rays

The red lines represent the incident X-ray beam while the orange lines represent the diffracted X-ray beam. The blue dots represent atoms arranged in a crystalline structure. [95]

For the XRD analysis of the materials a Bruker-AXS D8 Advanced Bragg-Brentano X-ray Powder Diffractometer was used. This diffractometer functions with a copper anode X-ray radiation source at a wavelength of 0.154178 nm and 8 keV. The diffractometer itself is shown in Figure 14 and Figure 15.

Figure 14 XRD machine used to perform analysis on samples of GSG-Al (housed in the Chemistry Department of Texas A&M University)

The X-ray tube and Bragg-Brentano primary beam optic unit are mounted on the left and output the incident X-ray beam onto the sample. The center circular structure is the carriage which serves to hold the beam and optic unit and also serves as a goniometer. The goniometer is a device that aids in the precision angle measurement of the system. The sample is mounted on the stand (normally a steel cup) in the center which is itself mounted onto the goniometer. The NaI (sodium iodide) scintillation detector is mounted on the right and serves to collect the diffracted beams coming off of the sample. The carriage and the sample are coupled so that the rotation of the sample with θ is accompanied by a scintillation detector rotation with 2θ. The 2θ angle (from the data) is the diffraction angle made between the scintillation detector or counter and the sample.

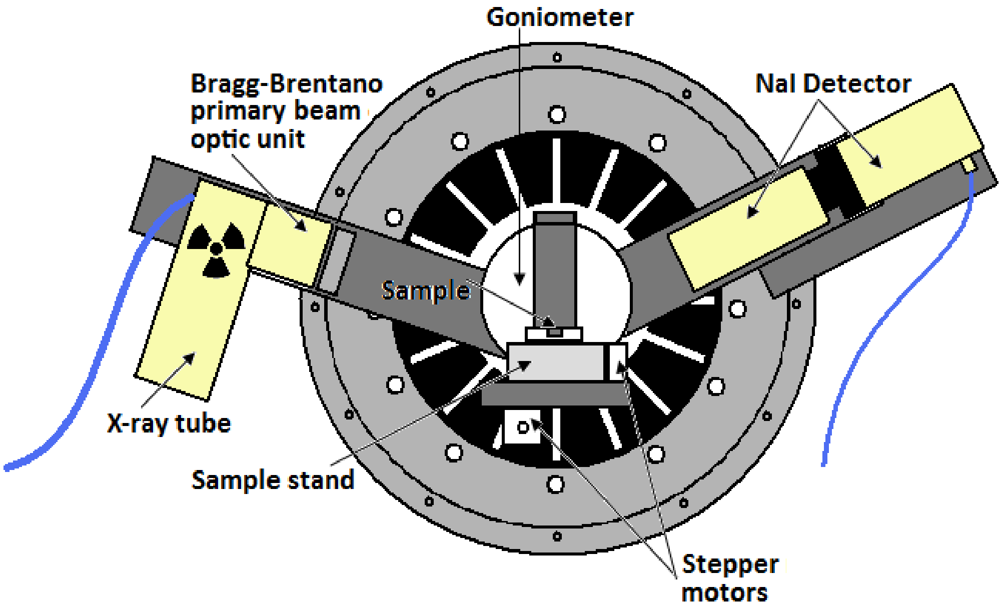

Figure 15 Experimental set-up for the XRD tests on the Bruker-AXS D8 Advanced Bragg-Brentano X-ray Diffractometer

The XRD analysis for all GSG-Al samples was performed in a similar manner. The sample was mounted in the stage cup with putty in order to keep the sample still. The stage cup is shown in Figure 16 with the sample mounted inside.

The doors to the XRD mechanism are made of lead glass and were closed in order to minimize the radiation leakage. The XRD was connected to a computer which collected the data and also allowed for the test parameters to be changed. These parameters included the diffraction angle (2θ) range and the step size. The diffraction angle range depends upon the range found in XRD plots from previously published documents on this material. The material GSG-Al is a new composite material and published documents for this material do not exist. The diffraction angle range was decided upon by using the same range as the previously published XRD results of GSG. The diffraction angle range for GSG-Al is from 5° to 70°. The step size was held the same for all samples at 0.014828 seconds/sample.

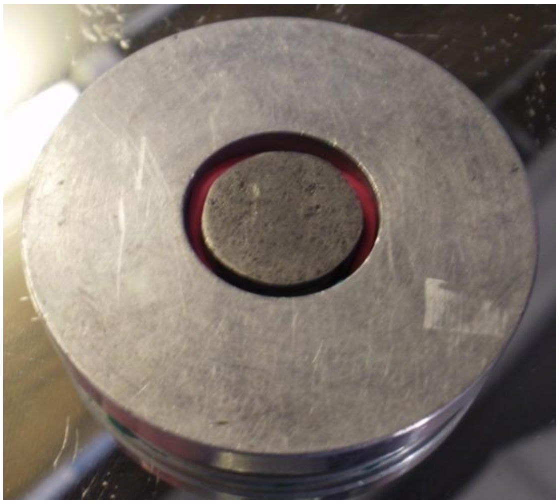

Figure 16 Stage cup used in the XRD analysis of GSG-Al. At its center is the GSG-Al sample with red putty holding it in place

The peaks for the GSG-Al samples were analyzed by overlaying XRD plots of all possible phases of the different elemental arrangements. For instance, the XRD plot of GSG-Al was plotted against AlGd, $AlGd_3$, and Ge, among others. The peaks of the different phases were compared to that of the GSG-Al. Each compound or element that fit the criteria was considered as a possible representation for that particular peak. The next criterion that was considered was whether or not a compound or element matched multiple peaks. If this was true, the element was placed on a high rank. After the eliminations were complete, each peak was labeled with the corresponding compound. Since the samples were made in a sintering process, the likelihood of a single element being represented by a peak was higher than if it was fully melted.

3.4 Surface Roughness

The process of roughness measurement using a stylus profilometer is described below. This section describes the theory behind obtaining the roughness values as well as the importance of this test. Roughness plays important roles in understanding the effects at the interface. It is typical for a highly rough surface to exhibit greater wear on or from another surface. The roughness reflects the polishing process and the surface quality.

For the surface roughness test, a Qualitest TR1900 Surface Finish Tester (stylus profilometer) was used due to its wide range of data parameters. The stylus profilometer can calculate average roughness (Ra), RMS roughness (Rq), an Abbott-Firestone bearing curve, maximum valley depth (Rv), maximum peak height (Rp), maximum height of surface profile (Rt), the distance from the highest peak to the deepest valley (Rmax), and the peak density (D). A sketch of a surface roughness profile is pictured in Figure 17 along with several roughness parameter representations.

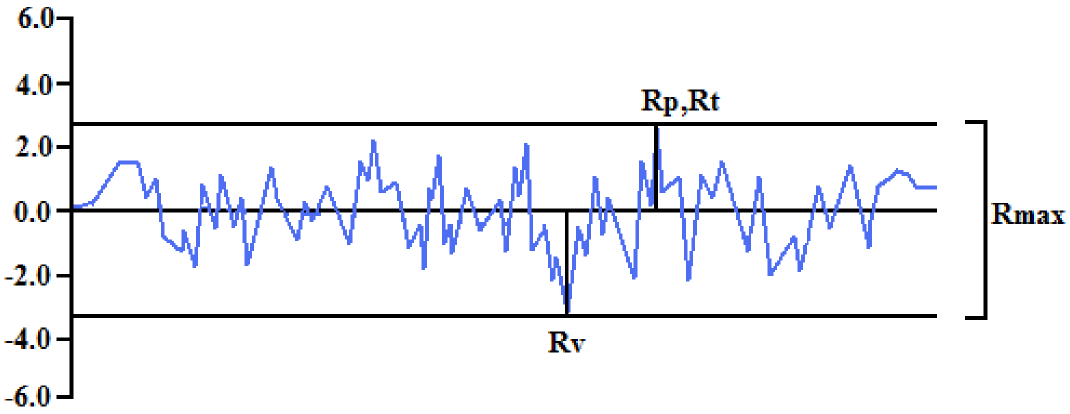

Figure 17 Example of a surface roughness profile along with representation of different roughness parameters

The average roughness (not shown in Figure 17) is the summation of the distances from the median line to the profile line divided by the number of sample distances that are taken. The median line, represented by the line 0.0 on Figure 17, is a line that demarcates a position in the surface profile where the area of the peaks above the line equals the area of the valleys below the line. The average roughness parameter is the most used roughness parameter and is used to compare different surfaces finishes. Such finishes can be characterized by polished, ground, honed, and cast, to name a few. The root mean squared roughness is similar to average roughness, except that it is the RMS value of the distances is taken. The RMS roughness is another common method of representing roughness and is always greater than or equal to the average roughness value. The RMS value is a better averaging method for data points that are positive and negative. The bearing ratio is another important part of the surface profile. The bearing ratio can be represented by an Abbott-Firestone curve. The curve is produced by tracing a line through varying depths of the surface profile. The traced line portions that lie within the surface peaks are then summed to a total length and then divided by the evaluation length in order to obtain a percentage. The percentages are then plotted versus the height of the profile. The curves are a good descriptor of the surface being analyzed. A steeper slope indicates a surface with tall, thin peaks, while a broad and bulky curve indicates a surface with small, wide peaks.

The line traced by the profilometer stylus can be broken into several different sections. A representation of this division is shown in Figure 18.

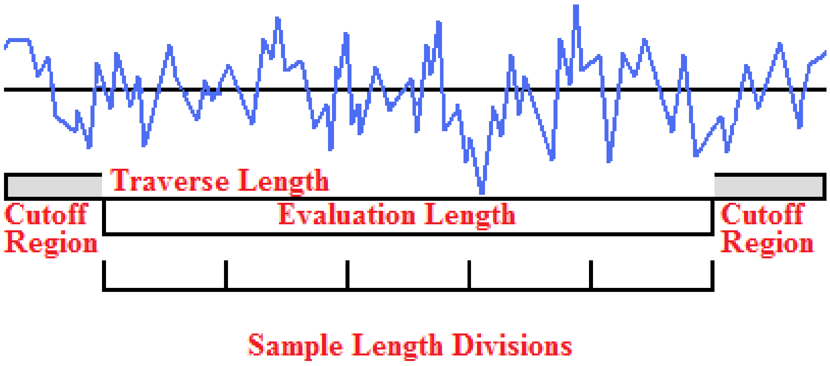

Figure 18 Labels of different sections of a roughness profile sample

The traced line is known as the traverse length. This segment is reduced to an evaluation length by discarding the cutoff regions at the beginning and end of the segment in order to remove any errors made when the stylus started and stopped moving. The evaluation length can be further decreased by dividing it up into sample lengths. The sample lengths are then individually evaluated for the roughness parameters.

The purpose of these experiments is to see how well the samples were polished for their use in wear testing. Surface roughness can have an effect on the coefficient of friction at the early stages of wear or running-in period. The testing can also indicate how well the surface is polished and if different measures need to be taken to diminish the roughness. The profilometer setup used in this experiment is displayed in Figure 19.

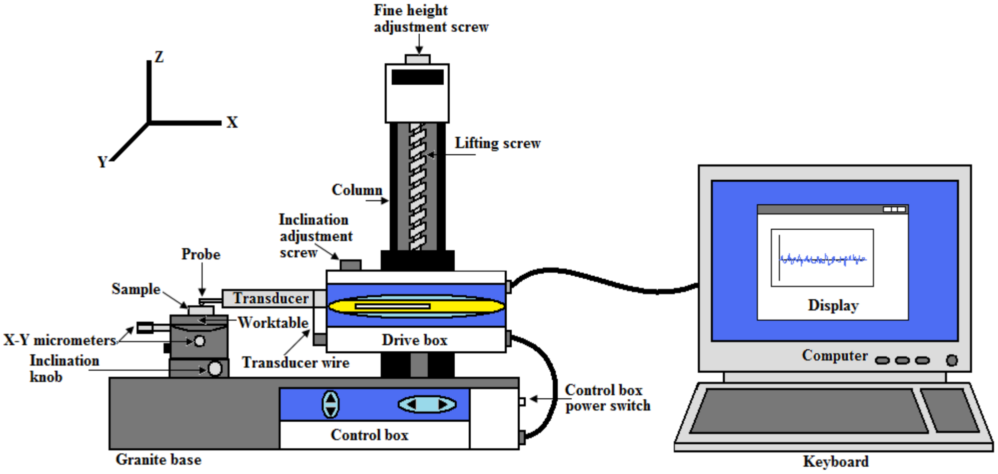

Figure 19 Experimental set-up of the stylus profilometer surface roughness tests with the Qualitest profilometer on the left and a computer on the right

The profilometer used in this experiment is a computer controlled setup that allows for precise manipulation of the sample worktable and accurate roughness measurement using an inductive pick-up design. An inductive pick-up transducer is a form of sensor which is able to detect the motion of the metal stylus. The voltage of the transducer is changed by the movement of the stylus and the voltage is transported to the computer software to be converted to a depth and length measurement.

The surface roughness tests were performed on samples that were prepared in the method described in section 3.2. The basic procedure for the use of the system is straightforward. The profilometer comes with a computer program. This program allows the user to initiate the tests from the computer screen. Parameters were selected in the program. These parameters included the selection of the type of surface (plane or sphere), the sample length division distance (0.25, 0.8, or 2.5 mm), and the evaluation length (multiple of the sample distance up to 5X). When these parameters were input into the program, positioning of the sample was the next key step. The sample was placed onto the worktable and the 2 nm radius, diamond stylus was positioned above the sample at the spot where the test was to begin. The worktable is equipped with two micrometers and two inclination adjusters. The two micrometers control the manipulation of the sample in the X and Y directions, while the two inclination adjusters can tilt the sample about the X axis or Y axis. At this point, the sample was positioned in a way so that the stylus would remain on the sample surface throughout the entire test (no run-offs). The sample was appropriately secured to the sample platform using a vise so that movements would not corrupt the data. Once this was done, the stylus was gently lowered onto the sample to a default normal load of 0.7 mN and the profiling test was initiated on the computer screen. The stylus moved across the surface of the material at a rate of 0.5 mm/s. The vertical and lateral motion of the stylus was carried out by the drive box. When the profile line had been made, the computer program showed the entire line on a plot of the X-Z plane (length versus depth). Two spots were selected on that line to serve as the evaluation length to be analyzed by the computer. The two spots were selected to demarcate a segment that showed a stable roughness with no extreme peak or valley depths. This brought up a screen that showed the data for that particular test. Once this data was saved, the sample was repositioned so that another profile line could be made. Performing these tests several times allowed for the data to be averaged. Care was taken not to cross the profile lines since the stylus made an indentation scratch on the sample's surface, which could have altered the results.

3.5 Phase Distribution

GSG-Al is a sintered combination of $Gd_5Si_2Ge_2$ and aluminum. The relative concentration of the two phases must be analyzed as a function of area due to the 2D view from the microscope used in the experiment. The two components were combined in a 1:1 ratio on a per unit mass basis. Using an optical microscope, these phase relationships can be analyzed by comparing the area of the GSG to the aluminum. A Keyence VHX-600 series digital microscope was used to capture the images from a magnifying set of lenses. A picture of the optical microscope is shown in Figure 20.

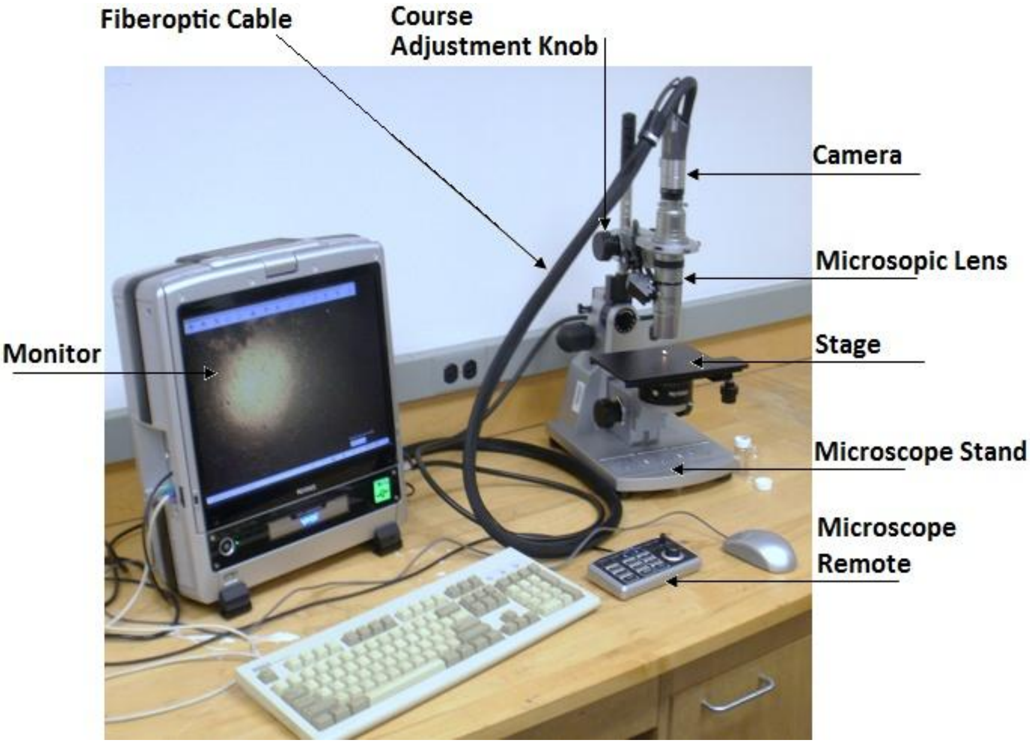

Figure 20 Optical (digital) microscope used to view and study samples of GSG-Al and Al 6061-T651 for mechanisms of wear and phases due to its ability to save digital pictures of microscopic images

Since both phases in GSG-Al reflect light differently, the optical microscope can be used to isolate the two different patterns so that the ratio of the 2D areas of the two phases can be analyzed. In order to determine the concentrations, an image analysis software Image Tool was used. This information can be used for optimization of the microstructure.

Image tool is a powerful software capable of measuring and quantifying images. In this research, this software was used to determine the percent area of GSG and Al phases on the surface of the material. The image was first imported into Image Tool by opening an image file in the mentioned program. The software was capable of selecting a viewing area which defined the sample's perimeter. Filters were applied to the image that changed the color of the individual pixels to either black or white depending on their shade, color, and contrast. This filter was set by using the "Processing" menu and selecting "Color-to-grayscale" which would change the image from color to grayscale. "Threshold" was then selected from the "Processing" menu and a manual manipulating of the scale was initiated. The threshold was adjusted until the GSG phases were covered by black pixels. The contrast was adjusted by controlling the defined threshold of the built-in filters. The areas of the GSG and Al phase were eventually sorted into either black or white pixilated regions. The software then counted the number of black and white pixels and saved the number in a file. The process was repeated using 6 separated images to minimize lighting and camera effects and to obtain an average. The average of the percent area and the error are calculated for each of the phases.

3.6 Transmission Electron Microscopy

The wear debris samples were characterized using a Transmission Electron Microscopy (TEM). The TEM is composed primarily of 3 systems: the illumination system, the lenses and specimen stages, and the imaging system. [34] A basic schematic of the TEM system is shown in Figure 21.

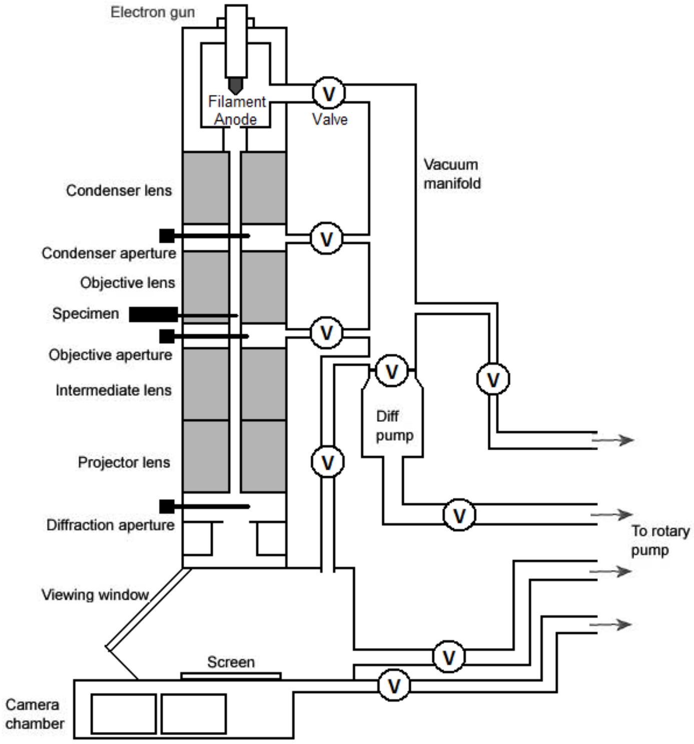

Figure 21 Schematic of a transmission electron microscope used in the study of wear debris

The illumination system is the source of electrons for the microscope. This section is comparable to the light source for common light microscopes. TEM use two different forms of electron sources: thermionic sources and field-emission sources. [34]

Thermionic sources produce electrons when heated and typically are less monochromatic; however, they do produce more energetic electrons. In order to emit electrons through heat, the work function of the material must be surpassed. The work function is the natural barrier to electron emission and it is specific to each material. In order for the source or filament to work it needs to be made of a material with either a high melting point or a low work function. [96] The two most used filaments of tungsten and lanthanum hexaboride (LaB_6) fit the criteria (tungsten being the high melting point filament).[96]

Field-emission sources produce electrons through the application of a strong electromagnetic field. The electromagnetic field is strongly increased as the filament is bent to a smaller radius. Tungsten is well suited for the high electromagnetic field as well as the stresses induced at the sharp bend, but LaB_6 can also be used. Overall, tungsten filaments offer the least performance. The tungsten is reliable, inexpensive, robust, and easily replaceable. LaB_6 is better for instrumental use and can create a brighter image if designed correctly.[34] The lower operation temperature increases the life of the filament; however, the filament is very expensive compared to tungsten. The electron gun is completed by the combination of the source with an anode. The anode accelerates the electrons from the source, thus creating a beam. The use of a Wehnelt cylinder, which is a type of electrode, aids in the control and focus of the electron beam.[34] The lenses of the TEM can be broken into four different types: condenser, objective, intermediate, and projective lenses.[34] Lenses in the TEM sense are not the same as the glass lenses used in light microscopes. The lenses are in fact combinations of electrostatic and magnetic fields that adjust the electron beam. The condenser lenses use the two combined fields to adjust the beam location, size, and intensity before the beam comes into the objective lens section of the TEM. The objective lens focuses the beam onto the specimen in a particular area. The objective lens can also magnify the image.[34] A polepiece is situated in the objective lens which provides a concentrated magnetic field near the specimen.

The sample is usually placed within the objective lens region and the position of the sample relative to the objective aperture can create different forms of imaging modes. The electron beam passes through the sample prior to reaching the objective aperture (metallic plate that filters electrons) which gives the user the option of selecting whether the TEM will detect the electrons scattered by the sample or the electrons that pass through unscattered. Images constructed using the unscattered beam electrons are known as bright field images. If, on the other hand, the image is created from only the scattered electrons, the image is called a dark field image. [96] Bright field images are important since they provide a mass thickness contrast of the sample, while dark field images display diffraction and defect contrasts. Bright field images are the most common because they show a 2-D projection of the sample. [34]

The intermediate lenses allow the magnification and fine tuning of the image prior to it being projected. The projector lens is used for scattering the electron beam that is sent from the objective lens region onto a phosphor screen so that the sample image can be seen by the user. [34] The projector lens can best be compared to the scattering device used in cathode ray tube televisions to scatter the electrons onto the screen for viewing.

An important component in every TEM is the vacuum system. A vacuum is needed for two reasons. The first reason is to reduce the frequency of collisions of the electron beam with air or gas molecules thus generating a mean free path. The second reason is to prevent arcing in the TEM due to the voltage difference between the electron gun and the ground. Different TEM's need different levels of a vacuum and can range from 10^{-4} Pa to 10^{-9} Pa. [34] Typically TEM have two pumps: a low level vacuum pump capable of achieving (10^{-3} Pa) and a turbomolecular or diffusion pump.[34]

The movable stage and specimen holder are important parts of the TEM due to the fact that they are the only link between the test samples and the user. The stage holds the specimen in place under the objective lens. The stage can best be described as a rod with a motor attached to the specimen holder. A schematic of the side entry stage is shown in Figure 22.

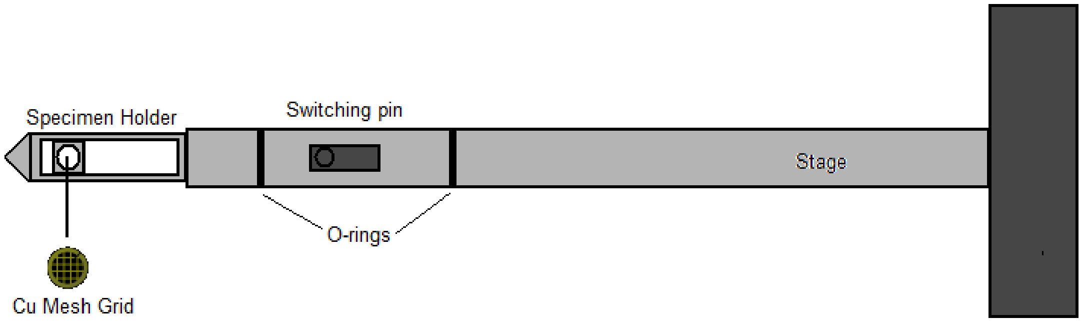

Figure 22 Side stage entry for a TEM along with the Cu mesh used to hold the sample under study

The stage has many designs available to use. Each design has features that can allow certain position manipulations of the sample as well as features that enhance the seal between the vacuum and the external atmosphere. Common stage types are O-ring, jewel bearing, specimen cup, and clamping ring or screw stages. [34] The sample or specimen itself rests on a copper mesh grid that is approximately 3 mm in diameter. [96] The mesh is placed directly in the specimen holder for insertion into the TEM.

The imaging system allows the viewing of the TEM image in real time as well as develops images for research use. The image seen depends upon whether bright or dark field modes are put into effect.[34] The magnification can be changed by adjusting the intermediate lenses. Modern TEM is equipped with digital imaging systems that can digitalize the scattered electron beam.

A TEM is equipped with special sensors that test the elemental make-up of the samples. The method of performing elemental analysis on samples is called energy-dispersive X-ray spectroscopy (EDS). [96] In order to describe the functioning of EDS, the effect of electrons on the sample and vice versa must be known. When the electron beam hits the sample, the sample can either emit elastically scattered electrons, in-elastically scattered electrons, or experience electron-electron interaction. [96] Elastically scattered electrons are scattered in such a way that their kinetic energy is conserved. [96] Inelastic scattering does not have their kinetic energies conserved. Electron-electron interaction can occur in one of three ways. The first involves an electron from the beam hitting an atom's valence electron. The collision causes a valence electron to be knocked out of atomic orbit and become secondary electrons. The second form of electron-electron interaction occurs when an electron from the electron beam strikes an inner orbital electron and sends the electron out of atomic orbit. When this happens, a higher energy electron descends to this lower energy level to fill the void of the electron. At the same time, this higher energy electron must release energy in order to take hold in this lower orbital. This release in energy results in the emission of radiation. In this case the radiation is a high energy photon, typically an x-ray. The third form of electron-electron interaction is similar to the second form. The difference lies in that the energy released from the descending electron is transferred to another electron. This causes the electron to be ejected from the atom. This tendency is known as the Auger Effect and the electron ejected is known as an Auger electron. [96] As with the previous two forms of interaction, Auger electrons can also be detected with the right detectors. The EDS analyzes the electron-electron interaction in which X-rays are emitted from the descending outer electron. This energy is characteristic of the difference in energy between the two shells and therefore is characteristic of the element the atom makes up. It is by this energy measurement that the element is determined. [96] The EDS can output a plot of counts versus electron voltage. The peaks in this plot are representative of a particular element.

Rather than the bulk material of GSG-Al being studied under a TEM, the wear material obtained from wear tests on the material (discussed later) were of more importance due to the oxidation effects during testing. The wear debris for both the GSG-Al and Al 6061-T651 was studied under the TEM in order to better understand the geometry of the wear particulate. EDS was performed on GSG-Al only. It is unknown after the wear tests how much oxidation occurred in the samples or if one phase tended to wear more than another phase. EDS can only sample small areas of the sample at a time. This means that concentrations in one area of the sample may not be representative of the entire sample. To improve accuracy, several EDS scans must be taken. When the data is compiled, a measure of the relative oxidation and phase percentages can be analyzed. The weight percentages of the different trials for the different samples were combined and averaged to form a plot of weight percentages for each element at each temperature.

GSG-Al and Al 6061-T651 debris were collected after wear tests performed at temperatures at 25°C, 50°C, and 150°C. The wear debris was collected and mixed with acetone. A syringe was used to place a small droplet of each sample on different copper mesh grids. When the acetone evaporated, the wear debris settled on the mesh. The grids were then taken to be analyzed in the TEM. The TEM used was a JEOL 1200EX with a 0.45 nm resolution and a 60-120 kV voltage range with an EDS analyzer. The TEM was operated using a LaB_6 filament under field emission voltage and in bright field image mode. Magnification of the wear debris ranged from 10kX to 150kX for GSG-Al and from 2.5kX to 100kX for the Al 6061-T651.

3.7 Hardness Testing

This section describes the processes involved in performing two forms of hardness tests on GSG-Al and Al 6061-T651 and the function behind the testers used. Rockwell and Vickers microhardness tests are used to determine the bulk and phase hardness of the samples under study.

3.7.1 Rockwell Hardness Testing

The hardness of a material is an important parameter since it can encompass a wide variety of properties including wear resistance and durability. [97] A Rockwell hardness test type 30-T was performed on GSG-Al. The Macromet I Rockwell test apparatus used is shown in Figure 23.

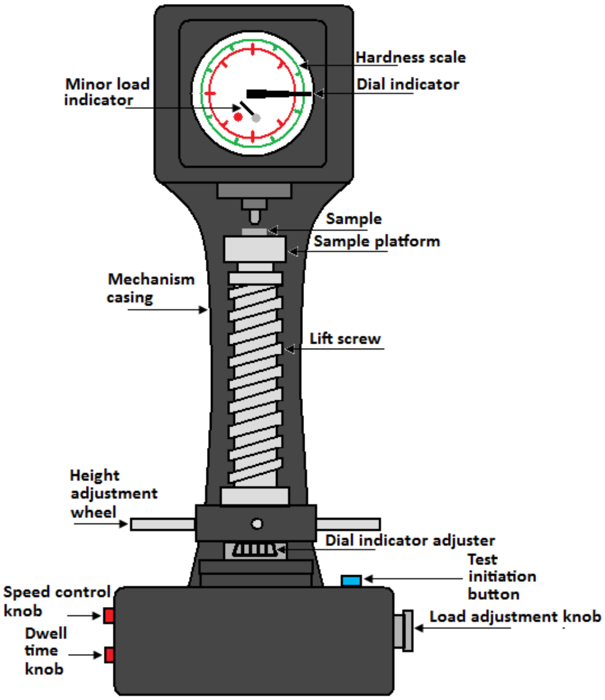

Figure 23 Schematic of the Macromet I Rockwell hardness testing apparatus used to determine the hardness of GSG-Al and Al 6061-T651

Two types of indenters can be used to perform a Rockwell test: diamond cones and hardened ball indenters. For this study a tungsten ball indenter was used. The indenter is forced into the test sample initially with a preload of a value defined by the specific testing standards. [98]The Rockwell tester was set with a 1/16" tungsten carbide ball. The test specimen was placed upon the mechanism's anvil so that it was flat and level. The major load of 30 kgf was selected via a knob on the side of the mechanism and the dwell time was set for 10 seconds. The sample and anvil were raised via a lift screw and height adjustment wheel until they were near to the indenter. The height adjustment wheel was then turned further until the indenter started to press into the sample and reach a minor load of 3 kgf. The minor load was known to be applied when the minor load indicator was pointing to a red dot. Once the minor load was applied, the hardness dial indicator was adjusted to point to the "Set-Set" marking on the dial face. This was done using the dial indicator adjuster. When the dial indicator was adjusted, the initiation button is pressed and the mechanism automatically applied the major load for the designated dwell time. Once the major load was removed, the hardness dial indicator pointed to the hardness value. The value was noted and identified with the appropriate hardness scale. The process is then repeated to gather more hardness data. The hardness test was performed on both a GSG-Al sample and an Al 6061-T651 sample. This would allow for comparisons between the properties of the two materials. The dwell time is an important parameter since it can directly affect the hardness measured. When the major load is removed and the minor load is still applied, the depth of the indicator may "spring back" to a slightly higher position than the loaded depth due to the elasticity of the material. This rebound can be increased or decreased depending on the dwell time. A longer dwell time deforms the material for longer and can cause a larger plastic deformation effect.

Multiple hardness tests were conducted on the samples. It is common practice to distance the test indentations at least 3 ball indentation diameters away from each other and 2 ½ diameters from the sides of the material. [98]This prevents the stresses created by the indentations from affecting each other. Positioning away from the edges of the material makes sure that the hardness is affected by the encompassing bulk of the material. Averaging of 12 tests for GSG-Al and 20 tests for Al 6061-T651 obtained the nominal hardness value for the materials.

3.7.2 Micro-Hardness Testing

The Vicker's hardness test covers two distinct force ranges: macro and micro scales. The macro scale ranges from 1 kg to 100 kg, while the micro scale ranges from 0.01 kg to 1 kg. [99] Macro scale tests and micro scale tests with loads as low as, but not including, 0.2 kg are considered to be load independent. [99] This means that the hardness value for the test is not influenced by load. The square pyramid indenter is used for both macro and micro Vicker's tests. The pyramid has a 136° angle from the base to the apex to the opposite base and is made of diamond due to the material's large hardness. [99] A drawing of the indenter with important dimensions is shown in Figure 24.

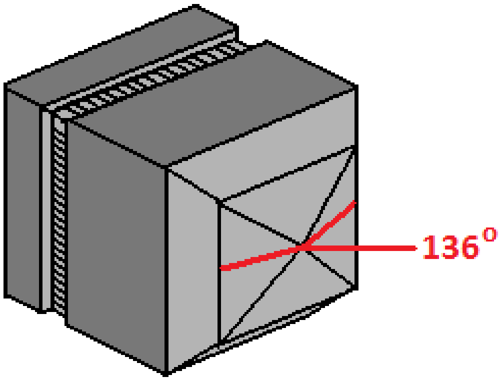

Figure 24 Vicker’s test indenter with a 136° square pyramidal diamond point

A Vicker’s test is performed by forcing the indenter into the material under a specified load. The indenter is allowed to set in the material with the applied load for a certain amount of dwell time. For the tests performed, the load was set to 0.3 kg while the dwell time was set to 13 seconds. The indenter is removed from the material leaving a square shaped indentation in the material. The hardness of the material is calculated by measuring the diagonal lengths of the square indentation. The Vickers hardness calculation is made using equation 6: [99]

$$HV = (C \cdot F_{max}) / D_{avg}^{2} \qquad (6)$$

where HV is the Vickers hardness number, C is a constant that is dependent upon the force, indenter geometry and diagonals; F_{max} is the maximum load applied during the test, and D_{avg} is the average of the diagonal lengths.

A LECO Microhardness Tester Model LM 300AT was used for Vicker's hardness testing. The specimen stage was equipped with two micrometer style adjusters that could move the sample in the X and Y axes. The indenter was attached to a rotating stage that was equipped with microscope objectives of varying magnification.

A schematic of the system is shown in Figure 25.

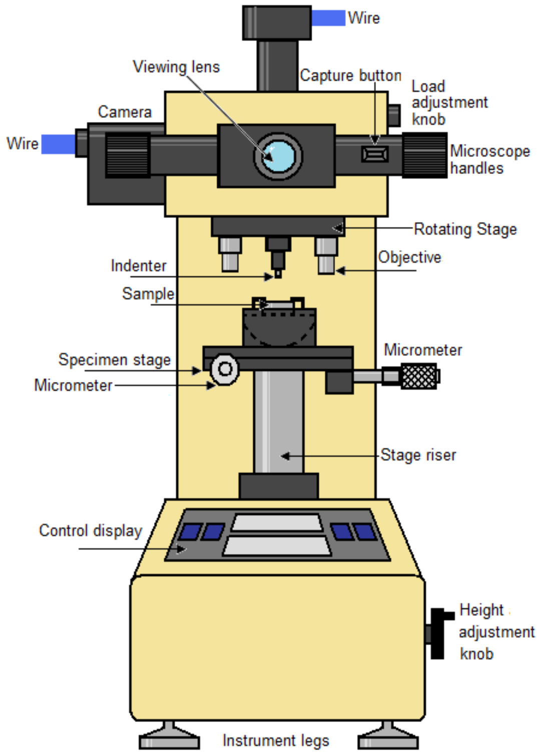

Figure 25 Schematic of a LECO Microhardness Tester Model LM 300AT with appropriate labels of its various parts

The specimen was loaded onto the sample platform which is capable of tilting to make the specimen level against the two holding tabs. This ensures that the indenter is applied on a level surface. The load and dwell times could then be adjusted by turning two different control knobs.

The 10X magnification objective was selected for this test. The location and size of indents were identified through two parallel lines having 0.1 μm resolution. The diagonal length and size of the indents were measured through adjustment of two lines through those divides. In order to select the location for the indentation, the microscopic lens was used to view the sample. A mechanism in front of the lens was marked with two adjustable, parallel lines which were used to aid in determining the diagonal measurements of the indentation later in the test. Once the location of the future indentation was set, a button was pressed on the instrument's control display in order to initiate the test. The rotating stage switched by motor from the objective lens to the indenter. The indenter was lowered and forced into the specimen at the prescribed load. Once the dwell time had elapsed, the indenter was removed automatically and the rotating stage switched back to the objective lens. The specimen was then viewed through the microscope. The adjustable lines were then moved using the microscope handles to mark the tips of one of the indentation's diagonals. The lines were able to be rotated 360° so that the diagonal could be made perpendicular to the lines. Once the diagonal was demarcated by the lines, the control display showed the length of the diagonal and the data capture button was pressed located on the microscope handles which saved the data to the instruments memory. The second diagonal was then measured in the same method as the first and was also saved. The instrument then averaged the diagonals and used them along with equation 6 to calculate the Vicker's hardness number. The test was repeated 75 times with the indentations made 0.015 inches apart in rows that were made 0.05 inches apart. This distancing was enough to prevent the indentations from corrupting each other. The distancing also served as a method of randomizing what phase the indenter landed on.

GSG-Al is composed of aluminum and GSG phases and the indenter could strike on one or the other or a combination of the two. The micro-indenter test was important to perform since the Rockwell hardness test hits on many different grains and phases at once. The micro-indenter can measure the hardness of the GSG and aluminum phases as well as what effects the grain boundaries have. The results for each phase could be skewed by taking a measurement of one phase which could be a thin layer atop a larger grain of a different phase.

3.8 Thermal Property Experimentation

The thermal properties of any material are important to consider, but it is even more important for magnetocaloric materials due to phase change and magnetization dependence on temperature. This section describes the experiments used to determine the thermal expansion coefficient of GSG-Al at high and low temperatures. Both temperature ranges required their own unique set-up. The procedures and reasons for the tests are described below.

3.8.1 High Temperature Thermal Expansion

The magnetocaloric material GSG is known to have a large expansion step at a temperature of around -6°C (T_c) when there is an absence of a magnetic field. [48] This means that rather than a gradual slope of increasing strain with increasing temperature, the GSG samples instead have a large jump in strain within the span of a couple of degrees. This jump is caused by the phase transition from the ferromagnetic orthorhombic crystal structure (temperature below the transition temperature, T_c) and the paramagnetic monoclinic crystal structure (temperatures above the transition temperature). [48] Prior to and after this sudden jump, the magnetocaloric material expands at a gradient that is more within the magnitude of common structural metals. [48] The expansion properties of GSG-Al were tested in order to see if the material was able to yield a similar jump in expansion within a small temperature change.

The first test was done in order to analyze the expansion properties at temperatures of 25°C to 185°C. This test is well out of the realm of the known phase change of GSG at -6°C; however, the range is within common operating temperatures of many possible applications such as automobiles. This test was conducted with a hot plate, a thermocouple, and a dial indicator with a 0.001 inch resolution. A schematic of the experimental setup is shown in Figure 26.

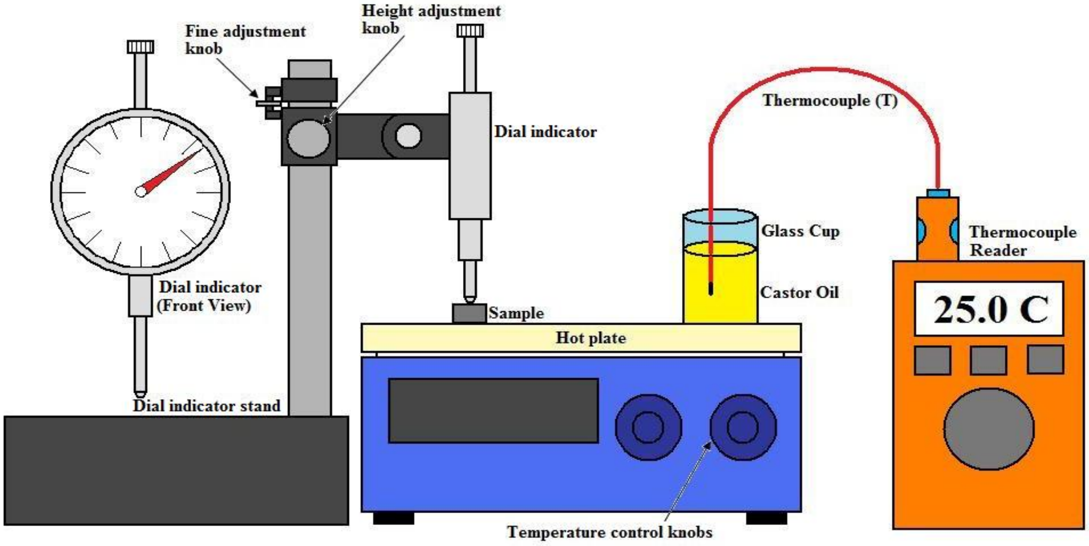

Figure 26 Experimental set-up used to determine the coefficient of linear thermal expansion for GSG-Al for temperatures ranging from 25°C to 185°C

A sample of GSG-Al was placed upon a hot plate. The sample was labeled with a point and an axis in order to ensure that the dial indicator hits the same spot on the sample every time a data point is logged and to keep the sample maintained at the same position/orientation on the hot plate. This point was necessary so that the height could be measured at the same point every time. In order to record temperature, a thermocouple and thermocouple reader were used. The thermocouple wires were coated in plastic by the thermocouple's manufacturer, so the end of the thermocouple was placed in a cup of castor oil in order to prevent the plastic from catching fire on the surface of the hot plate. Castor oil was selected since its boiling point is far greater than water's at 313°C and since it was readily available. This configuration meant that data points of temperature and length change had to be collected when the castor oil's temperature was at equilibrium. This is because the castor oil heats up slower than the metal sample and the temperature would have to stop changing in order for the temperatures of the sample and oil to be equal. In order to ensure that the temperature of the castor oil was comparable with the sample temperature, another thermocouple was intermittently placed on the surface of the sample to verify the temperature. Once the temperatures were verified as similar, confidence in the experimental set-up was reinforced. The initial height of the sample was recorded with the dial indicator when it was at room temperature (25°C). In order to prevent any error due to the expansion of the indicator, the indicator was kept from contact with the material (and thus the hot plate) until the data points were to be recorded. This also prevented any possible errors in dimension change due to the load of the indicator pin on the sample. Since the sample was placed upon a hot plate and since the dial indicator was zeroed on the hot plate, the expansion of the hot plate had to be brought under consideration. In order to determine the expansion of the hot plate, the indicator was used to monitor the height change of the hot plate as the temperature changed. The procedure for this part of the test is the same as the procedure used to determine the sample's expansion. Once the change in length per change in temperature for the hot plate was found the value was subtracted from the overall expansion of the system in order to determine the expansion of the GSG-Al sample. Due to the resolution of the indicator and the properties of GSG-Al, data points were collected every 30 to 40 degrees, which ensured that the change in length was able to be distinguished. The data points were compiled to obtain a plot of length versus temperature. The slope of this plot, along with the initial length of the sample was then used to calculate the coefficient of linear thermal expansion in the direction studied. The experiment was duplicated five times in order to obtain an average coefficient and a standard deviation of the results.

3.8.2 Low Temperature Thermal Expansion

The magnetocaloric phase transition of GSG has been determined to occur at a temperature of -6°C when a magnetic field is not applied to the sample. [48] When a field is applied, a Curie temperature close to room temperature can be achieved. Prior research has found that thermal expansion of the material experiences a large jump at the Curie temperature. [48] In order to determine whether or not this same transition occurs in the GSG-Al composite, the sample's dimensional changes need to be observed and analyzed as the temperature changes in a temperature range encompassing -6°C.

Prior analysis of the thermal expansion of GSG used a strain gauge combined with a SQUID magnetometer or a cryostat in order to obtain data. [47] Due to the absence of a Wheatstone bridge assembly for experimental use, the expansion had to be analyzed using other means. The schematic in Figure 27 represents the experimental set-up used to study the expansion of GSG-Al at low temperatures.

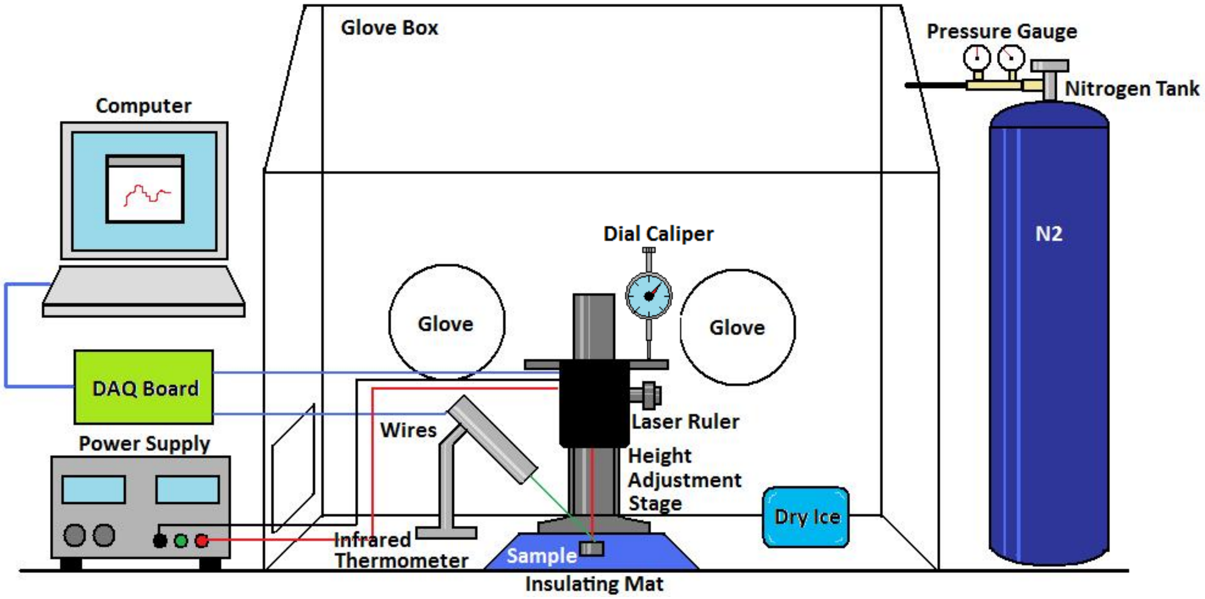

Figure 27 Experimental set-up used to measure the coefficient of thermal expansion of a sample of GSG-Al at low temperatures

The experiment involved the use of a laser ruler and an infrared thermometer. The laser ruler used feedback from a laser's reflection in order to determine a height change between the sample and the ruler's zero set point. The infrared thermometer determined the temperature by analyzing the infrared emissions from the GSG-Al sample. The thermometer used was set with an emissivity of 0.95. An emissivity is the ratio of the energy radiated by an object compared to a perfect radiator, or a blackbody [100]. A blackbody is denoted by the emissivity value of 1.0, while a shiny or very reflective object will have values nearing 0.0. An infrared thermometer was used due to issues dealing with contact. Thermocouples are very useful devices, however, mounting them to the sample would be difficult and surface connection would obtain an averaged value between the environmental temperature and the sample temperature. The IR thermometer would allow for non-contact advantages as well as ease of temperature data acquisition.

The ruler was calibrated to act within a range of 1/8” since thermal expansion rarely exceeds such a value for small temperature differentials. The ruler was calibrated using a dial caliper that was marked in the inch scale and had a resolution of 0.001”. The caliper was connected to the ruler and the height adjustment stage allowed for the ruler to be pushed up or brought down. The ruler was connected to a power supply that supplied 24 V to the device. The calibration began by pushing a button until an LED marked “Teach” turned on. The button was pushed again until the LED began to blink on and off, this action saved the position as the device’s new zero point. The height of the ruler was then adjusted by using the height adjustment stage. The stage was lowered until the dial caliper changed 1/8” from its original position. The ruler button was then pressed again to save this data point. The ruler was now calibrated to divide the 1/8” between the 0 to 10 V range of the device. This means that if the device outputs a change from 0 V to 1 V, the height would have changed 0.0125”.

The low temperature analysis of GSG-Al presented problems. Due to the humidity that exists in the laboratory, condensation and frost formation on top of the sample could have caused a problem in the analysis. If the laser was to reflect the change in height of the sample over temperatures ranging from negative Celsius temperatures to positive, formation and melting of frost on the top of the sample could affect the readings. In order to reduce this effect as much as possible, the experiment was performed inside a glove box that was supplied with nitrogen gas. The gas would dilute the amount of water vapor in the chamber and decrease the likelihood of condensation affecting the results.

The laser ruler and the IR laser were connected to a data acquisition board (DAQ) so that the voltages coming from the sensor could be collected in the computer programming and summed over time. The computer used software known as Labview in order to obtain and record the data coming from the sensors. The software could record and save multiple tests performed so that the data could be analyzed later.

The test was conducted by using dry ice to cool the sample of GSG-Al to a low temperature. The IR thermometer used had a minimum temperature limit of -18°C, so no temperature was valid until that threshold was surpassed. The sample was placed atop a block of dry ice for approximately 5 minutes in order to thoroughly cool the sample. The sample was then placed under the ruler laser and in the path of the IR beam. The sample was set upon an insulating pad so that heat transfer would not occur as rapidly as it would if it had been placed upon the plastic glove box surface. Prior to the initiation of data collection, the surface of the material was checked for frost or water layers that could corrupt the results and then the Labview program was initiated.

The program was allowed to run for approximately 8 minutes or at least until the temperature of the sample had increased to 7 or 8°C. This final temperature was decided upon due to the presence of dry ice in the glove box which lowered the environment temperature well below the room's ambient temperature of 19°C. The increase in temperature relied only upon the temperature differential between the sample and the surroundings and not upon any outside heating device. The tests were conducted a total of 5 times so that the accuracy of the data could be ensured.

The data was saved and then analyzed by plotting the height change of the sample versus the temperature. Certain parts of the plot were linear and by isolating these parts, the rate of height change as a function of temperature could be determined from the value of the slope. The slopes were then used to determine the coefficient(s) of friction that existed in this temperature range.

3.9 Measurement of Magnetic Properties

Magnetic materials as well as magnetocaloric materials are tested in magnetometers in order to determine the strengths of their magnetic fields and their reaction to externally applied magnetic fields. Since many materials' magnetic fields are strongly dependent upon their temperature, magnetometers often include temperature controls. Low temperatures are necessary due to some materials exhibiting a Curie transition temperature at temperatures approaching absolute zero. A commonly used magnetometer is a superconducting quantum interference device (SQUID) which is able to detect very low magnetic fields. [101] A SQUID is a vector magnetometer which means that the device is able to measure a magnetic field component in a certain direction while scalar can only determine magnetic field magnitude. [101] SQUIDs use either liquid helium or liquid nitrogen in order to cool the specimens to low temperatures. Liquid nitrogen can only lower the temperature of the apparatus to 77 K while liquid helium approaches absolute zero closely at 4.2 K. [101] A SQUID system is composed of three main parts: a superconducting magnet, a superconducting pick-up detection coil, and SQUID connected to the detection coil. [101] The superconducting magnet is a solenoid made of a superconducting coil that is maintained at low temperatures. The magnet applied a uniform magnetic field around the sample and can be adjusted. These magnets can produce fields as high as 18 T. [101] The detection coil is what is able to detect magnetization as well as moment and magnetic susceptibility in the sample under study. It is configured as a second-order gradiometer which detects the magnetic rate of change within the sample and is made from a single piece of superconducting wire. The SQUID is a very sensitive instrument and capable of detecting magnetic fields as low as 2E-9 emu. [101] The magnetic flux from the sample is able to create an electric current in the detection coil that is measured by the SQUID. [101]

The SQUID used in the study of GSG-Al was a Quantum Design PPMS 9T magnetometer and the tests were performed at Lawrence Livermore National Laboratory. A sample of GSG was studied along with the GSG-Al composite. The GSG sent for study was fabricated in identical fashion to the GSG contained in the GSG-Al composite. The magnetization versus applied magnetic field and the magnetic susceptibility versus temperature tests were performed on the GSG sample to analyze its magnetocaloric effect. Only 176.78 mg of GSG was needed for this analysis. The magnetization susceptibility test was conducted under an external magnetic field of 100 Oe between 250 K and 320 K due to the assumption of the Curie temperature being in that region. The magnetization susceptibility of the material should substantially drop as the temperature crossed the Curie temperature. Once the Curie temperature is passed the material changes from a ferromagnetic material to a paramagnetic material and cannot sustain the magnetization.

The magnetization test was conducted in a range of external field values between -60 kOe and 60 kOe and was performed at 3 temperatures: 270 K, 290 K, and 310 K. Magnetocaloric materials experience a decrease in magnetization as they approach their Curie temperature and progress into the paramagnetic region. When the field that the material is exposed to goes to zero, the magnetization of the ferromagnetic phase of the material is allowed to jump when no field is applied and begins to reverse orientation. When the material is in its paramagnetic phase, the jump does not occur.

A 129.86 mg sample of GSG-Al was also studied in the magnetometer; however, only magnetization versus temperature and magnetic susceptibility versus temperature tests were made. The magnetic susceptibility was performed under an external magnetic field of 100 Oe and within a temperature range of 5 K to 320 K. The magnetization versus applied magnetic field test of GSG-Al was performed in an external field range of -60 kOe to 60 kOe. Unlike the GSG tests, the magnetization effect was only performed at a temperature of 5 K.

3.10 Wear Tests

This section describes the wear tests performed on samples of GSG-Al and Al 6061-T651. Three types of wear tests are perform: low temperature, room temperature, and elevated temperature tests. A tribometer and an optical profilometer were used to determine the friction and wear rates of both materials at each temperature tested. The completion of these tests will determine the trend of friction and wear rates as a function of temperature.

3.10.1 The Tribometer and Friction Measurement

GSG-Al and Al 6061-T651 samples underwent wear tests using a tribometer. A tribometer is a device that can wear a surface by the use of a fixed abrasive on a moving platform that holds the material under study. A pictorial representation of the test system can be seen in Figure 28.

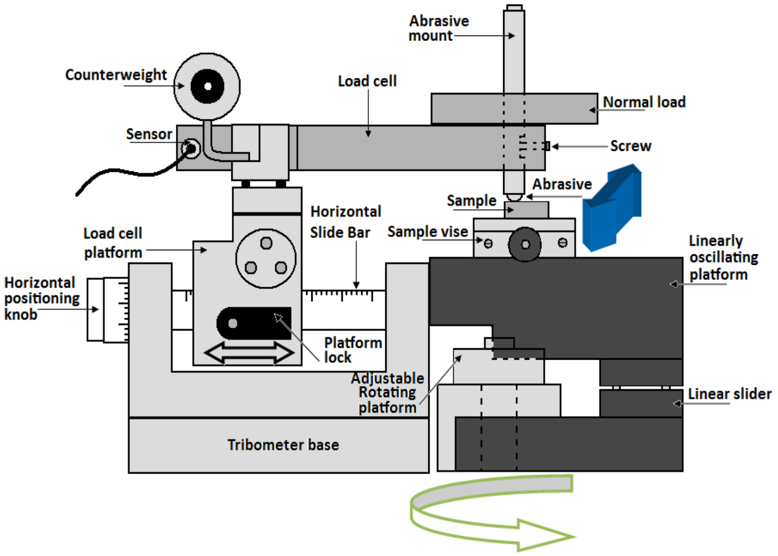

Figure 28 Tribometer test system set-up with linear oscillating platform. Arrows are shown to indicate possible motion of certain components

The abrasive, typically a ball bearing, creates wear tracks on the surface of the material if the material is not harder than abrasive.

A linear motion platform is used for this experiment. The amplitude of motion can be adjusted in millimeter increments. The tribometer can be used to determine the coefficient of friction of the material over time. When the abrasive pin slides on the surface of the material, a frictional force is enacted in the opposite direction of the motion. This force is detected in the load cell, which is calculated as a friction force in the computer program. Controlled loads can be added on top of the pin to serve as a normal load to the wear sample. The tribometer was used in a linear wear track configuration and the samples were tested dry, or without lubrication.

Three wear tracks were made on each sample so as to obtain enough data for an average for both the coefficient of friction and the wear rate. The sample was placed in the tribometer by securing it in the sample vise. The sample was leveled and tightly secured so that it could not be moved by the abrasive forces of the tribometer. The tribometer computer program was set to initiate linear wear at room temperature at a speed of 3 cm/s, with a half-amplitude of 4 mm, and with a load of 2 N. The abrasive object was a 6 mm diameter 52100 steel ball bearing (64 HRC). The load cell and abrasive mount were lowered onto the sample. A level was used in order to adjust the vertical position of the abrasive mount to a point at which the load cell arm was made level. Once the vertical position of the abrasive mount was obtained, the screw at the end of the load cell arm was tightened to secure the mount. The 2 N normal load was added to the top of the abrasive mount. Wear was initiated once the program was made to run. The samples were tested for approximately 1 hour or ½ an hour (depending on the temperature) to obtain a coefficient of friction with minimal variation with time.

Wear debris from the samples were saved to be studied under the TEM and data from the tribometer tests were saved (coefficient of friction versus time) to be analyzed later.

The analysis of the coefficient was broken into three parts: **(1)** tribometer program friction analysis, **(2)** positional analysis of the friction, and **(3)** Excel analysis using data from the tribometer. The tribometer program friction analysis is adjusted for linear mode which adjusts the reciprocating motion of the arm. This rectifies the signal and displays it on a position by position basis. Position is an important factor in that the velocity of the abrasive is different at each point due to the oscillation effects. The velocity is greater at the center than at the ends of the sample, thus creating dissimilar coefficients. Due to the velocity being closest to that of the defined parameter of 3 cm/s at the track's center, it was the focus of this part of the analysis and the data at that point was collected for each track. The second form of analysis was positional. The friction data at 5 different positions was noted for each track. For consistency, positions at 0 mm, 2 mm, 3.7 to 3.9 mm, -2 mm, and -3.7 to -3.9 mm were analyzed on each track (0 mm being the track's center). The range of 3.7 mm to 3.9 mm was ambiguous due to data being corrupted at the ends of the track due to an approximate velocity of zero. The mean, standard deviation, maximum, and minimum values were recorded for each of these points. Those values were then averaged to obtain a reasonable approximation for the friction properties over the whole of the wear track. The final analysis method employed the use of Excel. All the data from the tracks' tests were exported to Excel, there the data was rectified and a running average of every twenty data points was done in order to reduce the number of data points as well as their range on the plot. The plots are meant to provide a better approximation of the friction coefficient's transient performance when the entire length of wear track is considered. The samples were dismounted carefully to not contaminate the wear debris or surface. Wear analysis of the sample was performed on the wear tracks.

The same test was performed on a sample of 6061-T651 aluminum alloy so that the properties of GSG-Al could be compared with a known structural material. Since aluminum makes up 50% of the mass of the GSG-Al samples, it seemed logical to test the properties of a common aluminum alloy. Aluminum 6061-T651 is used commonly in such applications as couplings, hydraulic and brake pistons, and bike frames. [93] The fact that IC engines are now being made of aluminum alloys was also an incentive to use an aluminum alloy. Wear rates of various materials do exist in textbooks and charts, however, those wear rates are calculated through experimental methods that do not match those conducted on GSG-Al. Performing the exact same experiments on a common material provides wear rates that were free from many biases and errors that could have resulted due to experimentation dissimilarities. The key differences were the material studied and its properties.

The low temperature wear tests were performed in a similar method to the room temperature wear tests, but incorporated different items to aid in the reduction of temperature. Three different wear tests were performed in increments of 30 minutes. A reduction of test time was needed due to the short temperature time stability of the dry ice used to cool the system. Dry ice, or solid carbon dioxide, was use to cool the tribometer since its sublimation point is at -78.5°C. The test was set up as it is shown in Figure 29.

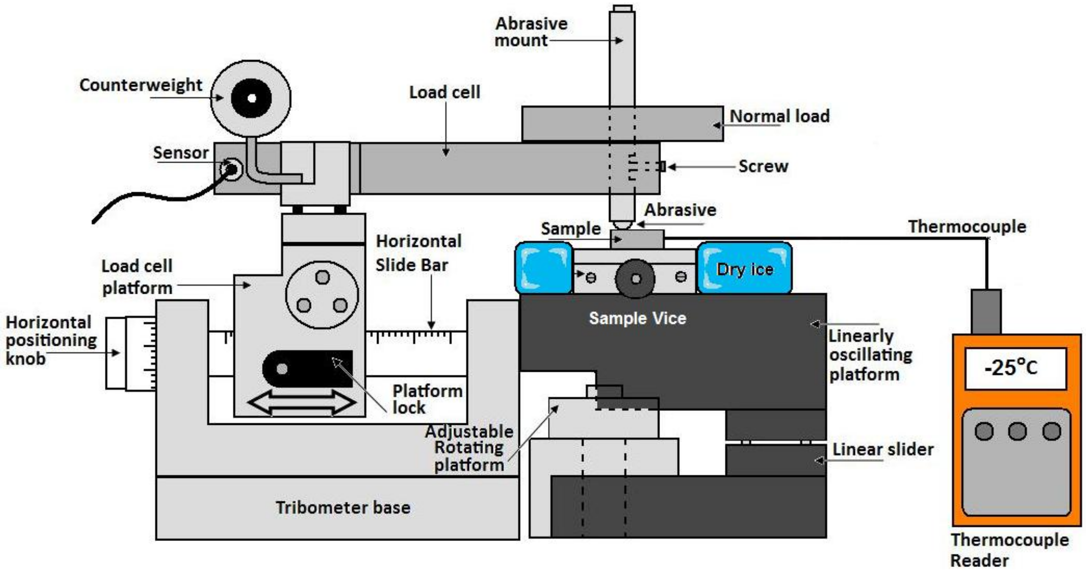

Figure 29 This is representative of the experimental setup for the low temperature tribometer tests. The setup is made up of the tribometer (left), linearly oscillating platform (center), thermocouple and reader (bottom right), and dry ice (center)

Such a low temperature source would aid in the reduction of the sample's temperature, but due to the temperature of the environment (apparatus and atmosphere) would average out to a higher overall temperature.

During the course of the test, the experimental setup was similar to the room temperature tests. In order to cool the specimen to a lower temperature, dry ice was piled on top of the linear oscillating platform and sample vise in order to cool the specimen. A thermocouple was connected to the sample vise so that the temperature could be monitored as the experiment progressed. The thermocouples end was wrapped in a layer of aluminum foil and then was slid beneath the sample. Throughout the experiment, the temperature was kept at a temperature of -25°C +/- 5°C due to the constant addition of dry ice to the experimental setup once other lumps of dry ice had sublimated. The temperature was continuously watched and monitored in order to achieve such a close tolerance. The temperature changes due to friction were not monitored.

One concern about the setup was that the moisture in the air would cool, condense, and then freeze on both the sample and the tribometer parts. In order to counteract this effect, the frost layer on top of the sample was scraped away prior to each test. The scraping was done by using a plastic rod that was wrapped in dust-free tissue paper to rub the sample up and down until the frost layer was mostly removed. This did not ensure, however, that moisture was removed from the sample, but it did reduce the probability that frost affected the coefficient of friction value and wear rate. The frost layer is problematic due to it affecting the running-in period or initial stages of transient friction. Also the moisture could increase abrasive and adhesive wear. Once the frost was removed, the tribometer's load cell was lowered and the abrasive tip made contact with the sample. The tip itself had been kept cool so that any temperature differences between the sample and the tip would be negligible. The tip was kept cool using pieces of dry ice. The tribometer program was initiated and the data was recorded for three separate test runs on both the GSG-Al and Al 6061-T651 samples.

The thermal wear tests were carried out with the same tribometer used in the wear tests at room temperature. The experimental system was altered by the addition of a Mica Thermofoil Heater from Minco. The thermal tribometer system is shown in Figure 30.

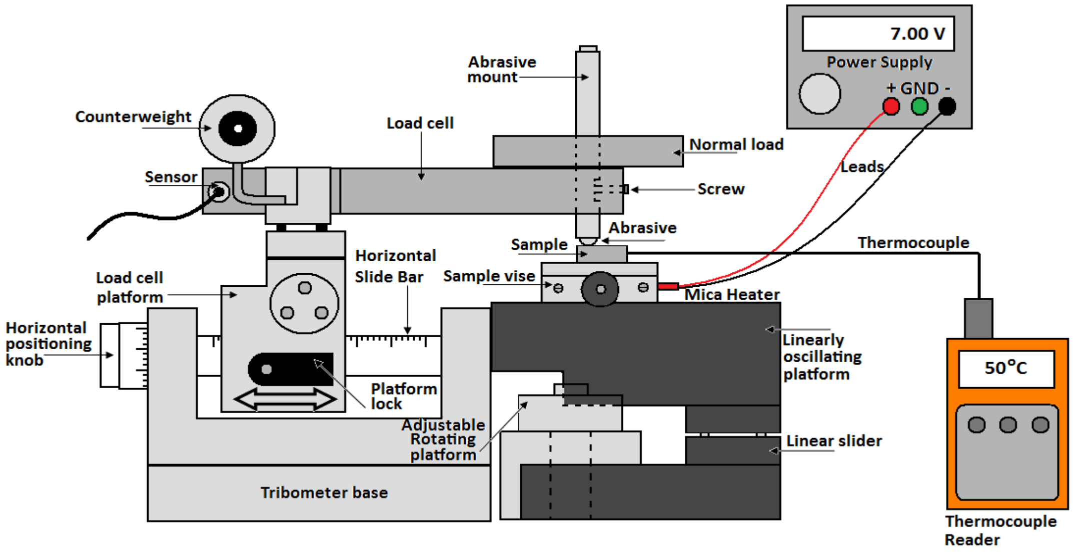

Figure 30 This is representative of the experimental setup for the thermal tribometer tests. The setup is made up of the tribometer (left), linearly oscillating platform (center), power supply (top right), thermocouple and reader (bottom right), and Mica heater (center)

The heater was attached to the base of the vise that holds the sample in place. The heater is circular and has a hole in its center so that a bolt and washer could be used to attach it to the sample vise. This vise is attached to the top of the linearly oscillating platform and secured using bolts so that no motion outside the desired linear direction is made. Prior to running the test, the sample was clamped in place, leveled, and heated to the desired temperature. The heater was equipped with positive and negative leads which were connected to the terminals of an AC power supply. The voltage from the power supply was constantly altered in order to make sure that the temperature was maintained to within 2 degrees of the actual temperature at 50°C and within 4 degrees of the actual temperature at 150°C. A T-type thermocouple was connected to the sample in order to measure the temperature. The thermocouples end was wrapped in a layer of aluminum foil so that it would have a conductive contact on all sides and then was slid beneath the sample. The wear test was run in the same way the wear tests were run at room temperature. The parameters that were input into the tribometer computer program were kept the same so that the room temperature and high temperature tests could be easily compared. The speed, half amplitude, scan rate, load, and test time were 3 cm/s, 4 mm, 10Hz, 2 N, and 1 hour respectively.

The first set of thermal wear tests was done at 50°C. The power supply was set between 7V and 8V in order to raise the sample to the test temperature quickly. Once the temperature was reached the voltage was lowered to around 4 to 5V in order to maintain a steady temperature. So that the temperature would be held within a certain tolerance, the voltage had to be slightly increased (+/- 1V) from time to time. The heating effects due to friction were not monitored. Three wear tests were performed at this temperature so that a decent average could be taken of the results. The same method was conducted for the thermal wear tests at 150°C. The voltage to the heater was turned higher in order to reach this high temperature; however, the same technique applied. Wear debris was gathered after every test so that TEM and EDS analysis could be performed on the debris at a later time. Thermal wear tests were also performed on a sample of Al 6061 T651. The tests were conducted in the same fashion and at the same temperatures (50°C and 150°C) as the GSG-Al samples so that comparisons could be made to a structural material of known mechanical properties.

3.10.2 Wear Tests

The wear of GSG-Al and Al 6061-T651 were determined by the use of a Zygo NewView 600S Optical Profilometer in order to determine the area of the wear scar cross sections. The system, shown in Figure 31, consists of a light source, lenses, a camera, a microscopic objective, a reference mirror, and beam splitters.

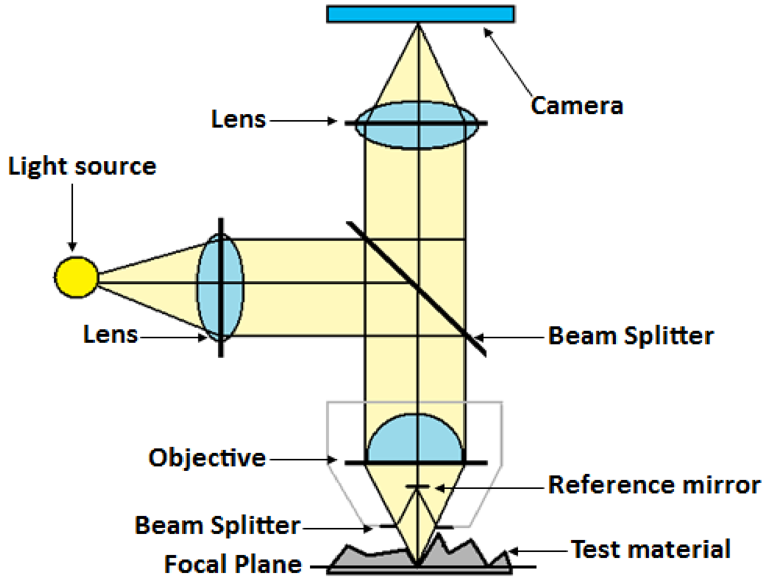

Figure 31 Optical profilometer functional representation involving interferometer functioning

Optical profiling uses the properties of light to determine the optical path differences between the reference mirror and the sample surface. The optical profilometer can be considered a specialized interferometer. A light source sends a beam toward a beam splitter which splits the beam in half. Half of the beam passes through the objective of a microscope and onto the reference mirror. That beam is then reflected back toward the camera. The other half of the light beam is sent through the objective and onto the test material. That beam is also reflected back toward the camera. The lower beam splitter is equidistant from the reference material and the focal plane of the test material. When the light beams from the reference material and the sample are combined in the camera, constructive and destructive interference occurs in the combined beam where the wavelengths of the light vary. A schematic of these types of interference are shown in Figure 32.

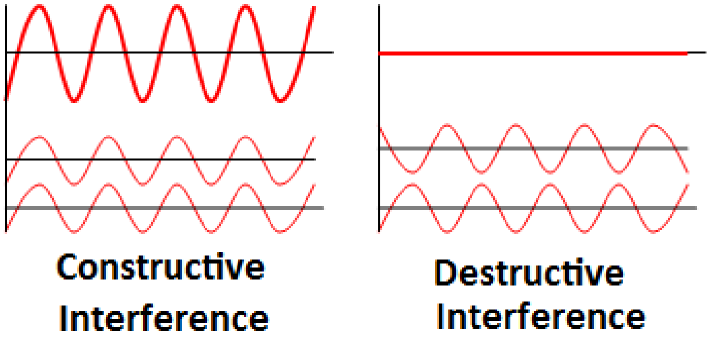

Figure 32 Constructive and destructive interference represented as sine waves. The upper waves of each type are a combined representation of the two bottom waves

This yields light and dark bands known as interference fringes. The transition from dark images to light images constitutes one half wavelength of difference between the reference light path and the sample light path. If the wavelength is known, the height across a surface can be calculated in fractions of a wave. A photograph of the interference fringes is shown in Figure 33.

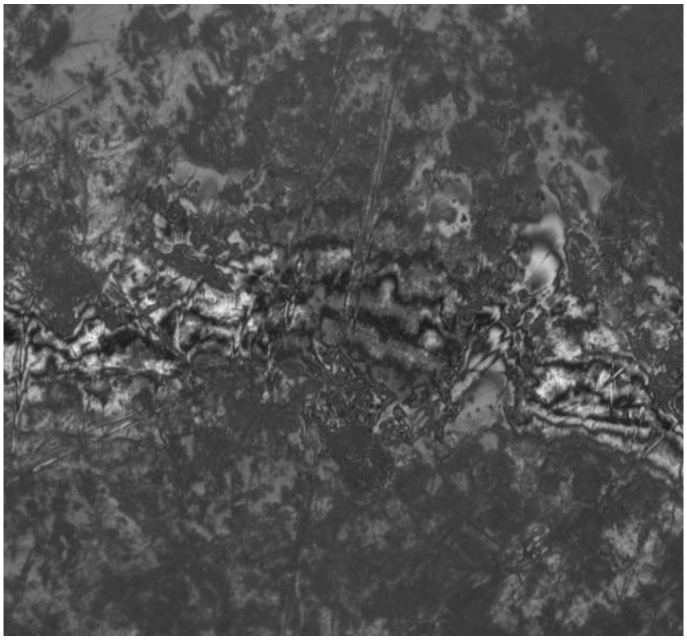

Figure 33 Photograph of the interference fringes caused by constructive and destructive waves

When using the profilometer, a microscopic objective was selected for the setup. For the tests performed in the research, an objective value of 10X was used due to the size of the wear tracks. The image of the material could be seen on the computer screen along with discolorations that represent the interference fringes. The microscope focus can be coarsely and finely adjusted. Adjusting the focus also moves the fringes along the image. In order to achieve the best possible profilometer images, the fringes need to be centered at a position where they are at a depth between the lowest point in the wear track and the unworn surface. The light source scanner would scan the surface of the material.

A scan length of 141µm (bipolar) was used to ensure that the sample surface was scanned at as great a depth as possible. The surface was measured as a plane and a low pass Fast Fourier Transform was selected as the filter in order to prevent unwanted high frequencies from corrupting the image. The camera was given a pixel area of 640 x 240 with a frequency of 72 Hz. The resolution of the instrument was set at 1.10 µm.

The profilometer was able to obtain several cross sectional views of the material which aided in the calculation of the average cross sectional area of the wear tracks. A screen image of the computer program used with the optical profilometer is shown in Figure 34.

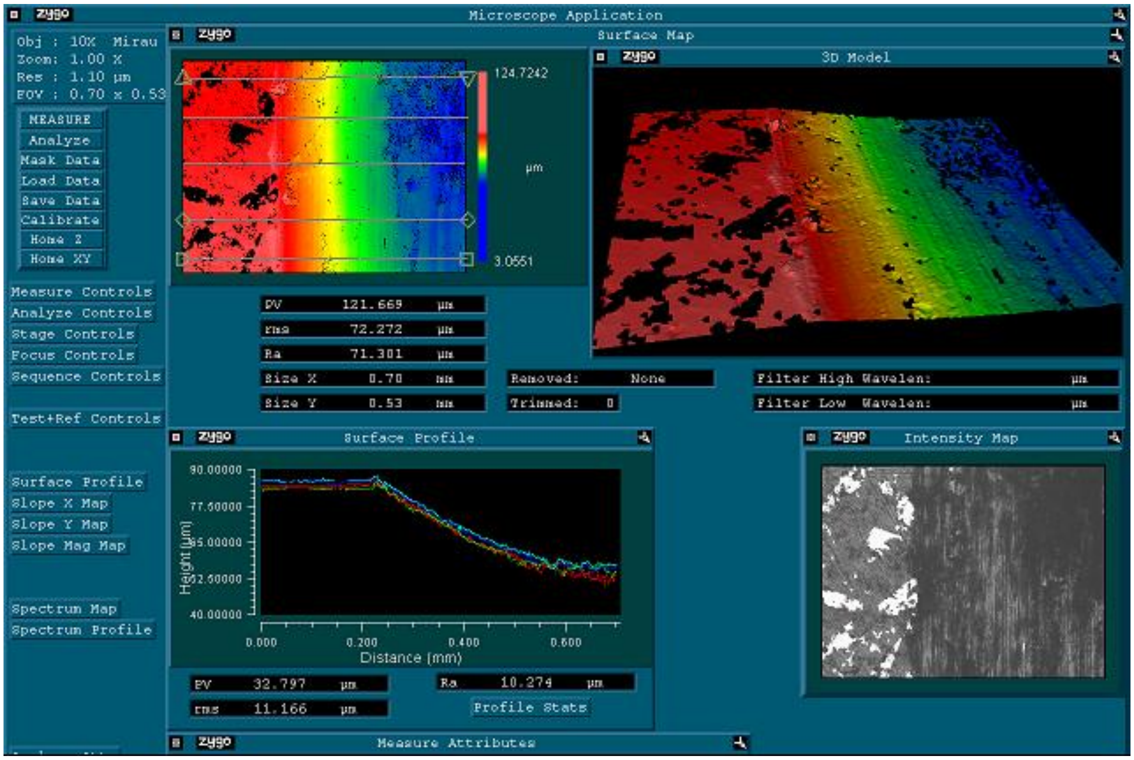

Obj : 10X Mirau
Zoom: 1.00 X
Res : 1.10 µm
FOV : 0.70 x 0.53

PV 121.669 µm
rms 72.272 µm
Ra 71.301 µm
Size X 0.70 mm
Size Y 0.53 mm
Removed: None
Trimmed: 0
Filter High Wavelen: µm
Filter Low Wavelen: µm

PV 32.797 µm
rms 11.166 µm
Ra 10.274 µm

Figure 34 Screen image of the Zygo Optical Profilometer computer program with surface 2D, 3D, actual, and profile images shown

The computer program displayed the 2D image of the sample with color coded height representation, a 3D image of the scanned area, a cross sectional view of the surface profile, and a camera image of the sample in black and white. Also displayed were the average surface roughness, RMS surface roughness, peak-to-trough distance, and test parameters. An example of the 3D image is shown by the scanned wear track in Figure 35.

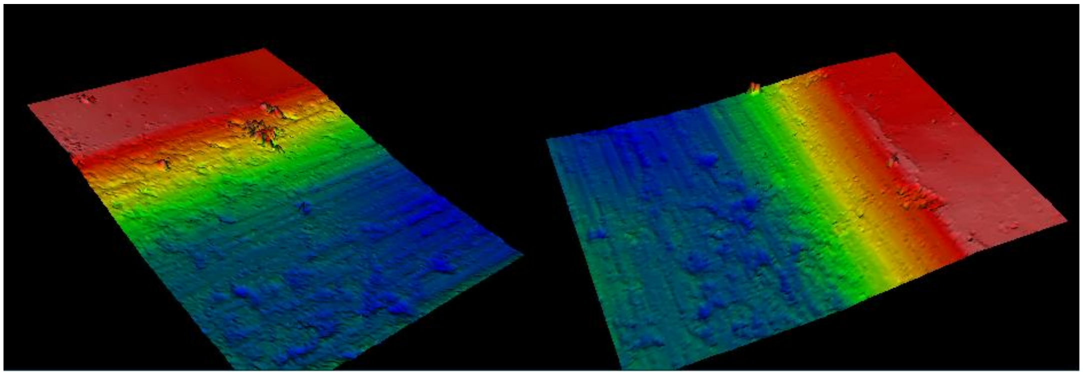

Figure 35 Example 3D image of the GSG-Al surface and wear track.
The two slides represent the left and right side of a section of wear track

The minimum magnification for the profilometer is 10X. This posed a problem in that the images of the wear track that were taken had to be broken into two segments in order to get the full track imaged. The 2D representation of the wear track was also taken by the profilometer. As with the 3D image, the 2D image had to be broken up into two segments in order to obtain the full wear track image. The 2D image of a wear track is shown in Figure 36.

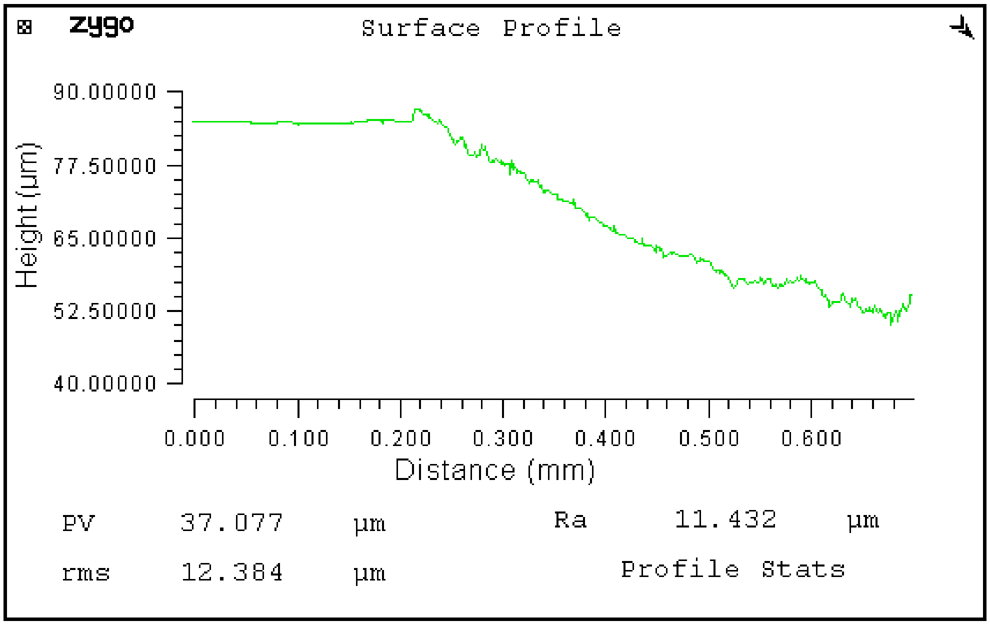

PV 37.077 µm

rms 12.384 µm

Ra 11.432 µm

Figure 36 Example image of the surface profile image displayed on the optical profilometer program screen. The profile represents half of the wear track on a GSG-Al sample

The profile in Figure 36 represents roughly half of the wear track. In order to obtain an image of the full wear track cross section, the two segments need to be combined to form one image so that an area can be calculated. An example of this combination is shown in Figure 37.

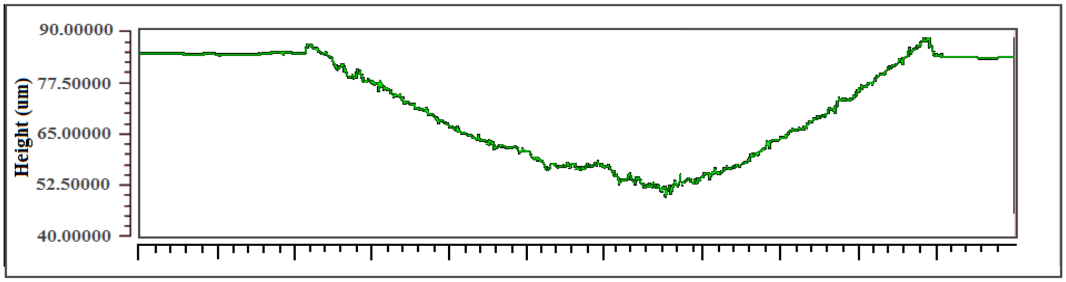

Figure 37 This is an example image of how the two halves of the GSG-Al wear track profiles were combined to form a profile of the whole wear track

The combination was accomplished by overlaying the two images upon one another and then matching up the similar features. This was done to several different cross sectional views so that an average could be calculated. The cross sectional area was calculated by means of trapezoidal integration, which is a method that approximates the area under a curve by means of drawing trapezoids whose areas are calculated and then summed. An example of trapezoidal integration is shown in Figure 38.

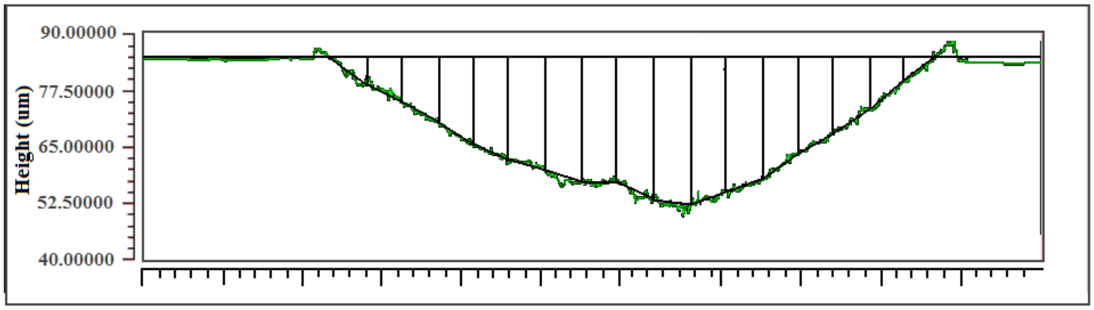

Figure 38 This is an example image of how trapezoidal integration was applied to wear track cross section of a GSG-Al sample in order to obtain the cross sectional area

The accuracy of the trapezoidal method increases as the number of trapezoids in the region increases. An average wear rate could be calculated by taking into consideration the wear scar length and the 2 N load using the following equation.

$$Kwear = V_{wt} \div (F_N \cdot L_S) \qquad (7)$$

where K_{wear} is the wear rate, V_{wt} is the wear track volume, F_N is the normal load applied to the sample, and the L_s is the wear length (68.8 m/hr). By using the trapezoidal integration method to analyze the wear track profiles found using the optical profilometer, the track volumes were able to be calculated by multiplying the cross sectional areas by the wear track lengths (8 mm).

3.10.3 Mechanisms of Wear Tests

The wear rate is an important property to determine for a material and as well as the initial wear. There are several common forms of wear, but three are considered highly probable in the wear tests conducted on the GSG-Al and Al 6061-T651 samples: abrasive wear, adhesive wear, and surface fatigue. [102] Abrasive wear occurs when a harder material rubs against a softer material and abrasion occurs on the materials (primarily the softer material) in the forms such as plowing, cutting, or fragmentation. Adhesive wear is initiated when two surfaces rub against each other and a portion of the matter from one material adheres to the surface of the other. Adhesion wear can be triggered by a number of things such as high wear speeds, high environmental temperatures, or materials with low melting points.[102] Heat is a key factor in that softened materials tend to plastically deform which is a principle cause of adhesion.[102] The wear type of surface fatigue is an important wear mechanism to consider since the tribometer abrades a material in a cyclic fashion. This fatigue, caused by the ball bearing abrasive forming a wear track, can cause cracks to form and then propagate into secondary cracks. If the cycles continue, the cracks can cause large pieces of the material to come loose and add to the wear debris. Cracks and pits are indicative of the fatigue form of wear.[102] Wear can be helped or hindered by many things. Oxidation of the material's surface, moisture on or around the sample, temperature, and the relative hardness between the abrasive and the sample are all factors that attribute to the sample's wear rate and can change the dominance of one wear mechanism over another.[102]

Samples of GSG-Al and Al 6061-T651 were studied under an optical microscope after they were tested in the tribometer at the temperatures of 25, 50 and 150°C. Under high magnification, the samples were analyzed for distinct characteristics that would indicate the form(s) of wear mechanism that affected the materials. The samples were analyzed along with their respective ball bearings so that both contact surfaces could be scrutinized.

CHAPTER IV

EXPERIMENTAL RESULTS

This chapter consists of the results obtained from the tests discussed in Chapter 3. The chapter begins with the physical and structural properties of the samples and then moves in to the results that deal with various mechanical and thermal properties of the samples. The last section of this chapter displays the friction and wear rate results in differing temperature ranges for both the GSG-Al and Al 6061-T651.

4.1 Materials

The GSG-Al samples were prepared as 5 gram samples of a 1:1 mass ratio of aluminum to GSG. GSG-Al samples appear as shown in Figure 39.

Figure 39 GSG-Al cylindrical sample approximately 16 mm in diameter

In order to obtain samples that do not expand greatly during sintering, the applied force used to create the samples in the die needed to remain above 178 kN (20 tons). Samples that were formed under lower forces tended to be more porous and often had large air pockets.

4.2 XRD Results

Prior to testing, the XRD profile of GSG-Al was expected to have the combined profile of GSG and aluminum represented on the plot due to the nature of the sintering process. The spectra of prepared GSG-Al samples are shown in Figure 40.

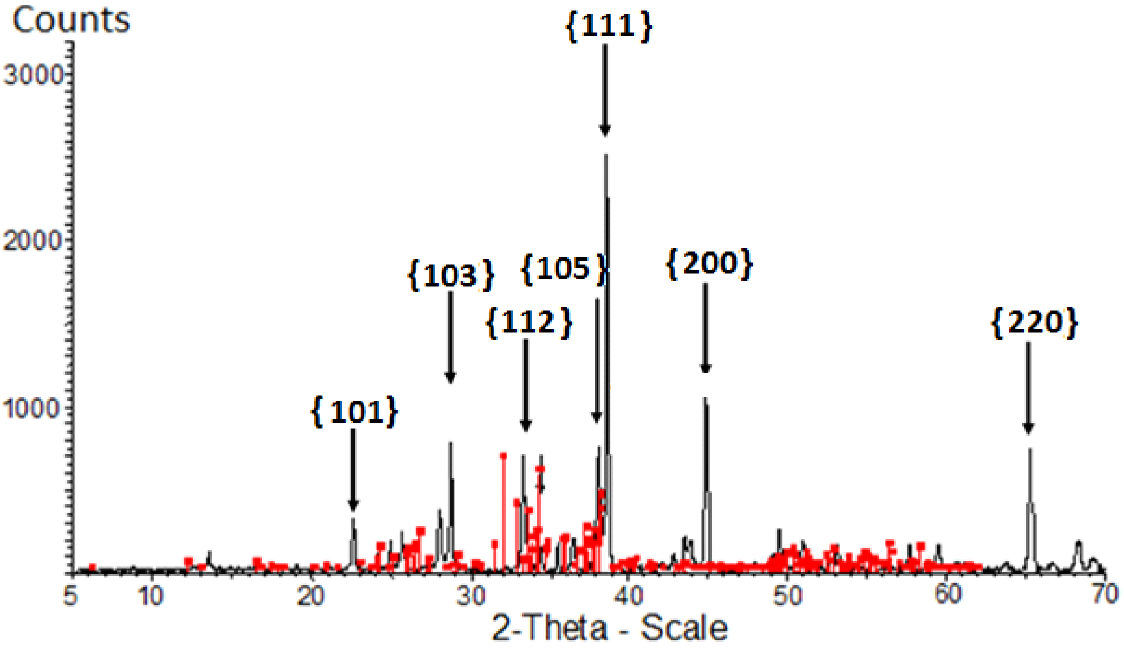

Figure 40 XRD phase profile of GSG-Al (black) with the GSG phase profile (red)

Here the X-axis is 2 times the angle (θ) of the X-ray source's position relative to the sampleand Y-axis is the intensities of reflected X-rays hitting the diffraction detector. The black plot is representative of the GSG-Al peaks and red represents the GSG phase peaks that are representative of GSG phases stored in a software database. The plot indicates the presence of GSG in the sample, but a substantially less quantity than what was originally added prior to the sintering process and the bonding of GSG and Al. Examing the sample XRD for traces of aluminum was the next step. Figure 41 plots GSG-Al versus known aluminum XRD peaks.

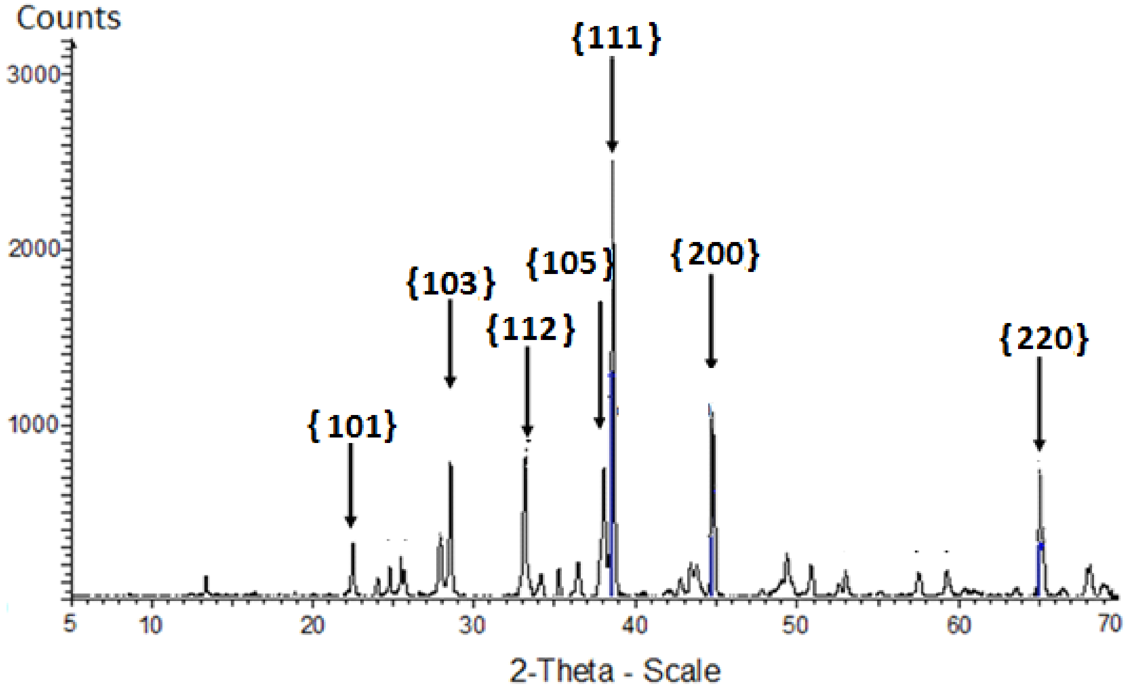

Figure 41 XRD phase plot of GSG-Al (black) with the phase profile of pure aluminum (blue)

Here the X-axis is the 2θ scale and the Y-axis is the count of X-rays hitting the detector. The aluminum metal exhibits only three XRD peaks and all coincide with peaks mapped during the XRD test of GSG-Al. In order to identify the remaining peaks, XRD peak identification software was used for further anaysis of the peaks. Results are shown in Figure 42.

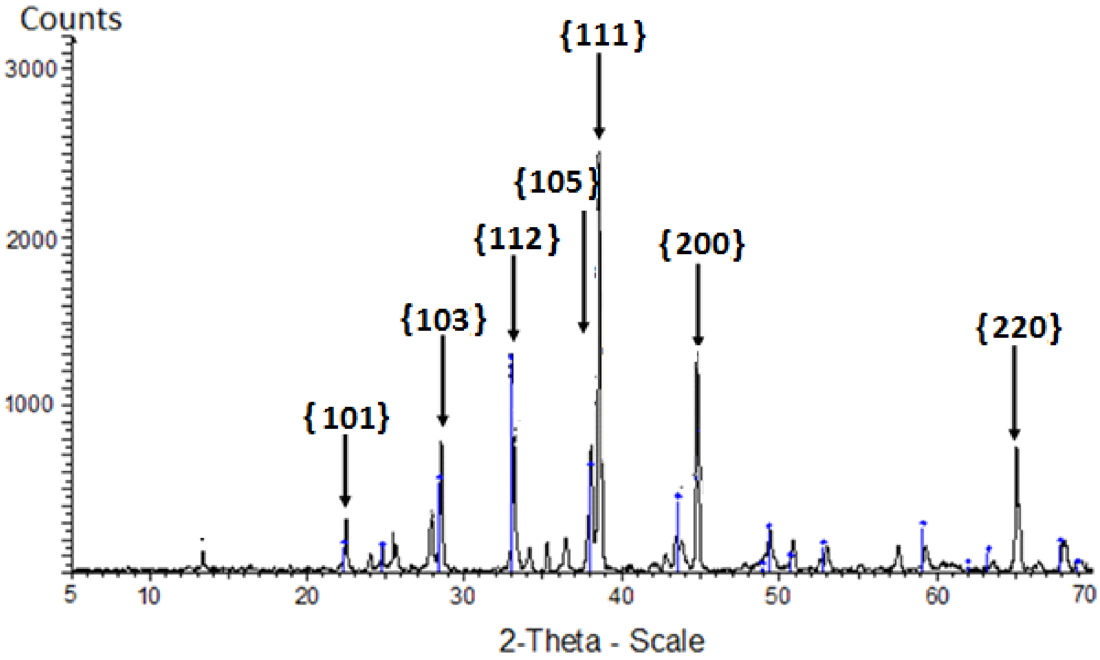

Figure 42 XRD phase profile of GSG-Al (black) with the phase profile of Aluminum Gadolinium Germanium (blue)

According to the standard peaks shown in Figure 42, the compound called aluminum gadolinium germanium (AlGdGe or GdAlGe) was found. The compound is known to have a significant magnetization and relatively high Curie temperature. [91] Table 3 identifies the peaks at 2θ angle locations for each of the constituent compounds.

Table 3 Constituent compounds and the peaks at which these materials are indicated on the XRD plots

Constituent Compound		
GSG	**Al**	**GdAlGe**
2θ angle	**2θ angle**	**2θ angle**
24	38.5	22
25	45	25
26	65	29
33		33
34		38
35		44
36		49
37		51
38		53
49		59
51		63
53		68
58		69

4.3 Surface Roughness

The ten tests performed on a sample of GSG-Al produced the roughness results. The GSG-Al was polished in the same method to other samples and its roughness is thus consistent with all other GSG-Al samples tested. The ten tests were averaged in order to gain an estimate of the overall surface roughness characteristics of the material. The average roughness (Ra) was calculated to be 0.4812 µm and the root mean square roughness (Rq) was calculated to be 0.6535 µm. The standard deviation for the average roughness was 0.0897 µm, which is 18.6% of the average value.

The Abbott-Firestone bearing curves for each of the ten tests were compiled into one plot so that the curve could be analyzed. The bearing curve is shown in Figure 43.

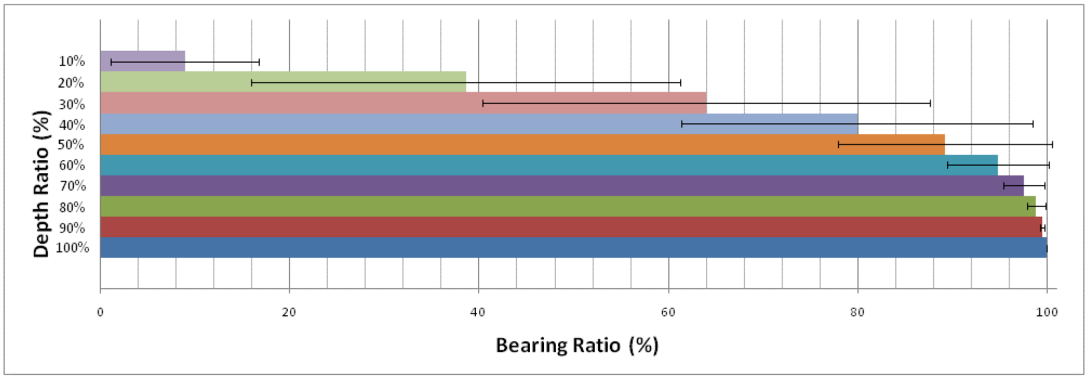

Figure 43 Abbott-Firestone curve for the average of 10 roughness tests on a GSG-Al sample

The depth ratio is the value obtained through equation 8.

$$R_{depth} = (1 - (H_{br} / H_{max})) \cdot 100\% \qquad (8)$$

where H_{br} is the height of bearing ratio line and H_{max} is the distance between the highest peak and the theoretical demarcation of a perfectly smooth surface. The curve had a wide data range which can be seen by the large standard deviations indicated by the error bars. The standard deviation of the roughness decreases as the depth ratio increases.

4.4 Microstructure

The GSG and Al particulate used to form GSG-Al was analyzed under a microscope prior to the sintering process. It was found that the GSG particles were sharp and appeared dark relative to the aluminum powder. Although GSG, Al, and GdAlGe each exist in the composite as indicated by the XRD results, the sharp and dark particles represent the GSG phase. However, the GSG particulate and aluminum phase will be less pure due to the formation GdAlGe. A digital picture of a sample of GSG-Al under 100X magnification is shown in Figure 44.

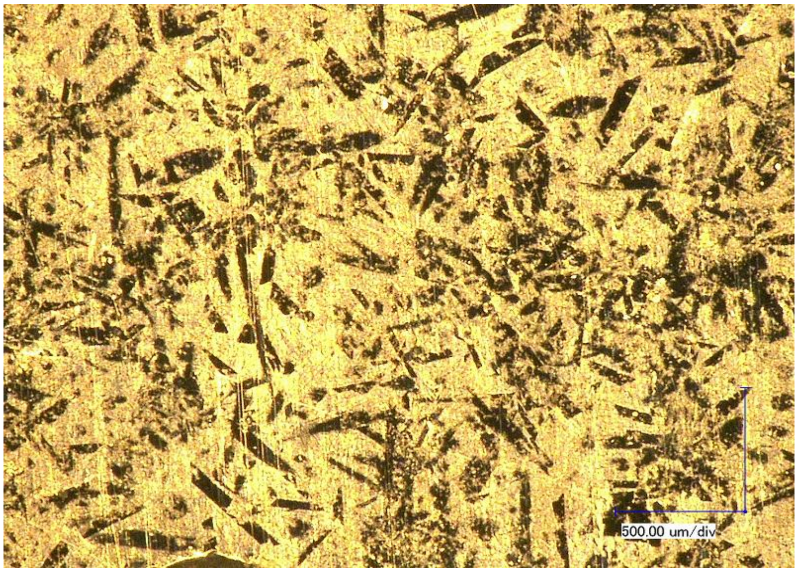

Figure 44 GSG-Al sample magnified 100X with the GSG phase showing up as the sharp and darker phases and the aluminum rich phase being represented by the golden portion

The GSG and aluminum portions of the sample can be easily distinguished from each other. The sharp grains that appear darker in the image are GSG grains while the slightly golden material surrounding these GSG grains is largely aluminum. The image was loaded into the Image Tool program in order to obtain a black and white pictorial representation of the photo. The average percentage of black pixels (GSG) was 31.11+/-4.60% while the average percentage of white pixels (aluminum) was 68.89+/-4.60%. This means that aluminum takes up the most area at roughly two-thirds of the sample while GSG makes up the other third.

4.5 Hardness Test

This section presents the hardness results from the tests performed on GSG-Al and Al 6061-T651. GSG-Al was tested using both the Rockwell scale and the Vicker's microhardness test, while aluminum was only tested in the Rockwell scale. Both materials showed large differences in their hardness values and the consistency of those values.

4.5.1 Rockwell Hardness

The superficial Rockwell tests performed on GSG-Al and Al 6061-T651 yielded the data presented in Figure 45 with error bars that represent twice the standard deviation. The Rockwell hardness for the GSG-Al sample was much less than that of Al 6061-T651 and it was also far more varying in its value.

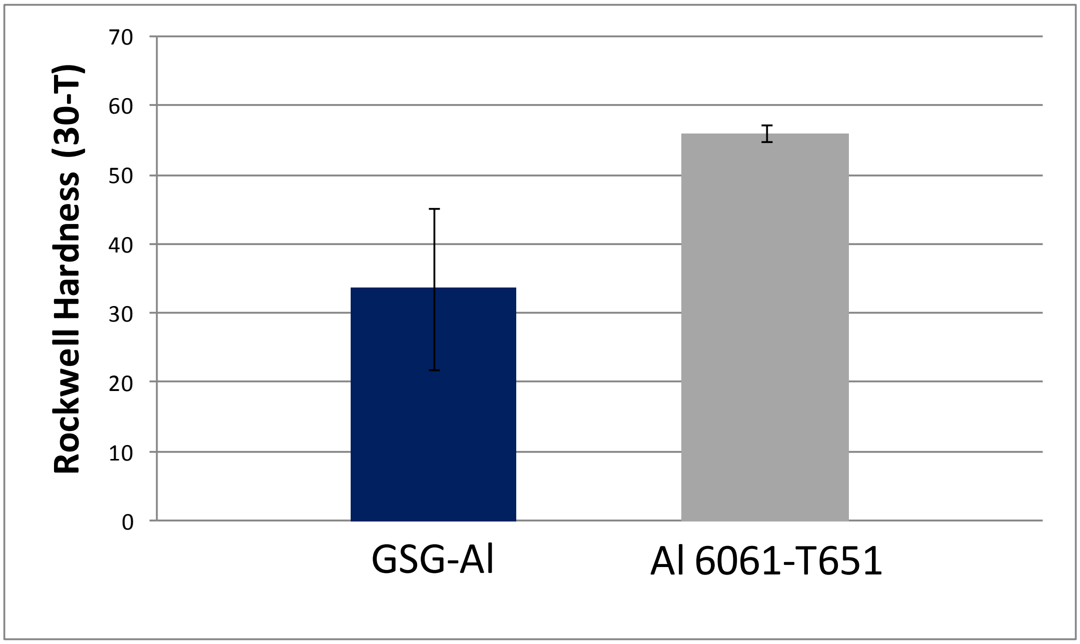

Figure 45 Hardness tests results for GSG-Al and Al 6061-T651
performed by employing the use of a Rockwell superficial 30-T test

From the error bars it can be seen that the standard deviation in the GSG-Al is quite large. This can be attributed to the several possible reasons such as the sintering process, multiple phases, porosity, and the fact that the sample was not made in a factory under highly controlled conditions. Hardness tests are supposed to be performed many times on each sample in order to obtain a good average for the data. Due to the sample size, however, the number of tests that could be conducted was limited. The Al 6061-T651 was tested 20 times, while the GSG-Al sample was tested only 12 times.

4.5.2 Vicker's Micro-Indentation Hardness

The Vicker's testing was carried out at multiple points on the sample. The indenter struck in a region that was all or mostly aluminum 42 times, it struck in a region that was all or mostly in a GSG phase 17 times, and it struck a mixed region (composite) with apparently equal phases of GSG and aluminum 16 times. These points yielded data with greatly varying values of Vicker's hardness. Figure 46 shows the average hardness of the aluminum, GSG, and composite phases.

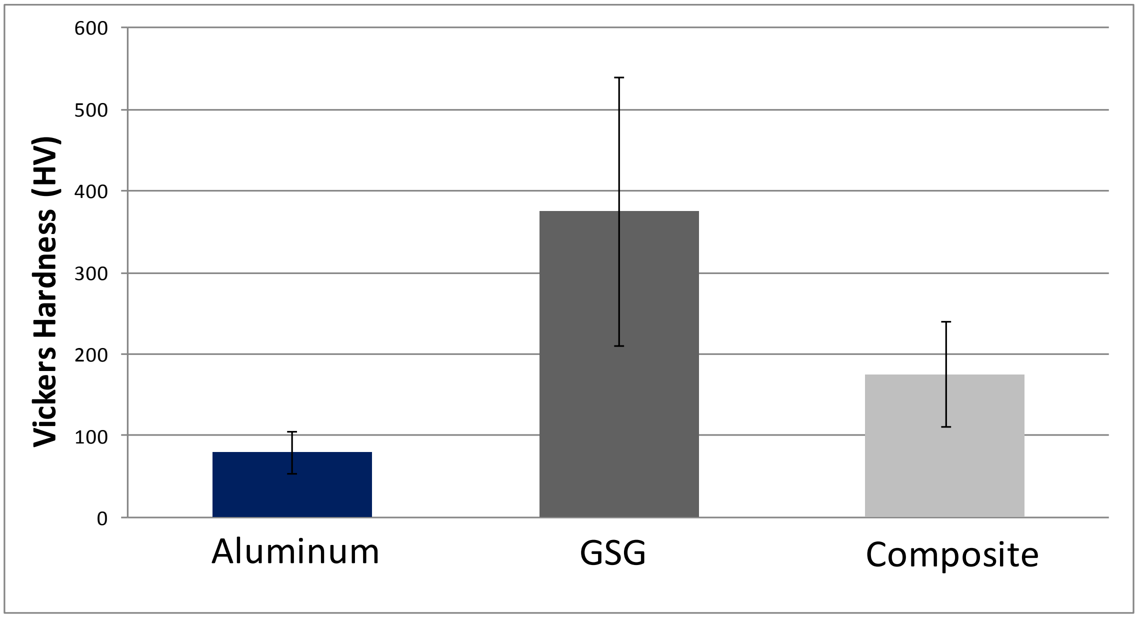

Figure 46 The average values of Vickers micro-indentations on GSG-Al in regions of mostly aluminum, mostly GSG, mixed regions of GSG and aluminum phases, and averaged results

The most visible characteristic about the plot is the large standard deviations (error bars). It is interesting to note that the GSG phases are harder than the aluminum phases by a large amount. A separate test was done later that involved indentations at the center of GSG phases in order to more accurately study the hardness of pure GSG without the interference of aluminum. This test yielded an average hardness of 505.5 HV with a standard deviation 74.9 HV.

4.6 Thermal Expansion

4.6.1 High Temperature Thermal Expansion

The GSG-Al expansion tests were conducted five times in order to obtain an average expansion rate. Figure 47 contains the average linear plot with standard deviation error lines that represents the data obtained.

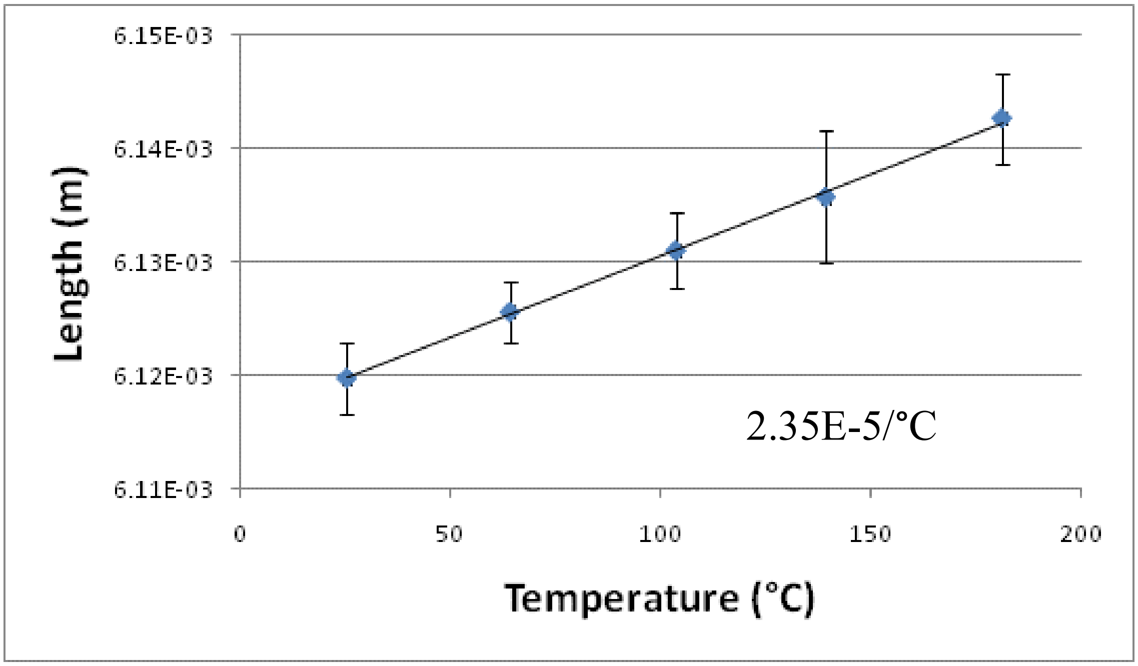

Figure 47 Coefficient of linear thermal expansion plot of GSG-Al that shows the change in length with increasing temperature from room temperature

The tests were tightly controlled so that the dial caliper hit the same point on the sample and so that the sample did not change location with respect to the hot plate's surface. The important parameter to focus on was the slope of the lines. This slope was the change in length per change in temperature. The average slope value was calculated to be 1.43E-7 m/°C with a standard deviation of 9.20E-9 m/°C. The coefficient of linear coefficient was calculated by dividing the slope by the initial length of the sample, 6.12E-3 m. The coefficient was calculated to be 2.35E-5/°C with a standard deviation of 1.38E-6/°C. The result was comparable to the expansion coefficient for aluminum which typically averages around the value of 2.3E-5/°C.

4.6.2 Low Temperature Thermal Expansion

Five thermal expansion tests were conducted on a sample of GSG-Al within a temperature range of -18 to 8°C. The test was necessary in order to determine whether or not the GSG within the sample expanded due to a phase change. The phase change for GSG occurs at a temperature of -6°C (267 K). Figure 48 shows the plot of the height change in a sample of GSG-Al over a temperature range of 27°C (27 K).

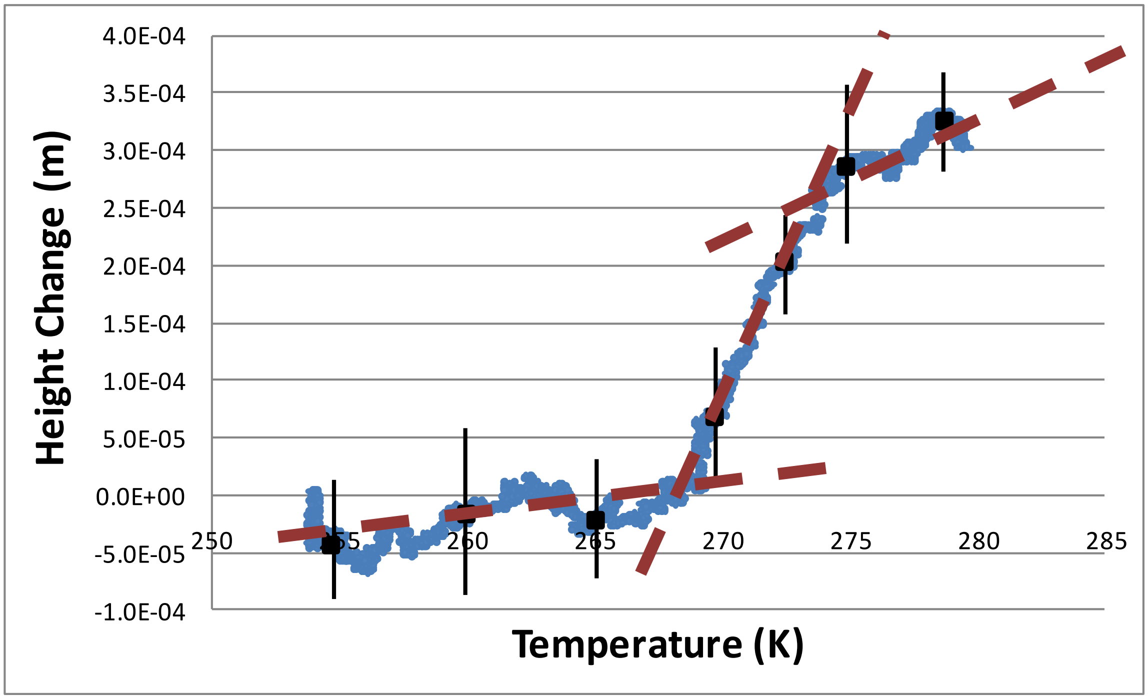

Figure 48 Plot of the averaged values of five tests conducted to determine the expansion of GSG-Al between temperatures of -18 and 8°C

The initial point of the tests was given a value of zero for its height while all the points following that are deviations from that value. Within the temperature range between -18°C and -8°C (255 K and 265 K), the height oscillates and it is hard to tell the trend of expansion in that region. The plot begins increasing again at around -7°C (266 K) and then rapidly increases between -5°C and 5°C (268 K and 278 K). This rapid expansion is better defined in Figure 49.

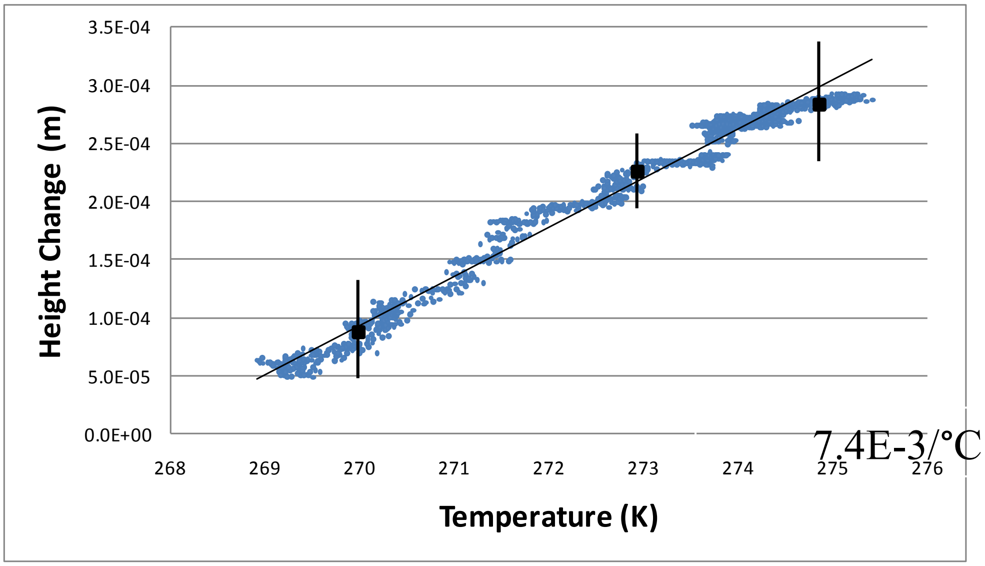

Figure 49 Rapid expansion zone of the GSG-Al sample (-4°C to 2.5°C (269K to 275.5 K))

This rapid increase is common in all five tests conducted on GSG-Al confirming the trend within the material. Using the slope of the plot in Figure 49 a coefficient of thermal expansion can be determined for this region. The slope was found to be 4.22E-5 m/°C (m/K). When this value is divided by the initial height of the sample (5.7 mm at -18°C (245 K)) the coefficient of thermal expansion is found to be 7.4E-3/°C (1/K) with a standard deviation of 2.45E-3/°C (1/K).

4.7 Magnetic Tests

4.7.1 GSG Magnetic Tests

The GSG magnetic tests conducted with a magnetometer gathered 2 plots of data: magnetization as a function of the applied magnetic field and magnetic susceptibility as a function of temperature. The plot of the magnetization as a function of applied magnetic field is shown in Figure 50.

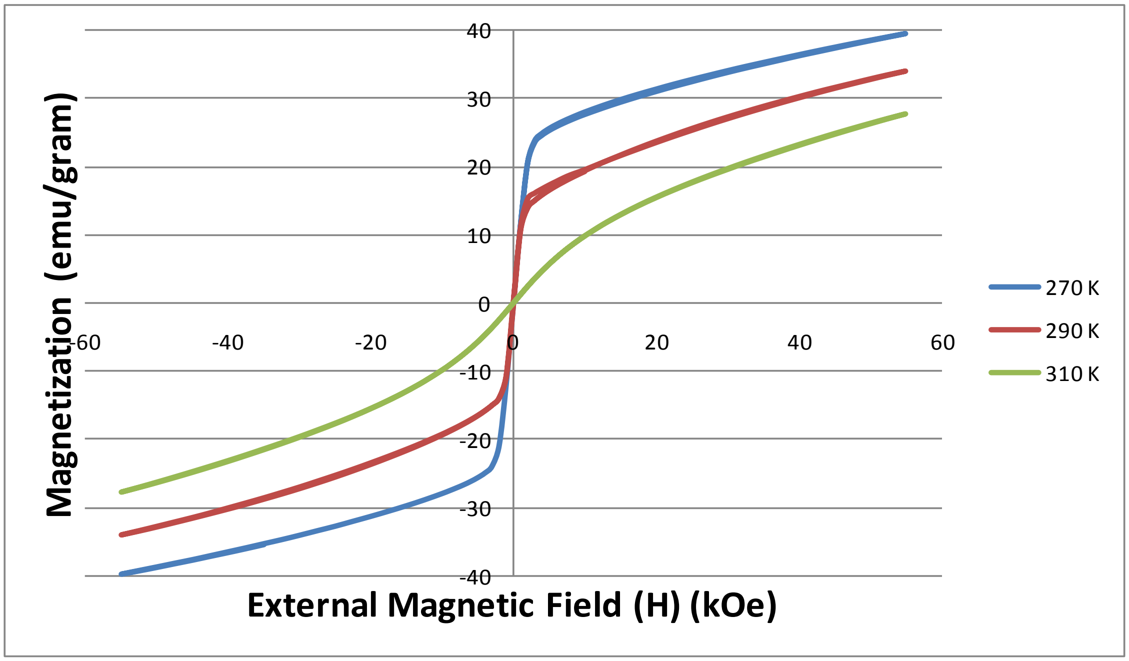

Figure 50 Plot of the magnetization of GSG versus an applied magnetic field used to study the magnetocaloric effect of the material

Figure 50 has three different trend lines representing the temperature at the time of the test. The temperatures below the transition temperature of GSG (27°C (300 K)) show a sharp change in the magnetization as the applied magnetic field approaches zero. The magnetization at temperatures above the transition point show a much more gentle change as zero is approached from both ends of the plot. The hysteresis of the plot, specifically at -3°C (270 K), is minimal and far less than the standard applied field (100 Oe) to get GSG to have a Curie temperature of 27°C (300 K).

The plot of the magnetization susceptibility as a function of temperature is shown in Figure 51.

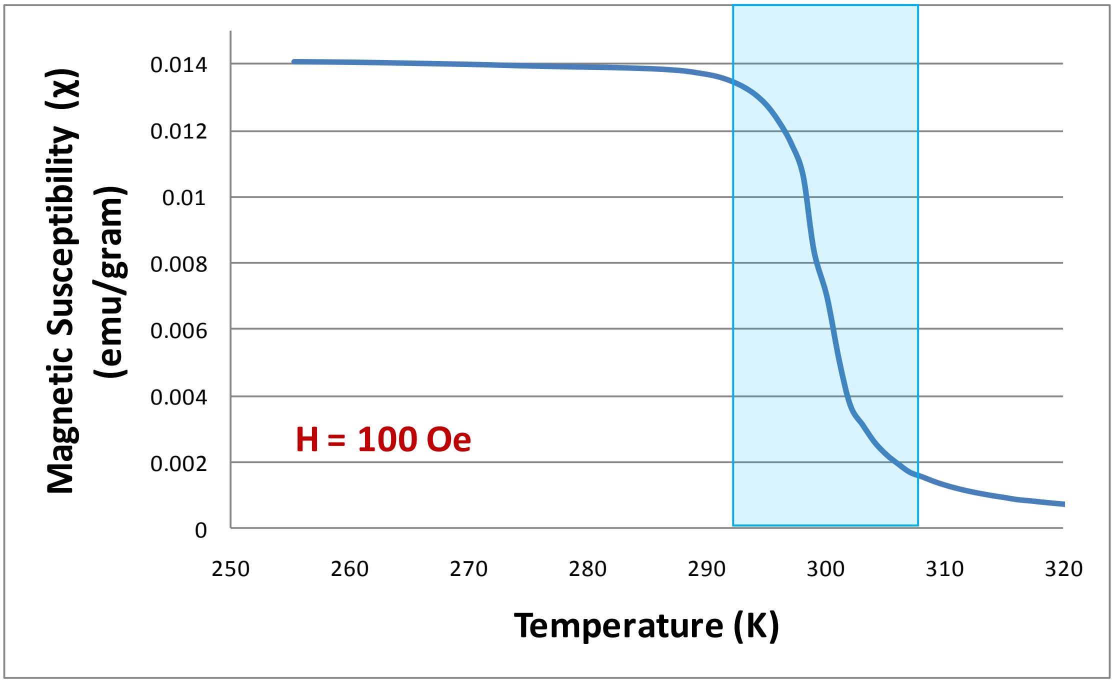

Figure 51 Plot of magnetization susceptibility versus temperature for a sample of GSG which aids in determining the strength of the magnetocaloric effect and the temperature at the Curie point

The magnetic susceptibility was relatively constant at around 0.014 emu/gram until the sample was brought close to the Curie transition temperature. Once the sample reaches this temperature, the magnetic susceptibility decreases rapidly until it almost approaches 0 emu/gram. The slope of the rapid drop takes place within the bounds of 14°C (K).

4.7.2 GSG-Al Magnetic Tests

The GSG-Al magnetic tests conducted with a magnetometer gathered 2 plots of data: magnetization as a function of the applied magnetic field and magnetic susceptibility as a function of temperature. The plot of the magnetization as a function of the applied magnetic field is shown in Figure 52.

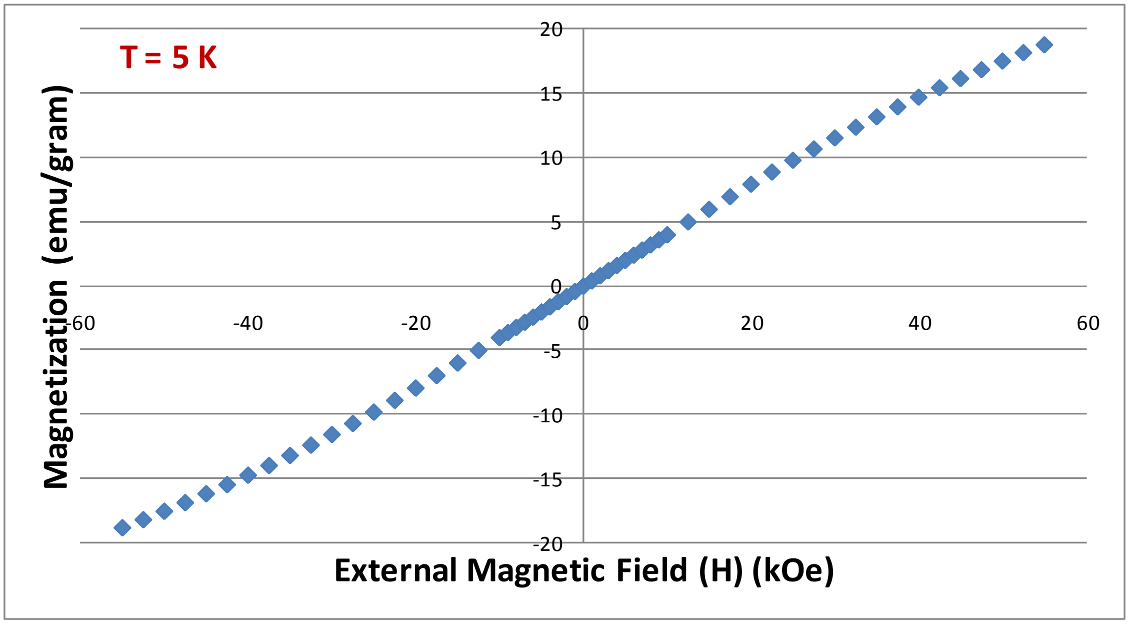

Figure 52 Plot of the magnetization of GSG-Al versus the applied magnetic field at 5 K for use in determining the existence of the magnetocaloric effect

The plot of the magnetization of GSG-Al at 5 K is comparable to the same plot for GSG at 37°C (310 K). The magnetization does not quickly shift as the external magnet field converges to zero as in the GSG temperatures at -3°C (270 K) and 17°C (290 K). The graphs indicate a strong difference between the magnetic behaviors of the two samples even though they both contain GSG. The plot of the magnetization susceptibility of GSG-Al is shown in Figure 53.

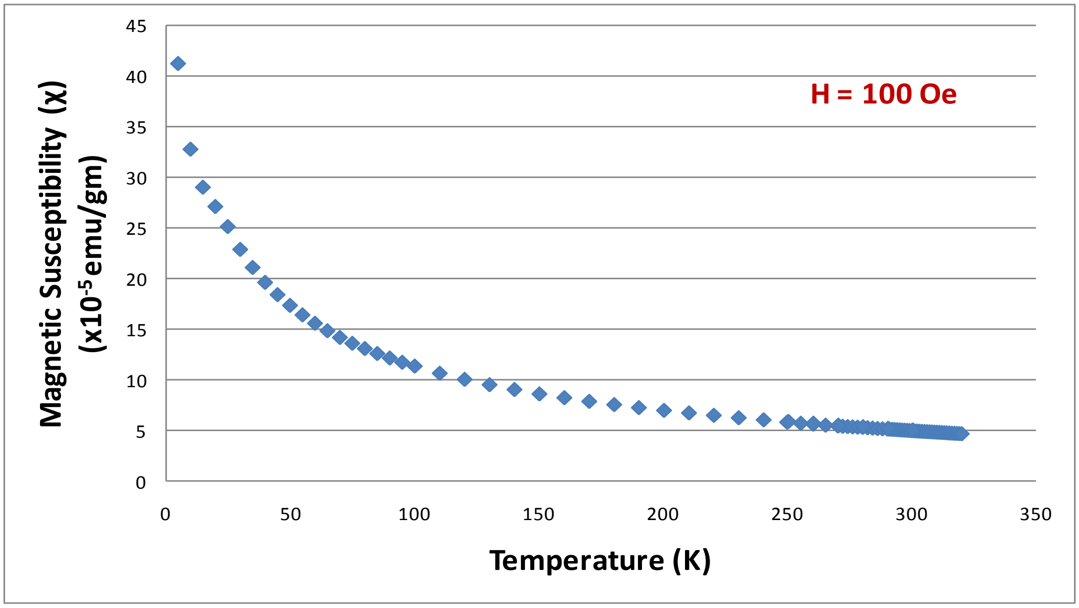

Figure 53 Plot of the magnetization susceptibility of GSG-Al versus the temperature used to study the magnetocaloric effect of the material

The magnetization susceptibility of GSG-Al bears no resemblance to the plot for GSG. The scale for GSG-Al susceptibility is two orders of magnitude lower than the GSG plot and shows no Curie temperature in the region of 300 K. The Curie temperature according to this plot seems to be very close to absolute zero.

4.8 Tribology Experimentations

4.8.1 Coefficient of Friction

GSG-Al samples were worn via a 52100 steel ball bearing abrasive connected to a tribometer. The abrasive was applied to the sample at temperatures of -25°C, 25°C, 50°C, and 150°C. The coefficient of friction for the GSG-Al and Al 6061-T651 differed in their trends at lower temperatures and this continued up into the higher temperatures. Testing the two materials at lower temperatures and for a shorter amount of time brought out challenges due to the moisture issues and the fact that there was not enough time for the frictions to settle to a constant value. The overall results may be skewed due to average coefficient of frictions being determined prior to settling time. Figure 54 shows a sample of GSG-Al worn at -25°C.

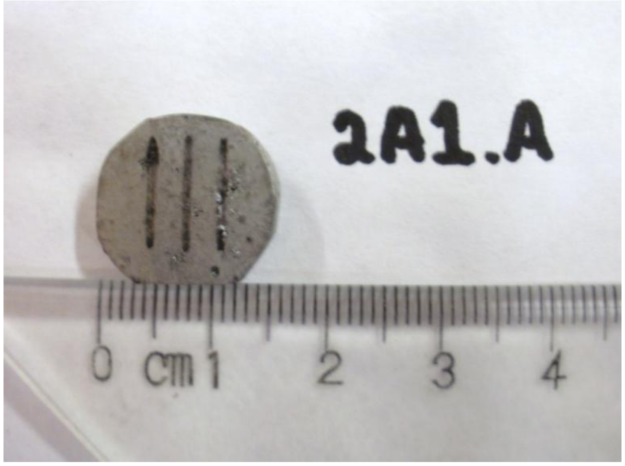

Figure 54 Sample of GSG-Al worn at a temperature of -25°C for 30 minutes with 3 wear tracks

The transient behavior of the coefficient of friction for the -25°C test was analyzed through the compilation of 3 tests. The plot of the average of these tests is presented in Figure 55.

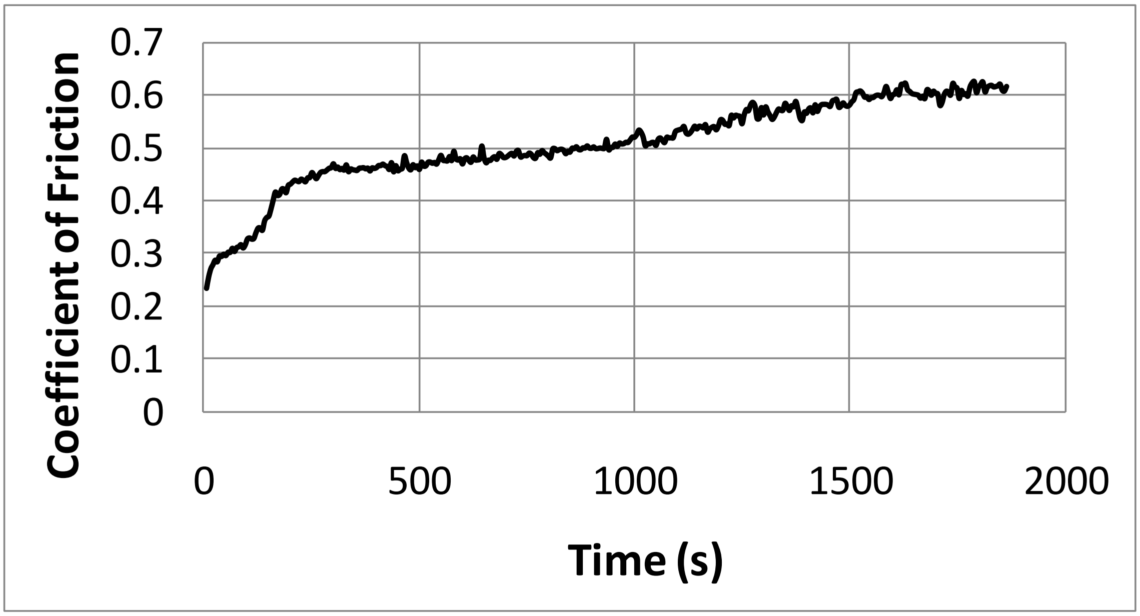

Figure 55 Transient performance of the coefficient of friction for GSG-Al composed of the average of three tracks made at a temperature of -25°C with a test length of 30 minutes

The three tests were relatively consistent, especially at times greater than 400 seconds due to the complications caused by frost and moisture on the sample surface and the running-in period. It is clear from the figure that the coefficient of friction has not yet settled. In order to obtain a reasonable value for the average coefficient of friction, the last 6 minutes of data was taken as a stabilized zone. The average coefficient of friction for GSG-Al at -25°C was determined by averaging the data points from the stabilized zone and was found to be 0.61 with a standard deviation of 0.013.

The coefficient of friction for a temperature of -25°C is virtually equal to that coefficient at room temperature. However, it is important to realize that the room temperature test had more time to settle and the -25°C test may actually be quite larger. For comparison, Al 6061-T651 was tested at this cold temperature. The same complexities and challenges in testing and interpretation existed for this material as well. Figure 56 shows a sample of Al 6061-T651 worn at -25°C.

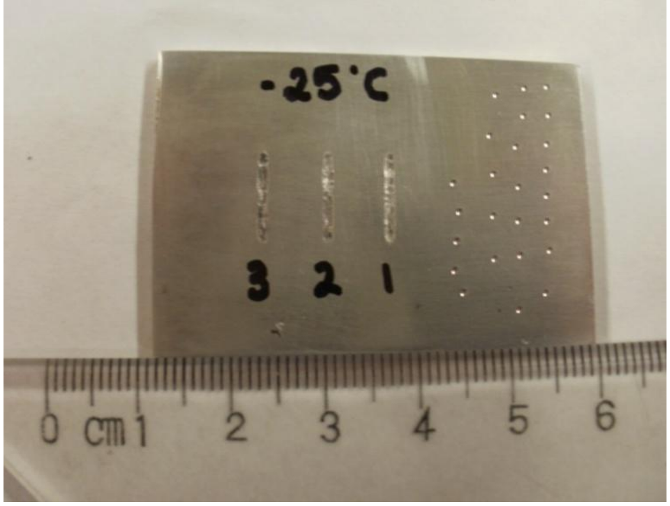

Figure 56 Sample of Al 6061-T651 worn at a temperature of -25°C for 30 minutes; 3 wear tracks are on the left and hardness test indentations are on the right

The transient behavior of the coefficient of friction for the -25°C test was analyzed through the compilation of 3 tests. The plot of these tests is presented in Figure 57.

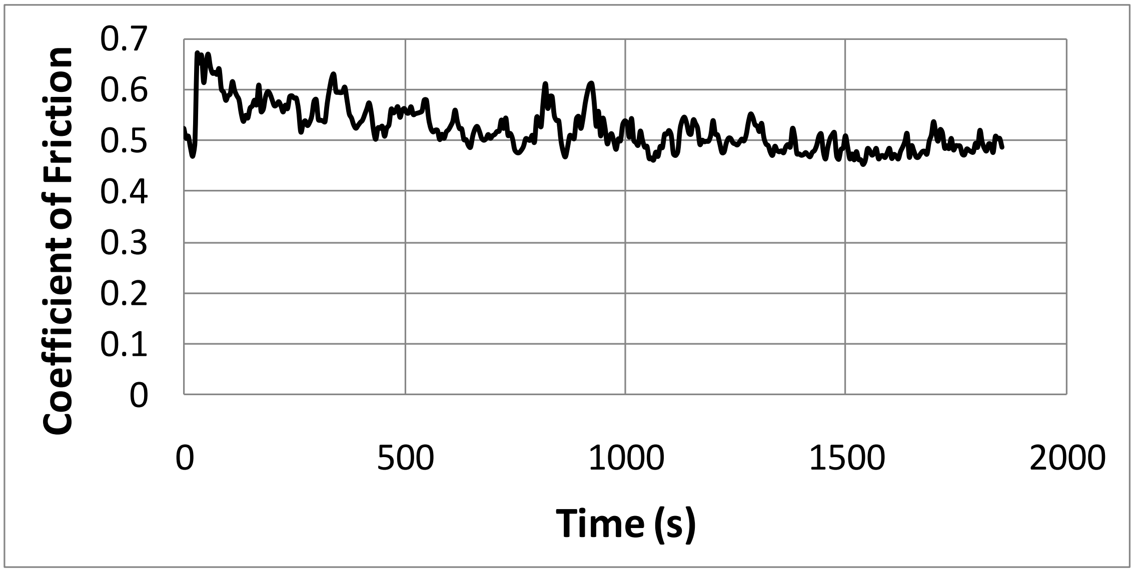

Figure 57 Transient performance of the coefficient of friction for Al 6061-T651 composed the average of the three tracks made at a temperature of -25°C with a test length of 30 minutes

The coefficient of friction with time for each test was consistent. Averaging the three test plots into one plot and then restricting that averaged plot to the final 6 minutes of testing yielded the region used to determine the final average coefficient of friction for Al 6061-T651 at -25°C. The average coefficient of friction for the aluminum sample was found to be 0.48 with a standard deviation of 0.016. The coefficient of friction for the Al 6061-T651 sample at -25°C was greater than that of the room temperature coefficient; however, as with the GSG-Al sample, the average coefficient may be inaccurate due to the shorter testing time.

For the room temperature tests, conducting wear tests with the tribometer for one hour allowed for the coefficients of friction to come to a consistent value. The transient behavior of the coefficient yielded a plot with a gentle growth of magnitude until the value leveled off to a steady state value at an average of 35 minutes into the test. The coefficient data of the last 25 minutes of all six tests were then compiled to form an average. The average coefficient of friction of GSG-Al at room temperature was calculated to be 0.610 with a standard deviation of 0.0265.

When the coefficient of friction is compared to that of Al 6061-T651, the coefficient of friction is higher for the GSG-Al. The stabilized region of the Al 6061-T651 sample worn at room temperature was limited to the last 25 minutes. The average coefficient of friction for Al 6061-T651 was calculated to be 0.432 with a standard deviation of 0.051. Figure 58 compares the room temperature coefficient of friction analysis for GSG-Al and Al 6061-T651.

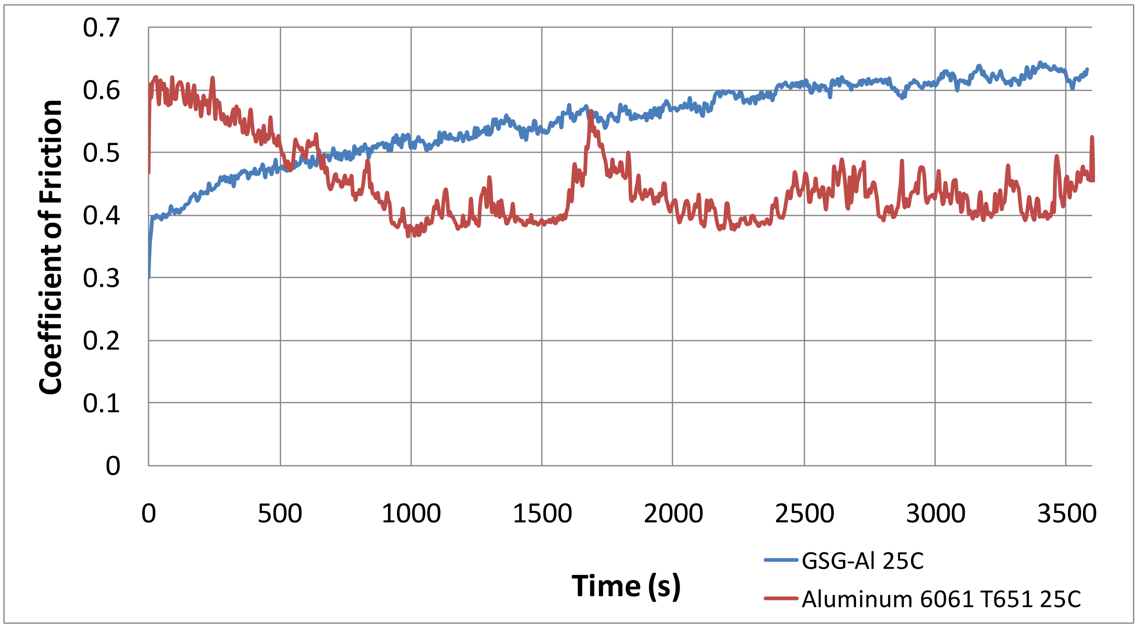

Figure 58 Plot comparing the transient trend of the coefficient of friction for both GSG-Al and Al 6061-T651 worn at room temperature

This plot shows the relative stabilities of the two types of materials. It is apparent that the aluminum alloy creates a far more unstable curve than that of GSG-Al due to the long running-in period of approximately 17 minutes. GSG-Al has a significantly shorter running in period, but a gradual increase in friction. At that point the plot maintains a relativily even magnitude with time even though oscillations still exist, notably the one that occurred between 1500 and 2000 seconds into the testing. The tendency for the Al 6061-T651 to decrease its coefficient with time is different from the GSG-Al, which slowly increases.

The higher temperature tests of GSG-Al at 50°C and 150°C yielded important results. The 50°C test had coefficient values that were more stable than the room temperature tests. For consistency, the last 25 minutes of the tests were used to determine an average of the coefficient of friction. The average coefficient was calculated to be 0.434 with a standard deviation of 0.001. The 150°C test was far less stable and did not achieve a stability region until 3 hours of testing had elapsed. The last 25 minutes of 150°C plot were averaged. The average coefficient for the 150°C was calculated to be 0.551 with a standard deviation of 0.013. The transient behavior of the coefficient of GSG-Al tested at temperatures of 25°C, 50°C, and 150°C can be observed in Figure 59 and Figure 60. The plots in Figure 59 are averaged plots of six tests at 25°C and six tests at 50°C. Figure 60 is an averaged plot of three tests at 150°C.

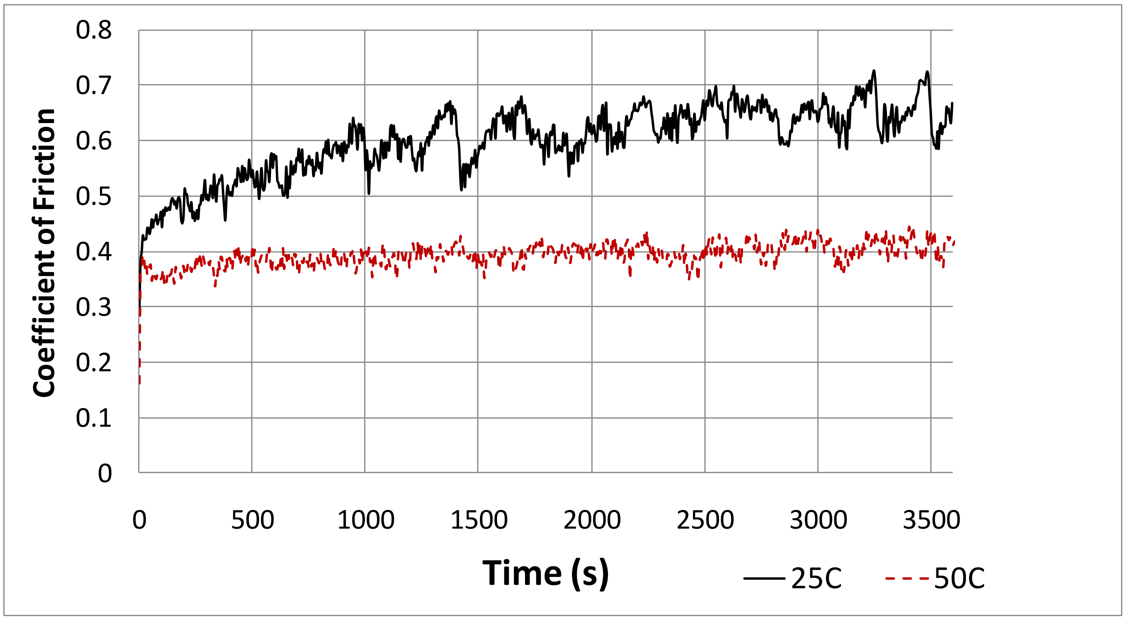

Figure 59 Transient behavior of the coefficient of friction for wear tests of GSG-Al at room temperature and 50°C

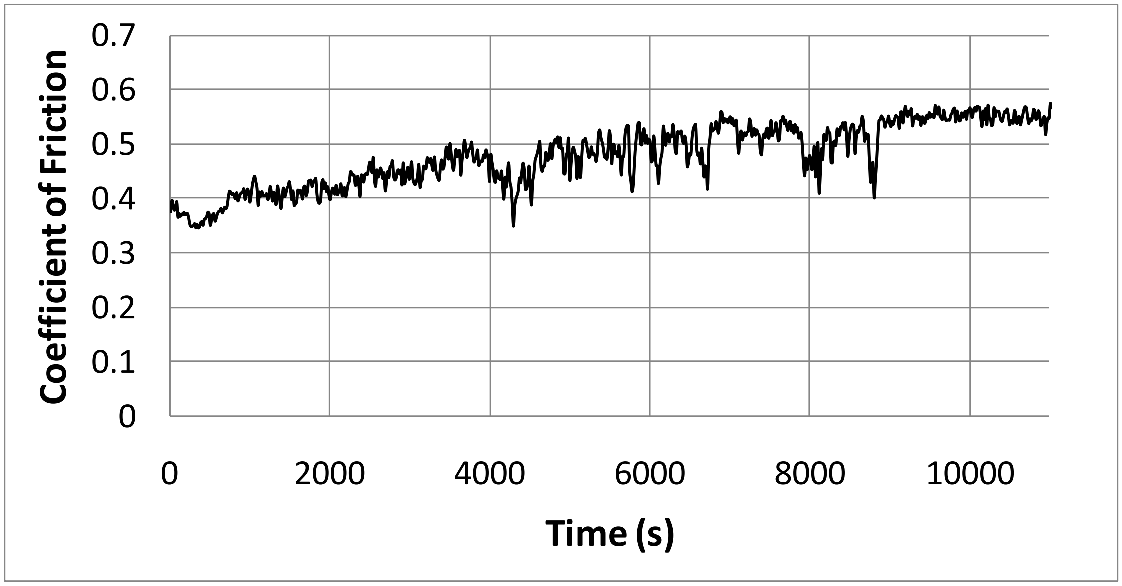

Figure 60 Transient behavior of the coefficient of friction for wear tests
of GSG-Al at 150°C

The effects of temperature were also studied on a sample of Al 6061-T651. Figure 61 and Figure 62 show the worn samples of Al 6061-T651 at 50°C and 150°C respectively.

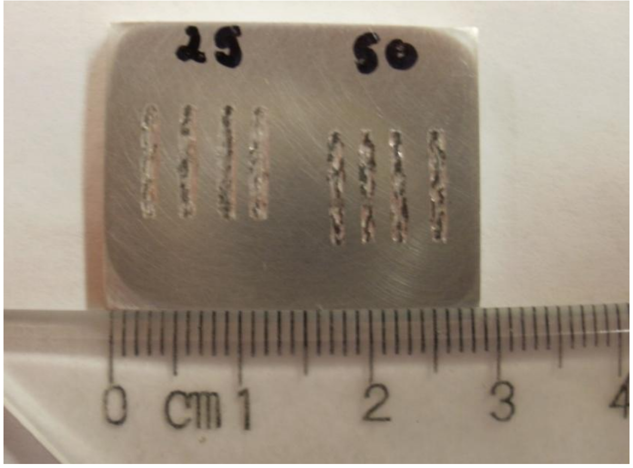

Figure 61 Al 6061-T651 sample worn at a temperature of 25°C and (left) 50°C (right) containing four wear tracks for each temperature

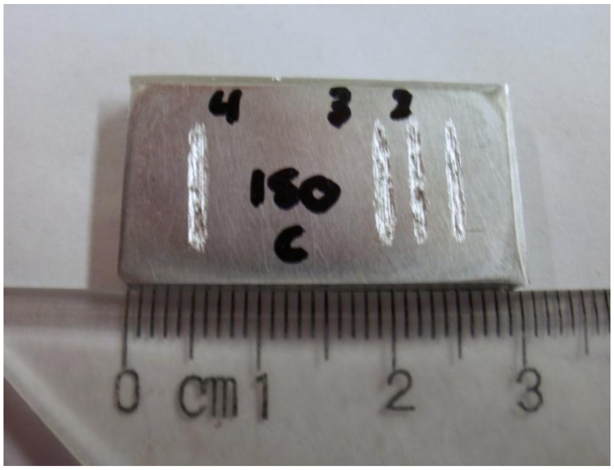

Figure 62 Al 6061-T651 sample worn at a temperature of 150°C containing four wear tracks with only three of them being usable

The last 23 minutes of the tests were used to determine an average of the coefficient of friction. For the 50°C test the average coefficient was calculated to be 0.371 with a standard deviation of 0.024. The 150°C test exhibited the longest running-in period, but exhibited a more stable behavior than the 25°C or 50°C tests beginning at around 1750 seconds and continuing through the end of the test. The last 23 minutes of 150°C plot were averaged. The average coefficient for the 150°C test was calculated to be 0.505 with a standard deviation of 0.031. Figure 63 shows the transient behavior of the elevated temperature tests on the sample. The three plots in the figure are each averaged plots at three different tests at the specified temperature.

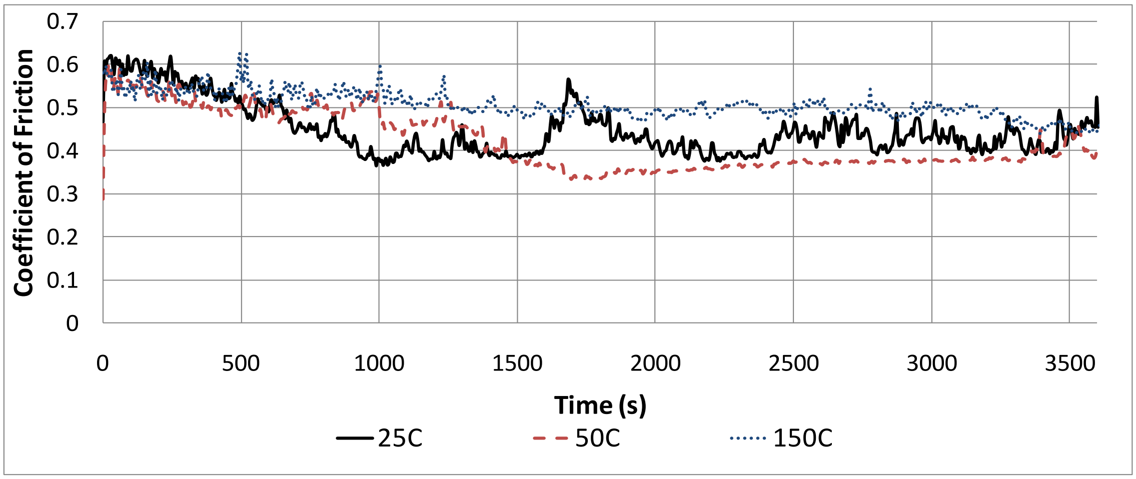

Figure 63 Transient behavior of the coefficient of friction of GSG-Al for the elevated temperatures of 25°C, 50°C, and 150°C for a time of one hour

Figure 64 shows a column chart comparison between the average coefficients of friction at the temperatures of -25°C, 25°C, 50°C, and 150°C.

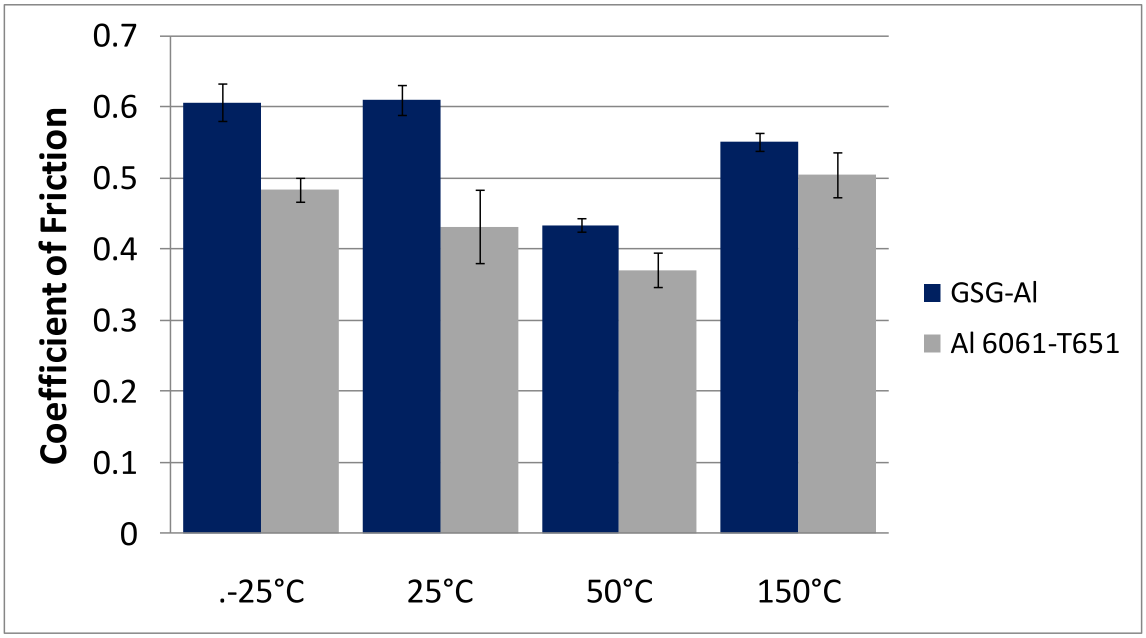

Figure 64 Comparison of the coefficients of friction for both GSG-Al and Al 6061-T651at temperatures of -25°C, 25°C, 50°C, and 150°C

GSG-Al has the highest overall coefficient of friction at all four temperatures. It is apparent from Figure 64 that both GSG-Al and Al 6061-T651 exhibit a reduction in the coefficient of friction from room temperature to 50°C. An interesting result is that the reduction of GSG-Al's coefficient from 50°C to 25°C is greater than that of Al 6061-T651. Both metals show a decrease in the coefficient from 25°C to 50°C and an increase from 50°C to 150°C; however, Al 6061-T651 shows a higher coefficient at 150°C than at room temperature, the opposite can be said for GSG-Al. For GSG-Al the room temperature test and -25°C test are virtually the same, while Al 6061-T651 experiences a decrease in friction between -25°C and room temperature. When the overall stabilities of both materials are compared to one another, GSG-Al tends to have the more stable friction coefficient with time as it has the lowest standard deviations.

4.8.2 Wear

4.8.2.1 Wear Rate

The wear rate was calculated for all temperatures and was calculated the same way. The wear rates of the GSG-Al and Al 6061-T651 were both calculated using an optical profilometer to analyze multiple wear tracks on each sample. Wear studies at -25°C developed smaller wear volumes due to the shorter wear time. The wear rate for GSG-Al at -25°C was determined to be 1.63E-6 mm^3/N-mm with a standard deviation of 5.47E-7 mm^3/N-mm. The wear rate is compared with a known metallic sample. A sample of Al 6061-T651 aluminum was analyzed due to its common usage in structural components and since aluminum is a constituent material of GSG-Al. The wear rate of Al 6061-T651 was found to be much higher than the GSG-Al sample at the lower temperature range with average value of 4.22E-6 mm^3/N-mm and a standard deviation of 5.39E-7 mm^3/N-mm.

The wear tests conducted at 25°C indicated a strong difference from the -25°C tests. From that volume the average wear rate of GSG-Al was determined to be 7.55E-7 mm^3/(N-mm) with a standard deviation of 1.10E-7 mm^3/(N-mm). The wear data for the GSG-Al and Al 6061-T651 tests are shown in Table 4.

Table 4 Average cross sectional area and volume of GSG-Al and Al 6061-T651 wear tracks at room temperature along with their calculated wear rates

Sample	**GSG-Al**	**Al 6061-T651**	**Units**
Temperature	**25**	**25**	°C
Average Area	0.0130	0.0930	(mm^2)
Std. Dev.	0.0019	0.0057	(mm^2)
Wear Track Volume	0.1039	0.7437	(mm^3)
Volume Std. Dev.	0.0152	0.0459	(mm^3)
Wear Rate	7.55E-07	5.40E-06	mm^3/N-mm
Wear Rate Std. Dev.	1.10E-07	3.34E-07	mm^3/N-mm

The average wear rate of Al 6061-T651 is 5.41E-6 mm^3/(N-mm) with a standard deviation of 3.34E-7 mm^3/(N-mm). The wear rate for aluminum at room temperature is much higher than that for GSG-Al at roughly 7 times the wear. This result is significant in that it indicates a greater wear resistance of the GSG-Al and that it shows better promise in wear applications than a commonly used aluminum in industry.

The wear rates of GSG-Al and Al 6061-T651 were conducted at elevated temperatures of 50°C and 150°C. The wear data for GSG-Al at elevated temperatures are shown in Table 5 while the wear data for Al 6061-T651 are shown in Table 6.

Table 5 Wear data for GSG-Al for at temperatures of 25°C, 50°C, and 150°C

Sample	**GSG-Al**			**Units**
Temperature	**25**	**50**	**150**	°C
Average Area	0.0130	0.0079	0.0066	(mm^2)
Std. Dev.	0.0019	0.0006	0.0022	(mm^2)
Wear Track Volume	0.1039	0.0636	0.0525	(mm^3)
Volume Std. Dev.	0.0152	0.0046	0.0174	(mm^3)
Wear Rate	7.55E-07	4.62E-07	3.81E-07	mm^3/N-mm
Wear Rate Std. Dev.	1.10E-07	3.34E-08	1.27E-07	mm^3/N-mm

Table 6 Wear data for Al 6061-T651 for at temperatures of 25°C, 50°C, and 150°C

Sample	**Aluminum 6061 T651**			**Units**
Temp.	**25**	**50**	**150**	°C
Average Area	0.0930	0.0341	0.0424	mm^2
Std. Dev.	0.0057	0.0109	0.0220	mm^2
Wear Track Volume	0.7437	0.2730	0.3393	mm^3
Volume Std. Dev.	0.0459	0.0874	0.1757	mm^3
Wear Rate	5.40E-06	1.98E-06	2.47E-06	mm^3/N-mm
Wear Rate Std. Dev.	8.35E-08	1.59E-07	3.19E-07	mm^3/N-mm

GSG-Al and Al 6061-T651 wear rates at temperatures of -25°C, 25°C, 50°C, and 150°C are shown in Figure 65. The figure shows a great difference between the two materials when it comes to wear.

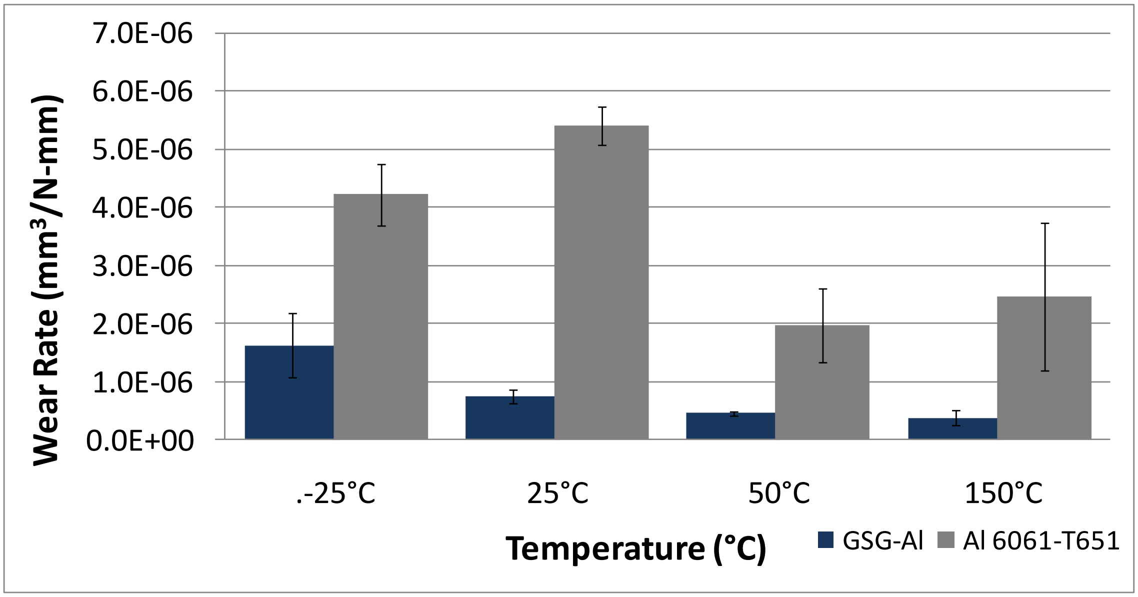

Figure 65 Comparison of the wear rates for GSG-Al and Al 6061-T651 at temperatures of 25°C, 50°C, and 150°C

The wear rates for GSG-Al show a decreasing trend as the temperature increases. The wear rate for Al 6061-T651 shows a differing trend in that it decreases from 25°C to 50°C, but increases again by the time a temperature of 150°C is reached. The room temperature tests showed that the Al 6061-T651 material has a much higher wear rate than GSG-Al, and this is also seen at higher temperatures. On a percentage basis, the Al 6061-T651 showed a greater drop in wear rate during the temperature change from 25°C to 50°C.

4.8.2.2 Wear Debris

The TEM was used in order to gather data on wear debris from GSG-Al and Al 6061-T651 samples. Particular attention was paid to the shape of the materials as well as the size and relative sizes of sample debris. Figure 66 shows the wear particulate for GSG-Al tested at room temperature.

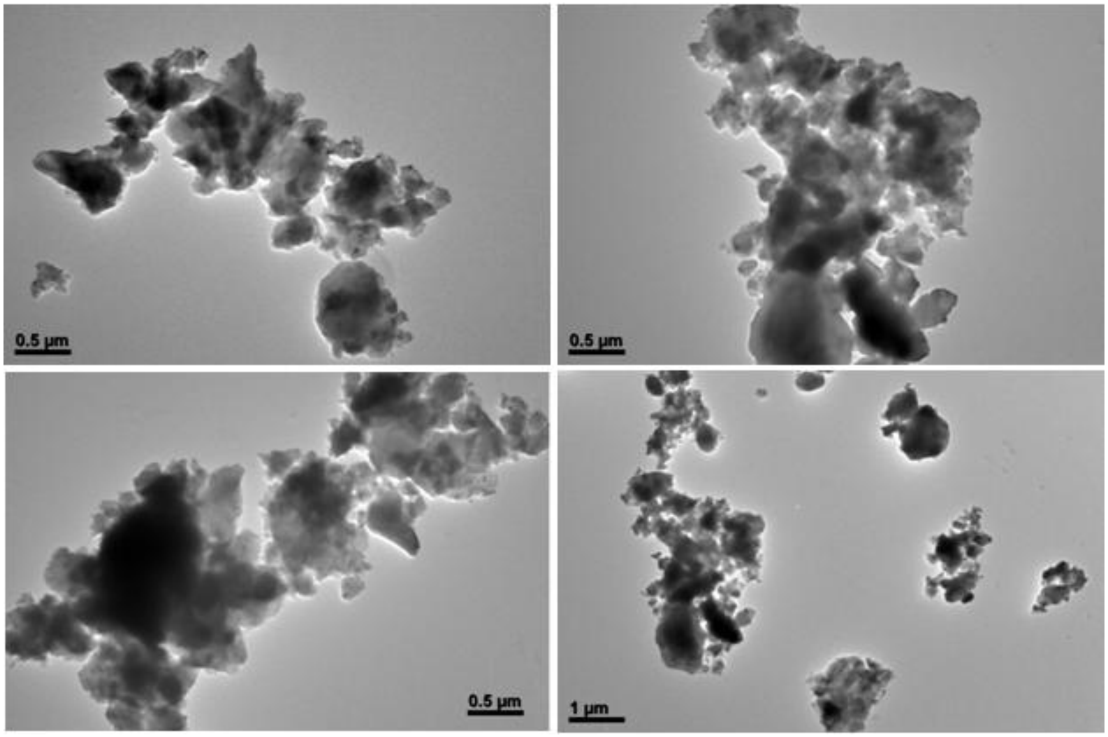

Figure 66 Wear debris viewed under the TEM from a wear test of GSG-Al at room temperature

The particles in the sample do not indicate a constant debris size; however, few particles appear to be greater than 0.5 µm in diameter. The wear debris from the elevated temperature wear test at 50°C were also analyzed under the TEM in order see if temperature affects the size and shape of the wear debris. Figure 67 shows the wear debris at this elevated temperature.

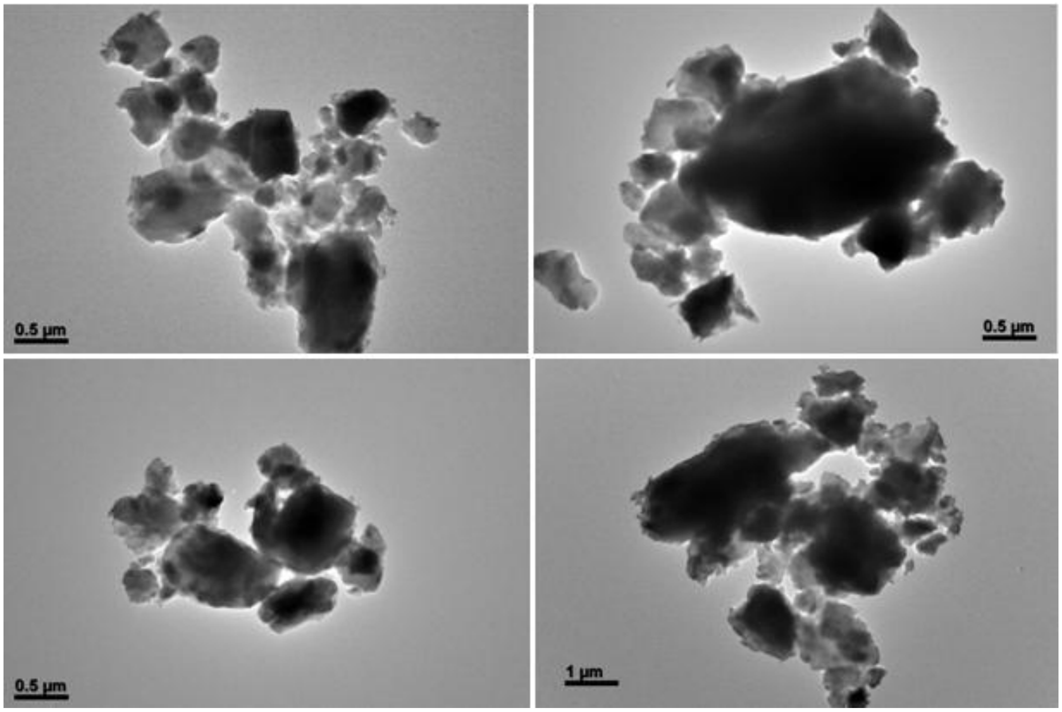

Figure 67 Wear debris of GSG-Al from the wear tests at 50°C

The particles at this temperature appear to be greater in size relative to the room temperature wear debris and most particles are greater than 0.5 µm in diameter and several particles exceed 1-2 µm. The highest temperature at which elevated temperature wear tests were conducted on GSG-Al was 150°C. Figure 68 shows the magnified wear debris from the 150°C test.

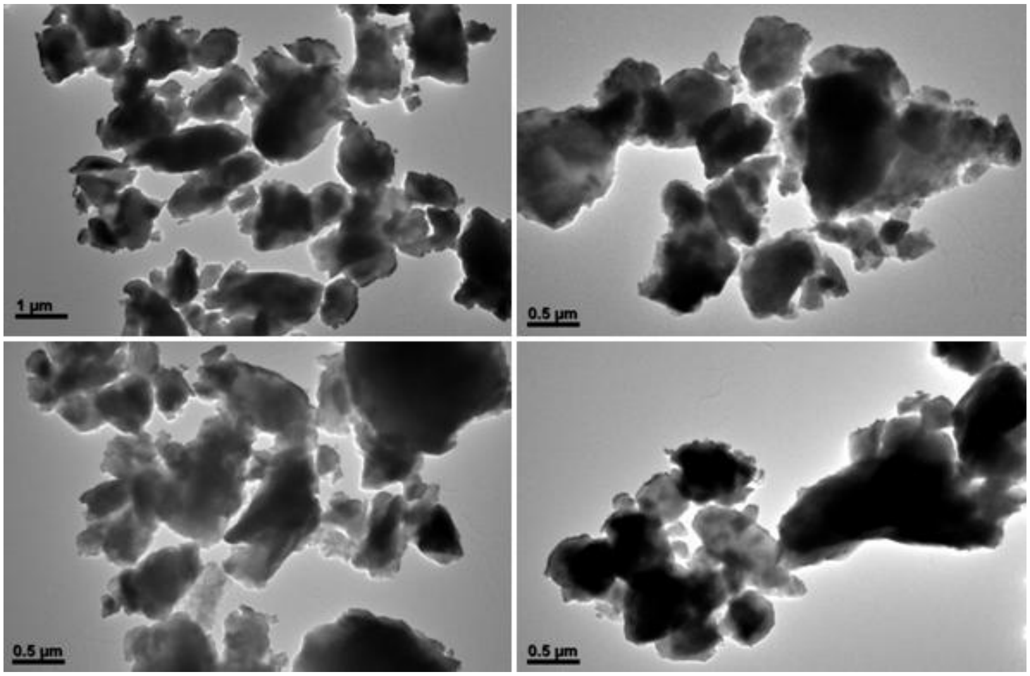

Figure 68 Wear debris viewed under the TEM from a wear test of GSG-Al at 150°C

The particles at 150°C all have diameters greater than 0.5 µm with even more particles exceeding 1 µm. The particulate growth shows a trend of increasing particulate size with temperature.

In order to better understand the wear debris of GSG-Al, the samples were compared to wear debris of Al 6061-T651 when the sample was tested at room temperature. Figure 69 displays the wear debris from Al 6061-T651.

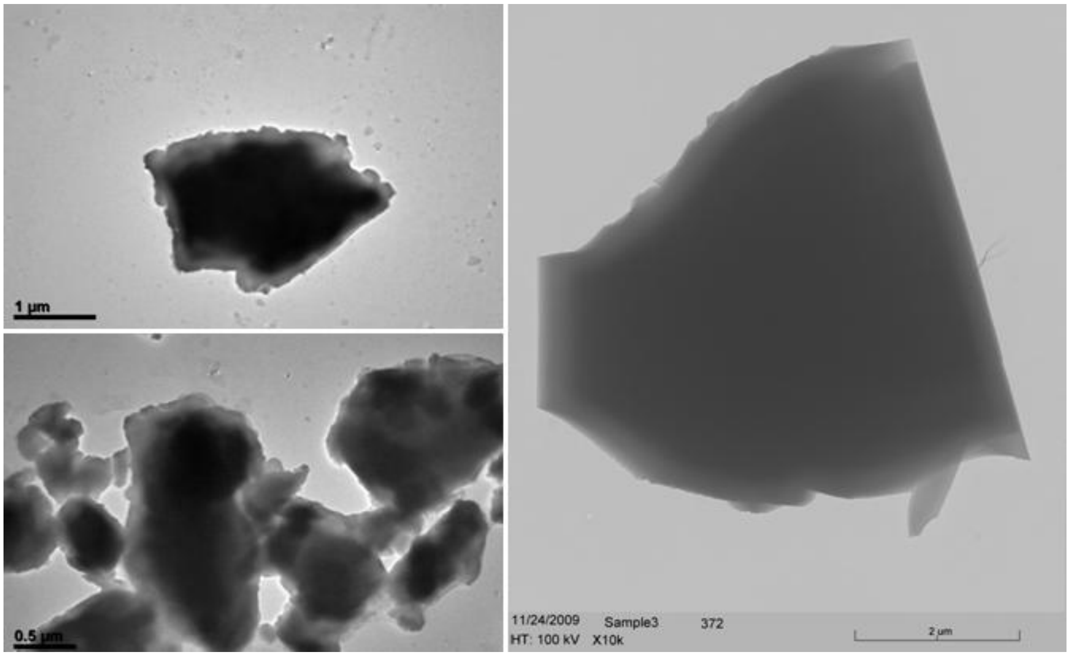

Figure 69 Wear debris viewed under the TEM from a wear test of Al 6061-T651 at room temperature

Aluminum debris consists of both rounded and sharp particles. Some of the sharp particles are very large and flake-like in appearance. The debris from the room temperature test for Al 6061-T651 is greater than or equal in size to the GSG-Al particulate at 150°C.

EDS studies were conducted on GSG-Al wear debris samples that were formed from wear tests conducted at 25°C, 50°C, and150°C. This test was performed in order to see what effect temperature had on oxidation and wear particle composition. Figure 70 shows the EDS results and displays them according to recorded weight percentages of elements detected.

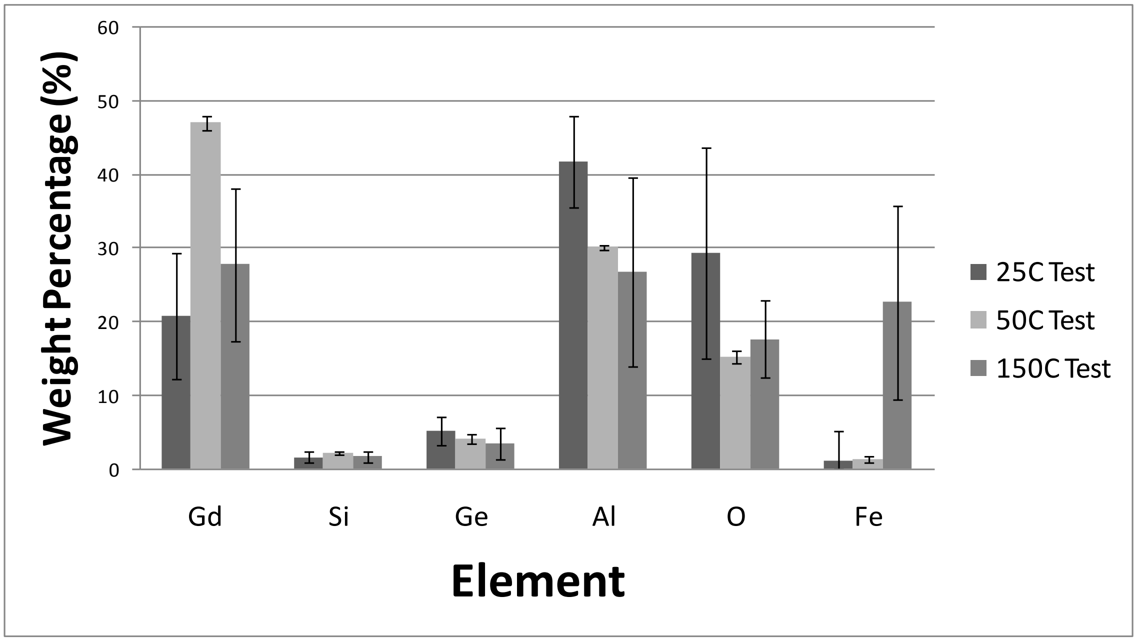

Figure 70 Weight percentage of the different elements contained within the GSG-Al wear test debris at different test temperatures

The elements of Gd, Al, and O show the greatest weight percentages in the sample at all temperatures, while Ge and Si appear to show small weight percentages as well as relatively constant percentages as the temperature increased. Iron showed an unexpected jump in weight percentage in the 150°C wear debris. No evidence is noticeable in the EDS tests that would indicate an oxidation rate trend.

CHAPTER V

DISCUSSIONS

This chapter discusses the microstructures, properties, and tribological performance of the GSG-Al composite. The structural properties of the GSG-Al are compared to those of its constituent compounds such as GSG, Al, and GdAlGe. It is followed by an analysis of the physical and mechanical properties of the same and compared with related metal alloy, Al 6061-T651. Lastly, this chapter discusses the friction and wear performance of materials developed in research.

5.1 Microstructures

GSG-Al is composed of three known compound configurations: aluminum, GSG, and GdAlGe. The three types of materials have different crystalline configurations. Aluminum exhibits a face centered cubic crystalline structure. The GSG exhibits a monoclinic crystal structure when in its paramagnetic state above the Curie temperature and an orthorhombic crystal structure when in its ferromagnetic state below the Curie temperature. [49] The ternary compound GdAlGe possesses an α-ThSi-type tetragonal crystal structure at high temperature and a YAlGe-type orthorhombic structure at low temperatures. [103]

The structure of the GSG-Al composite is far more structurally stable than the GSG itself. While the original GSG began to break apart into particulate within a few weeks of formation, as shown in Figure 71 and Figure 72 below, the GSG-Al sample has remained in the same shape with no signs of cracking. The GSG sample was susceptible to magnetostriction effects due to thermal and magnetic variances. Magnetostriction due to the realignment of magnetic moments and phase transformation causes the material to fatigue and crack. [87] Therefore, a composite is needed to eliminate such an effect. A sample of GSG is shown in Figure 71 prior to disintegration due to magnetostriction, while Figure 72 shows GSG in powder form after the disintegration.

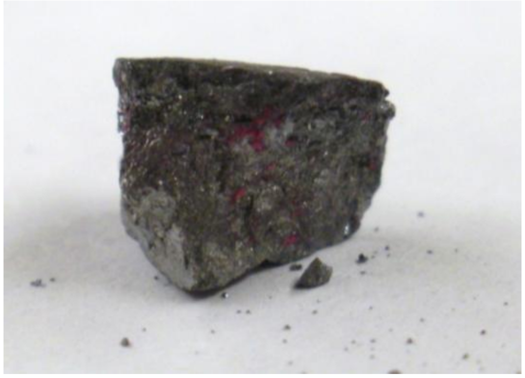

Figure 71 Specimen of GSG prior to onset of effects due to magnetostriction and phase change

Figure 72 Specimen of GSG after it was affected by many cycles of magnetostriction and phase changes

GSG-Al samples have been tested at both high and low temperature extremes 20 times in order to study the thermal properties of the material. The GSG-Al has shown no signs of fatigue or cracking. According to the Figure 47 the linear thermal expansion coefficient of the composite is 2.35E-5/K and Al 6061-T651 has a expansion constant of 2.3E-5/K, but at lower temperatures and in Figure 49 GSG-Al has a large expansion jump to 7.4E-3/K indicating a phase change and high strain.

The resistance of this material to fatigue compared to GSG can be explained in three different ways. Aluminum has a Young's modulus of 69 GPa compared to 200 GPa for steel [97]. This low modulus allows flexibility within the composite. The use of aluminum might have a disadvantage since it has no endurance limit. It has been known that the aluminum can fatigue far easier than steel. [97] Through the use of GSG in the composite, the fatigue effects seem limited.

Another reason why the composite is resistant to cracking is because of the formation of pores generated during the sintering process. Pores provide room for certain phases in the material to expand. If the phases were expanding into a dense composite, the cracking could be significantly increased. Pores can also act as crack inhibitors due to their shape. As a crack propagates through a material its tips have high stress concentration causing cracks to propagate further. If a crack tip intercepts a pore, the tip becomes a pore and the stress concentration factor is significantly reduced, stopping crack propagation. [104]

A final possible reason to why the composite did not crack is due its microstructure. This material is not GSG and it is not aluminum; rather it is a new material with new properties. As will be discussed later, the properties of GSG-Al are significantly different from its constituent metals, and a possible reason for the limit to crack formation may lie in the development of a unique thermal expansion property. The crystal sturctures of the material were analyzed using the XRD. As shown in Figure 40 , Figure 41, and Figure 42, XRD analysis revealed that there are three known compounds that existed in the GSG-Al sample: GSG, Al, and GdAlGe. As indicated in the Figure 42, there are several clean and distinguished peaks of GSG and Al. The third compound, GdAlGe, was found. This means the strong bonding betweeing GSG and Al. Interestingingly, materials similar to GdAlGe are known to exhibit strong magnetizations with relatively high Curie temperatures. [91] Prior research has been conducted on alloys containing Al, Gd, and Ge that have a form of $Gd(Al_{1-x}Ge_x)_2$ and some results have been described in Chapter 1. In the present research, the formation of GdAlGe during processing of GSG-Al means the strong bonding of the GSG and Al matrix. The properties of this compound will be studied in the future.

5.2 Surface Roughness Analysis

Section 4.3 listed the roughness results. The average surface roughness value of 0.481 μm indicates a level of polishing designated as an N5 level. The N5 level is range of roughness values designated in ISO 1302 that indicate a ground finish in the GSG-Al sample. The level is one of 12 (N1 to N12) with N1 being the finest of finishing. [105] The porous nature of the sintered GSG-Al and the multiple phases that make up the sample cause this level of surface roughness.

Studying the Abbott-Firestone curve, as shown in Figure 43, a general shape is noticed. It displays the type of surface profile on the GSG-Al. The curve is a graphical representation of the bearing ratio which determines the shape of the peaks within the sample length. The standard deviation, shown in Figure 43, was based on ten tests. The shape of the curve indicates that the surface of GSG-Al has shorter and rounder peaks rather than tall and thin peaks. This was to be expected due to the large amount of polishing involved in reaching 0.48 µm. Rounder peaks mean the sharp tips of the peaks prior to polishing had been ground down. The surface roughness is important because a smoother surface would work better in wear applications. The surface roughness, though, is really only influential in the initial stages of wear, i.e., the running in period.

5.3 Phase Distribution

The phase analysis was conducted using microscopic tests combined with picture analysis software and the results are shown in section 4.4. Results revealed that the samples consist of roughly 2/3 aluminum and 1/3 GSG on a cross sectional area basis. The designation of “aluminum” and “GSG” grains for GSG-Al does not mean that aluminum or GSG exists purely in those phases; instead those phases are merely mostly aluminum or mostly GSG. The GSG material has densities in the range of 5.7 g/mL, while aluminum has that of 2.7 g/mL. Since the two materials are combined in equal mass amounts to form GSG-Al, the percentage of GSG in the sample is 32.14% in volume ratio, while that of aluminum is 67.86%. These values are close to the values for the area ratios and thus add corroboration to the data collected.

It is important to understand the ratio of aluminum to GSG because the important properties of both compounds and their concentrations will determine the properties of the composite. GSG, prior to the addition of aluminum, disintegrated with time and had no structural stability. The addition of aluminum has corrected this problem and the material can now hold its form.

5.4 Hardness Test Analysis

This section discusses the two different forms of hardness tests performed on GSG-Al: Rockwell and Vicker's microhardness. GSG-Al and Al 6061-T651 were both tested in the Rockwell scale while on GSG-Al was tested in the Vicker's. This section seeks to analyze the relative hardness of these materials and determine whether a structural application is feasible.

5.4.1 Rockwell Hardness Test Analysis

As shown in Figure 45, the Rockwell hardness tests performed on GSG-Al yielded an average superficial hardness of 34 HR30-T. The data range for the sample varied greatly. The hardness indicates that GSG-Al shares a similar value to copper and copper nickel. Both materials are used for heat transfer and electric applications. [106] Sintering processes along with the multiple phases in GSG-Al added to the material's ductility. Limiting the effects of the porosity would be the first step in converting this material to one that could be used in structural applications. If the application for the composite requires a more ductile mechanical property, then GSG-Al would be a good choice. In industry, there are many processes used to harden and strengthen aluminum alloys, specifically precipitation (age) hardening and quenching. These processes may be useful in the future to modify the structure of the GSG-Al. [106]

For comparison, Al 6061-T651 was tested for its superficial Rockwell hardness. Al 6061-T651 yielded a more consistent average hardness value of 56 HR30-T which can be approximated as 59 HRB. This value is consistent with published data of Al 6061-T651 by the International Alloy Designation System (IADS). Al 6061-T651 is harder than GSG-Al and has been used in several structural applications such as aircraft fittings, valves, and bicycle frames. [93] Al 6061-T651 is made by blending aluminum with small percentages of magnesium and silicon. This blending aids in the machinability of the alloy which makes ideal for use in many factory made parts. This material has also been precipitation hardened which increases its yield strength and thus its suitability in structural applications. [106]

5.4.2 Vickers Micro-Indentation Hardness Analysis

The Vicker’s testing of GSG-Al was primarily used to identify the relative hardness of the phases that make up GSG-Al and results have been listed in Figure 46. The two noticeable phases of GSG and aluminum phases significantly differ in their Vicker’s hardness readings. The GSG concentrated phase is clearly harder than the aluminum region. However, when Vicker’s tests were done at the centers of the GSG phases, the hardness increased greatly from those reading taken at its fringes. This indicates that the small amount of aluminum in the indentation area can affect the data.

The aluminum used to create GSG-Al was in the form of powder prior to compression and sintering of the sample. This is unlike the GSG which existed in both powder and bulk form. The bulk had cohesion prior to the sintering process and did not become as porous as in the aluminum regions. Porous regions of aluminum were thus seen as softer phases, while the bulk GSG was more cohesive and harder. Due to the randomness of the testing, regions of mixed phases of GSG and aluminum were also evaluated. Such data is shown in Figure 46. Phase boundaries are known for being weaker or softer than the bulk of the phase, as indeed shown here.

5.5 Thermal Expansion

This section analyzes the thermal expansion of the GSG-Al composite in the temperature regions of 25°C to 185°C and -18°C to 8°C. The separation of the two regions is important due to GSG having a phase change at -6°C when a magnetic field is not applied.

5.5.1 High Temperature Analysis

As shown in Figure 47, the coefficient of linear thermal expansion of GSG-Al for temperatures between 25°C and 185°C was found to be that of aluminum. As noted, the GSG-Al has 50% aluminum by mass. In comparison with steel, aluminum and GSG-Al have considerably higher values; this is important to realize considering many automotive components are made of steel. Thermal expansion above the Curie temperature for GSG is important to analyze since GSG-Al would be faster in cooling than in warming. This is important for applications in an IC engine. Also, the thermal expansion experimentation aids in determining temperatures effect on phase changes within the material and if they exist at all.

Noticing the effects of expansion at higher temperatures is crucial since the Curie temperature may or may not cause significant expansion or contraction in the newly formed GSG-Al composite. The expansion of GSG-Al according to Figure 47 forms a linear trend at high temperatures meaning that the Curie temperature has not been experienced. The magnetocaloric effect on expansion does not affect GSG unless the sample is around the temperature of -6°C (without a supplied magnetic field). [48] The fact that another magnetic material, GdAlGe, was formed means that this Curie temperature could have been shifted or suppressed. As a matter of fact, it has been reported that when changing the elemental of Si to Ge the Curie temperature shifts. [56] This means that, due to the magnetocaloric effect or phase changes, magnetostriction and expansion of the material cannot be seen in the high temperature range.

5.5.2 Low Temperature Analysis

Results are shown in Figure 48 of the low temperature thermal expansion of GSG-Al. The low temperature tests provided interesting results. GSG is known to expand rapidly due to a phase change from an orthorhombic crystal structure to monoclinic when the Curie temperature of -6°C is reached. [48] GSG's Curie temperature is dependent upon the magnetic field that is applied to the material. If no magnetic field is applied, GSG has a Curie temperature of -6°C. At the Curie temperature, GSG experiences a large amount of strain in the range of only a couple of degrees. One study found that the sample jumped 8250 ppm strain between -6°C and -8°C. [48] This strain, even though large, is not as large as the amount of strain that the GSG-Al went through. GSG-Al experienced a large jump in the expansion of the material as a function of temperature. While the coefficient of thermal expansion for GSG-Al at temperatures above 25°C was 2.35E-5/°C, the expansion coefficient for the lower temperature tests was 7.4E-3/°C. The expansion coefficient increased by 2 orders of magnitude.

The large strain could be caused by the nature of this new combination of materials, but the explanation for this expansion lies in a phase change within the material. From the magnetic tests, as shown in Figure 52, it can be seen that the sample does not experience a magnetic transition at -6°C or at room temperature. As known, aluminum does not experience a phase change within this temperature range, but GSG does. Studies of $Gd(Al_{1-x}M_x)_2$ alloys have shown that it does experience changes within the crystal lattice, but in different temperature ranges. [91] It is possible, however, that the existence of the $Gd(Al_{1-x}M_x)_2$ alloy in this composite and its interaction with the other phases may have changed its properties. For GSG and GdAlGe, their phase changes appear to control magnetic properties in this composite. This giant strain effect in a ductile material can be beneficial as a method to help cracks self-heal and could reduce the spread of cracks in materials if the material is brought within this low temperature range.

5.6 Wear and Friction Analysis

This section discusses the wear and friction results in Chapter 4. Wear tests were performed in order to see if GSG-Al sample would function well in the harsh environment of an automobile engine which experiences significant wear. Due to IC engines constantly changing temperature, understanding the material's wear and friction properties as a function of temperature was desired. This section discusses the effect of temperature on the friction and wear of GSG-Al and Al 6061-T651, the TEM and EDS wear debris analysis, and the wear mechanisms that were proposed.

5.6.1 Friction Analysis

As shown in Figure 64, the coefficient of friction for GSG-Al at -25°C was close to the room temperature value. The high friction value is most likely related to the increased roughness from increased adhesive wear. The build-up of the GSG-Al material suggests that abrasive was sticking at times to the sample surface. This increased contact area as well as surface roughness would increase the coefficient of friction. The increasing surface area with time allowed for more direct contact between the abrasive and the GSG-Al surface.

According to Figure 64, the Al 6061-T651 sample showed an increase in the coefficient of friction from room temperature. As with the GSG-Al sample, the adhesive wear also increased from room temperature and the same situation that GSG-Al encountered, Al 6061-T651 encountered as well. As shown in Figure 64, the Al 6061-T651 had a far more jagged wear scar than the room temperature scars. When combining the jaggedness of the abrasive with the adhesive forces, it can be seen that the force required to move the abrasive is quite high.

From Figure 59 it can be seen that the coefficient of friction steadily increased throughout the one hour of testing until the coefficient stabilized. The GSG-Al surface at room temperature was recently polished which means that the oxide layer was minimal. Comparing Al with Al_2O_3, the Al is softer and easier to be deformed by the slider. The contact area in such will be increased and the friction is expected to increase. The Al_2O_3 is harder and vice versa. This phenomenon is further proven at high temperatures where the oxidation or the tribo-oxidation is more pronounced. As such the friction is reduced. [107] Opposing this deduction is the amount of moisture present in the environment during the tests. As temperature increases, the moisture tends to decrease. Moisture is often detrimental to the abrasive wear of the material; however, it can aid in lowering the coefficient of friction. [102]

Some materials exhibit high friction coefficients due to hardness or surface properties. Al 6061-T651 experienced a coefficient of friction of around 0.4 compared to that of the GSG-Al of around 0.6 as shown in Figure 64. From the hardness tests it was determined that the Al 6061-T651 was harder than GSG-Al. Studies have found that, in general, harder materials do have lower coefficients of friction. This is due mostly to the plastic deformation that exists between the abrasive and the sample surface as just discussed and also found in the reference. [108] The different phases that exist on the surface of GSG-Al along with its porosity may also be a contributing factor. Porosity generally works similar as the surface roughness. [109] Rather than having a smooth surface, the porous nature makes a rougher surface and this roughness continues down into the bulk of the material.

A trait that both GSG-Al and Al 6061-T651 share is that there is a reduction in friction from room temperature to 50°C, but a rise in friction from 50°C to 150°C. This trend can be seen in Figure 64. This effect was interesting in itself, but the samples also had interesting wear characteristics as the temperature changed. According to Figure 65, the GSG-Al samples tended to slowly decrease in wear rate as the temperature increased, but Al 6061-T651 tended to fall and then rise much as it did in the friction tests.

As temperature increases, materials that do not undergo a phase change tend to soften. Softening of the material can lead to a wear mechanism known as plowing. [110] Plowing is where the abrasive material begins to have the softer material build up in front of it as it is moved. This causes an increase in the friction because the motion of the abrasive is opposed by the build-up of the soft material. Even outside of the plowing effect, softer materials deform more and can thus increase their contact area with the abrasive material. This extra contact leads to increased friction and wear. [110]

Atmosphere and environment have profound effects on wear. Humidity and atmospheric gases play a prominent role in the analysis of wear and friction. Many materials tend to be more susceptible to abrasive wear as the moisture in the atmosphere increases, but there are exceptions. [111] Moisture can weaken parts of the abrasive or create new cutting edges to abrade the material. It can also undergo interfacial reactions with the abraded material. [111] The increase in temperature reduces the wear rate and possibly increases friction, but friction and wear are not solely dependent on moisture.

This is because an increase in temperature lessens the chance of moisture from affecting the surface of the material, whether it is evaporation or the distance from dew point.

Another temperature related effect is the oxidation rate. Oxidation rate is dependent on temperature and the rate increases greatly with the same. [112] For this experiment, aluminum oxide (Al_2O_3) is the main oxide to form on Al 6061-T651 while GSG-Al forms several due to the presence of Gd, Ge, and Al. The aluminum oxide tends to form a thin layer on aluminum alloys and builds to a thickness of only 0.02 μm. [112] This oxide is tougher and harder than the bulk of aluminum and thus alters the coefficient of friction and wear. [112] The presence of the oxides was determined during the EDS analysis of the wear debris. At all temperatures the oxygen content in the wear debris stands out as the highest element concentration by molecular weight. It was not determined from EDS whether the oxidation of the materials increases as temperature increases, however it is generally held that this is the case. [43] Aluminum oxide is harder than aluminum itself and is useful both in its protection from further oxidation of the aluminum bulk and its strengthening of the aluminum surface. Harder materials tend to have lower wear rates. [113] So if the oxidation increase was alone in its effects, one would expect a reduction in friction and abrasive wear with increased temperature. As stated, the oxide for aluminum is thin and can be worn and reformed at the same time. The temperature accelerates oxide production and forms as the abrasive wears into the bulk.

GSG-Al and Al 6061-T651 do not show a constant trend upwards or downwards in friction and wear; rather they are more dynamic. For GSG-Al and Al 6061-T651, the friction decreases from room temperature to 50°C, but it then increased again once 150°C was reached. From the effects analyzed in GSG-Al, the oxidation rate effects outweigh the effects of friction increases due to adhesion and softening of the bulk in the temperature transition from 25°C to 50°C. When a temperature of 150°C was reached, the adhesive and softening effects outweigh the effects of the oxidation rate. In the Al 6061-T651 samples, the same traits apply except that surface fatigue becomes a determining factor.

5.6.2 Wear Rate Analysis

5.6.2.1 Wear Modes

This section discusses the wear modes within GSG-Al and Al 6061-T651 samples worn at temperatures ranging from -25°C to 150°C. The microscopic images of the wear tracks and abrasive steel balls are observed and analyzed for signs of abrasive wear, adhesive wear, or surface fatigue. The relative severity of these wear modes are also analyzed.

Samples of GSG-Al and Al 6061-T651 were studied for wear and friction properties at low temperatures. In order to analyze the wear mechanisms at these low temperatures digital microscopic images were taken of the wear tracks and abrasive balls. Figure 73 shows a wear track of a GSG-Al sample worn at -25°C.

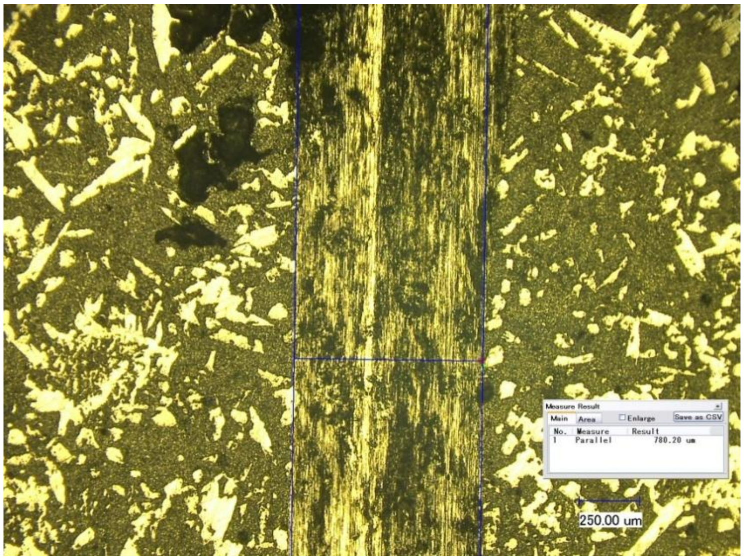

Figure 73 Magnified image (100X) of a wear track on sample of GSG-Al that was worn at a temperature of -25°C for 30 minutes

The wear tracks made at low temperatures appear to show the same types of wear mechanisms as the tracks made at higher temperatures. Abrasive wear is visible in the linear scratches made in the GSG-Al wear tracks. Debris can be seen in the wear track as dark patches where the material was not pushed to the ends of the wear tracks. The wear scars of balls were analyzed under an optical microscope. Figure 74 and Figure 75 show the abrasive steel balls used in the wear of the GSG-Al.

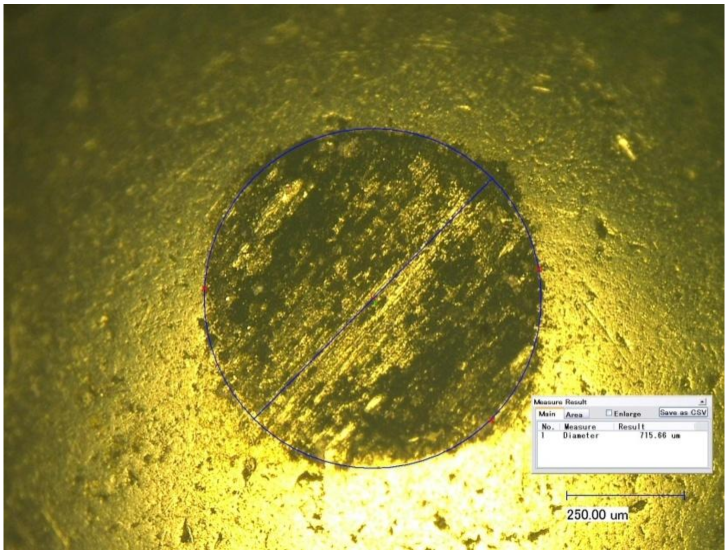

No.	Measure	Result
1	Diameter	715.66 um

Figure 74 Magnified image (200X) of the steel abrasive used to wear a sample of GSG-Al at a temperature of -25°C for 30 minutes

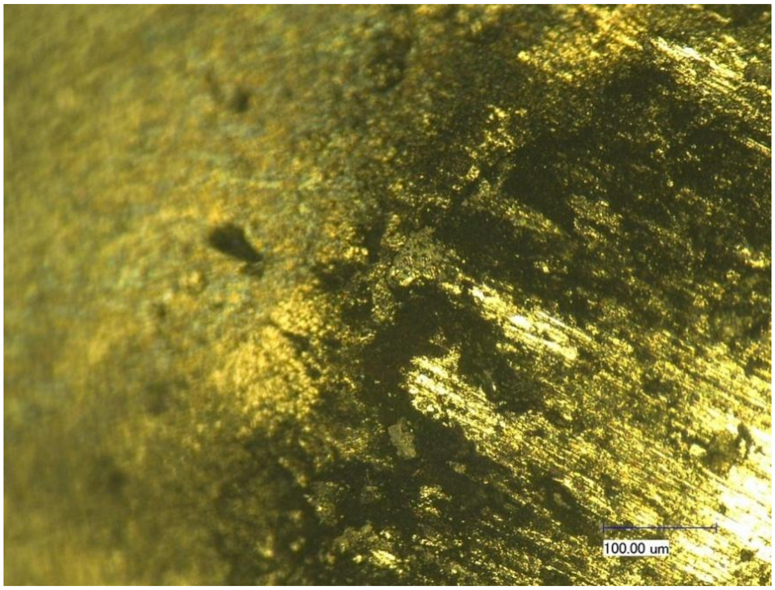

Figure 75 Magnified image (450X) of the steel abrasive used to wear a sample of GSG-Al at a temperature of -25°C with signs of adhesive wear

Figure 74 appears to resemble the abrasive ball used in the other wear tests of GSG-Al with the darker areas of the image representing adhered particles of GSG-Al. Figure 75 shows that the adhesion of the GSG-Al to the steel has increased greatly to form solid mounds of material rather than particulate. This increase in adhesive wear seems contrary to the higher temperature results found when wear was initiated with increased temperatures. From the results the wear mechanism of GSG-Al is primarily abrasive at all temperatures, but interestingly adhesive wear increased from the room temperature tests. The moisture involved in the test could have contributed to the adhesion. Low temperatures often make a material brittle, even though the samples showed no signs of cracking or fatigue, the particulate amount increased due to the wear rate more than doubling from the rate at room temperature. More particulate was available to adhere to the abrasive.

Surface fatigue is not present in GSG-Al samples. It was thought that perhaps through the decrease of temperature, the material may have become very brittle and thus more likely to suffer from fatigue. As the results show, however, temperatures of -25°C and above do not seem to be vulnerable to this form of wear. The thermal expansion of the GSG-Al described in section 4.6.2 occurred within the temperature region that this wear test was performed at. It is likely that the compression of the GSG-Al as the temperature decreased caused any cracks that may have formed to heal themselves. Other reasonable, additional conclusions lie in the porous nature of the sintered material and its limiting effect to crack propagation that extends along a large temperature range.

For comparison with the GSG-Al sample, Al 6061-T651 was worn in the same method. Figure 76 and Figure 77 show wear tracks made in a sample of Al 6061-T651 at a temperature of -25°C.

Figure 76 Magnified image (100X) of a wear track made in a sample of Al 6061-T651 at a temperature of -25°C for 30 minutes

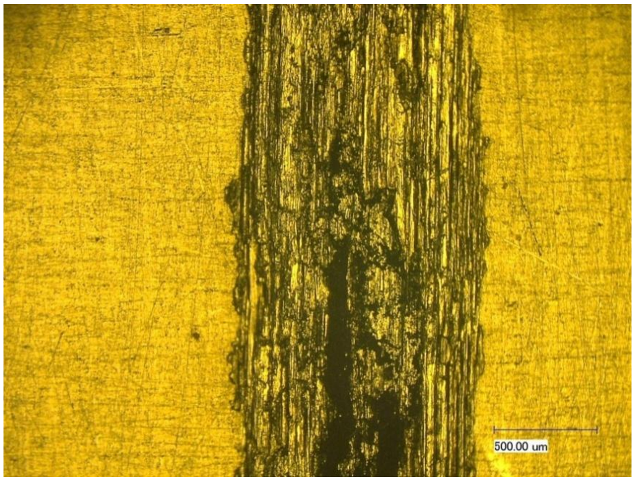

Figure 77 Magnified image (100X) of a wear track made in a sample of Al 6061-T651 at a temperature of -25°C for 30 minutes

The wear tracks in Al 6061-T651 were considerably different in form from the GSG-Al sample and closer in form to the wear tracks formed when at room temperature. Abrasive wear is visible in the linear scratches in the wear track, but it appears to be less significant than it was at room temperature and is being superseded by surface fatigue. The aluminum yielded a special form of surface fatigue known as flaking failure due to the formation of flat flake-like wear particulate from surface spalling and delamination. [41,43,102,114] Spalling is initiated through fatigue and occurs when cracks begin to form beneath the surface of the material and parallel to the wear track. [114] The cracks then begin to propagate around in different directions and they, with the aid of adhesive wear, begin to cause flakes to form and be removed from the track. Surface fatigue appears as it did at the room temperature tests; however, this fatigue is more substantial. Unlike the GSG-Al sample, the low temperature environment has caused embrittlement and further exacerbated the fatigue in the aluminum.

Adhesive wear is present in the Al 6061-T651 sample as it has been present at all temperatures under study. Figure 78 shows the abrasive ball used to wear the Al 6061-T651 and has aluminum adhered to its surface.

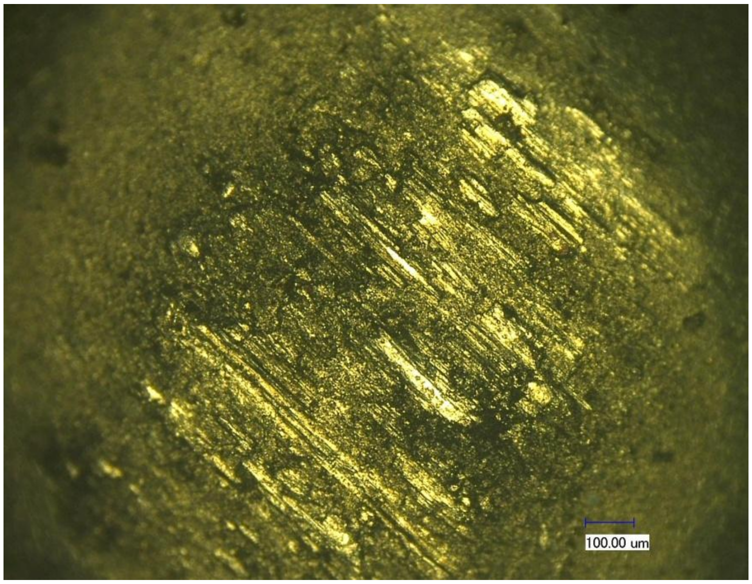

Figure 78 Magnified image (200X) of an abrasive ball used to wear a sample of Al 6061-T651 at temperature of -25°C with traces of adhesive wear present

The adhesive wear at -25°C appears to have increased from the room temperature tests. Due to the increase in surface fatigue, more delamination of the aluminum occurs. When the delaminated particles become loose, they can either be pushed to the ends of the wear track or adhere to abrasive ball. Since the low temperature resulted in the increase in delamination, it provides a higher likelihood of adhesion between the flakes and the steel. Moisture and frost on the surface of the sample also could have added to this adhesion. The wear tests at -25°C indicate that GSG-Al has good wear resistance when compared to Al 6061-T651. The reason for the differences in wear rates lies in the aluminum alloy's susceptibility to abrasive wear, adhesive wear, and surface fatigue. GSG-Al was not affected by surface fatigue and thus performed better.

The wear tracks created during the wear tests with the tribometer at 25°C are shown in Figure 79. The image is an optical microscope digital photo at 50X magnification. Once the test time had elapsed, the wear tracks were approximately 0.871 mm in width, 8 mm in length (neglecting semicircular ends), and 25 µm in average maximum depth.

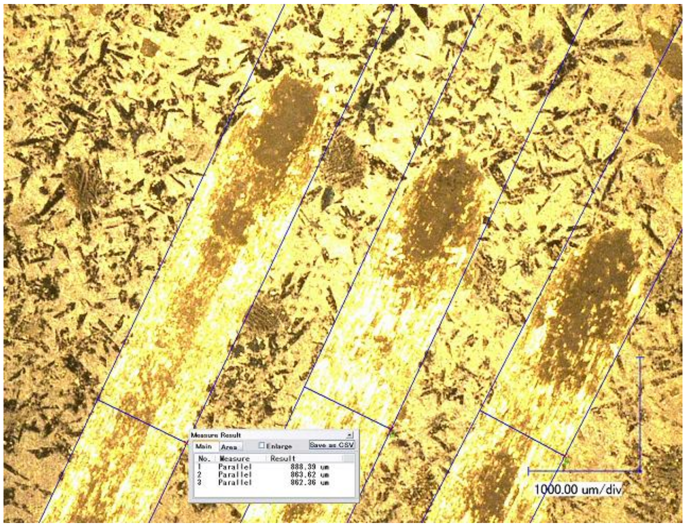

No.	Measure	Result
1	Parallel	888.39 um
2	Parallel	863.62 um
3	Parallel	862.36 um

Figure 79 Magnified image (50X) of three wear tracks made into a sample of GSG-Al at 25°C

The figure shows the three wear tracks that were taken in order to get an average of the wear properties. The mechanism of wear appears to be mostly abrasive wear which can be seen in the linear cutting pattern along the length of the wear track shown in Figure 80 magnified 500X.

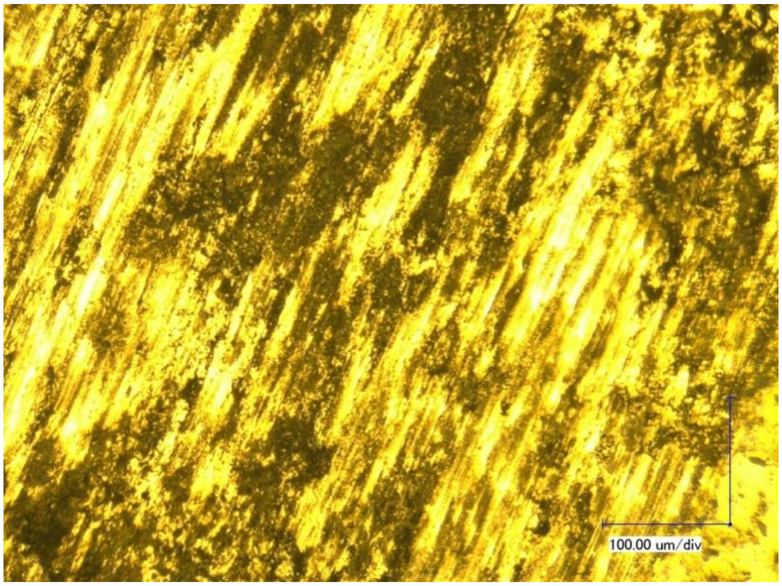

Figure 80 Magnified image (500X) of a wear track made into a sample of GSG-Al at 25°C that displays abrasive wear

The darker areas in the image of Figure 80 are spots where wear debris settled and collected. Adhesive wear does appear to be present when the ball bearing abrasive is viewed under the microscope (magnified 200X) in Figure 81. The darker material on the steel ball bearing is the wear debris. More material was adhered to the ball during and just after the test. The adhesive wear of GSG-Al is very limited at room temperature and is overshadowed by abrasive wear. As was determined in the wear debris analysis in section 4.8.2.2, the wear debris was small and did not adhere to itself as well at room temperature. The particulate was also pushed out of the wear track and deposited at the track ends in large powder clumps.

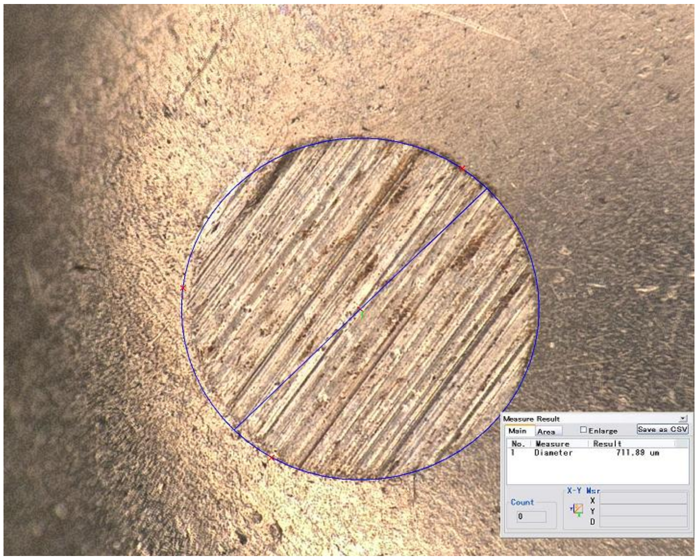

No.	Measure	Result
1	Diameter	711.89 um

Count 0

Figure 81 Magnified image (200X) of an abrasive steel ball used in the wear of GSG-Al at room temperature

Fatigue wear is usually identified by cracks propagating from the wear track, perpendicular to the direction of wear. [115] The mechanism of fatigue wear was not seen to be present since no cracks were propagating in the wear tracks of GSG-Al. The sintering method used to form GSG-Al may be the reason why no fatigue was seen since sintering increases the porosity of the material. Pores inside the material act as buffers that prevent the propagation of cracks much like a circular hole drilled into the end of a crack on an aluminum aircraft wing prevents crack growth. These holes or, in the case of sintered material, pores open the cracks up and reduce the stress concentration factor of the end of the crack. [104] Surface fatigue is not a wear mechanism at this temperature.

Analysis of the wear debris in section 4.8.2.2 revealed that all elements of GSG-Al were a part of the wear debris and their weight percentages were in close agreement with the ratios of the elements that formed GSG-Al. This means that no one element was noticeably worn more than another; however, oxidation of certain elements like Gd, Ge, Fe, and Al was different based upon how easily that material binds with oxygen. [116]

In order to compare GSG-Al with an aluminum alloy, Al 6061-T651 was studied under an optical microscope for signs of different types of wear mechanisms. The sample was first analyzed for wear that occurred at room temperature. An image of three wear tracks is shown in Figure 82 magnified 20X.

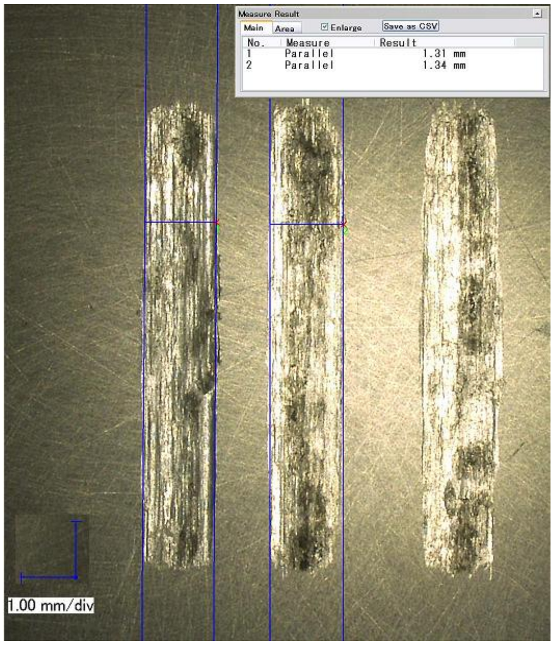

No.	Measure	Result
1	Parallel	1.31 mm
2	Parallel	1.34 mm

Figure 82 Magnified image (20X) of three wear tracks made in a sample of Al 6061-T651 at room temperature

The wear tracks are approximately 8 mm in length and 1.325 mm in width. The tracks are noticeably wider and deeper than the GSG-Al wear tracks made at the same temperature, even to the naked eye. The wear mechanism of abrasion is obvious due to the linear cut marks along the length of the tracks. Also, the wear debris was consistent with this form of wear. Two types of debris were found through the use of the TEM. The TEM found that both small, round, and dark particles existed in the debris as well as large, sharp, and metallic colored particles. The smaller debris was consistent with abrasive wear particles. The sharp wear debris from the aluminum was of a distinct form characteristic of another type of erosion – surface fatigue.

Adhesive wear was detected in traces of the aluminum found on the ball bearing used as the abrasive. The abrasive ball is shown in Figure 83.

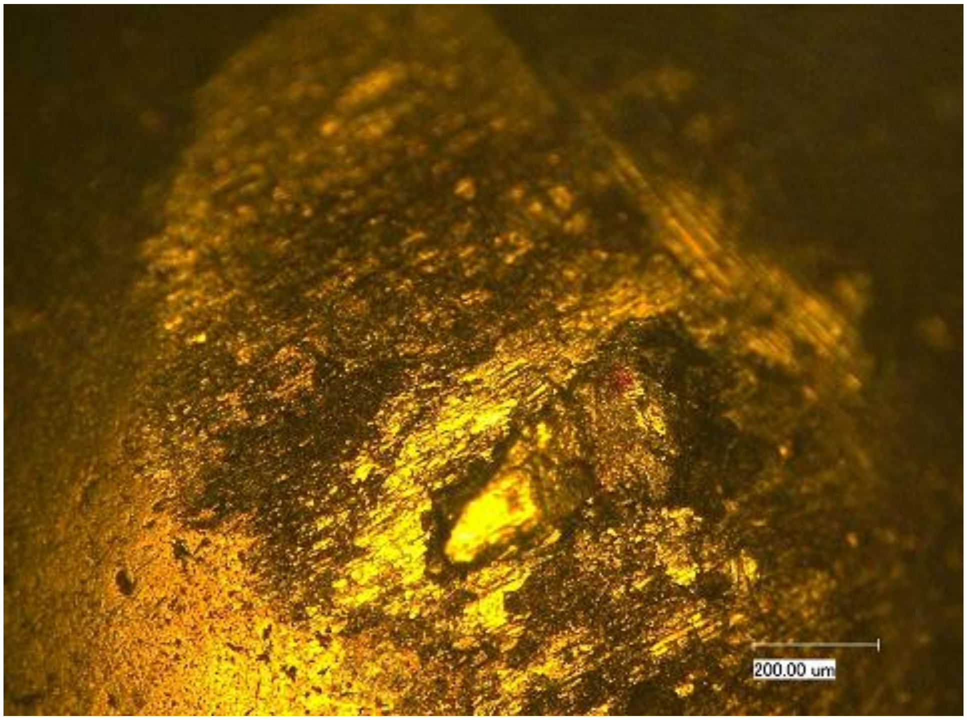

Figure 83 Abrasive ball used to wear a sample of Al 6061-T651 at room temperature with traces of adhered aluminum

Much like the GSG-Al sample, the Al 6061-T651 sample adhered to the steel abrasive ball; the Al 6061-T651did adhere more strongly. While small amounts of GSG-Al particulate were found on the abrasive ball during its wear tests, a considerable amount of aluminum had attached itself to the grooves of the ball and had begun to accumulate. The adhesive wear mechanism was more prominent in the Al 6061-T651 sample meaning that the GSG-Al fares better with this wear mechanism.

In Figure 84, cracks seem to be present (red arrow), however, when the sample is viewed under a higher magnification (200X), the "cracks" are actually shadows made from differing wear track depths.

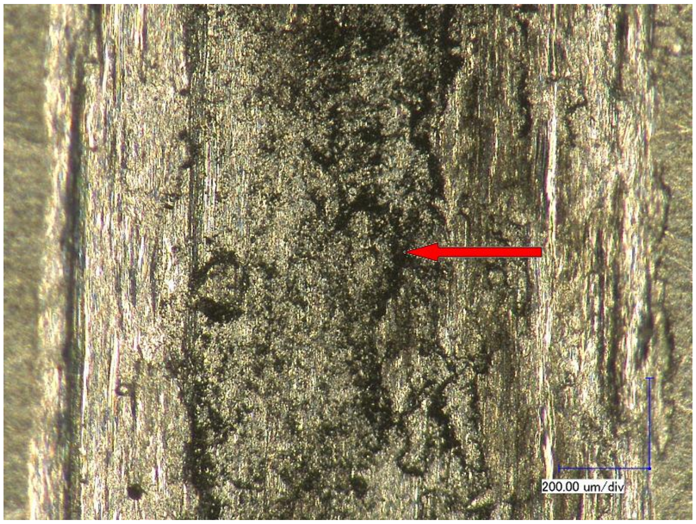

Figure 84 Magnified view (200X) of a wear track of Al 6061-T651
worn at a temperature of 25°C

The image indicates the great inconsistencies in wear depth along the length of the wear track. Flakes were found during the TEM analysis as mentioned in section

4.8.2.2 and are shown in Figure 69. Their presence constitutes the second form of wear debris found in the TEM analysis.

GSG-Al was analyzed for wear mechanisms when the sample was worn at 150°C. Figure 85 shows three wear tracks magnified 150X that appear similar to the wear tracks made at room temperature (**Note:** microscope lighting between Figure 79 and Figure 85 has been altered.)

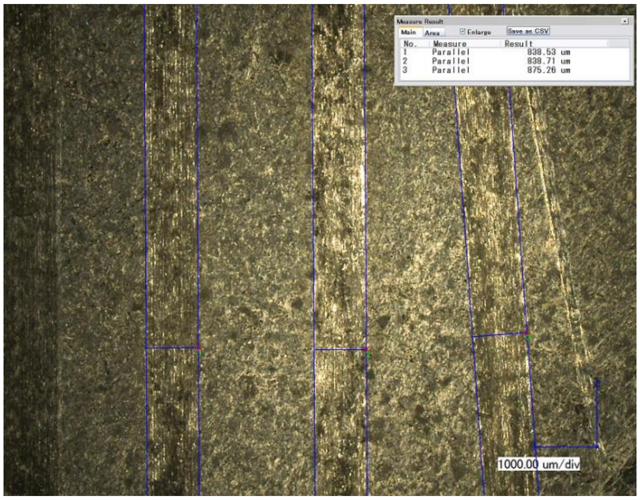

No.	Measure	Result
1	Parallel	838.53 um
2	Parallel	838.71 um
3	Parallel	875.26 um

Figure 85 Magnified image (150X) of three wear tracks in a sample of GSG-Al worn at a temperature of 150°C

The length of the tracks is 8 mm and the width of the tracks was averaged to 850.83 µm. With the dimensions known, the wear tracks can be said to be slightly less worn than tracks at room temperature. The abrasive wear is evident in this sample and appears uniform and consistent across three different tracks. The linear scratches present in the wear tracks make abrasive wear appear to be the most damaging wear mechanism at this high temperature. The presence of adhesive wear can be seen on the ball bearing in Figure 86 magnified 200X.

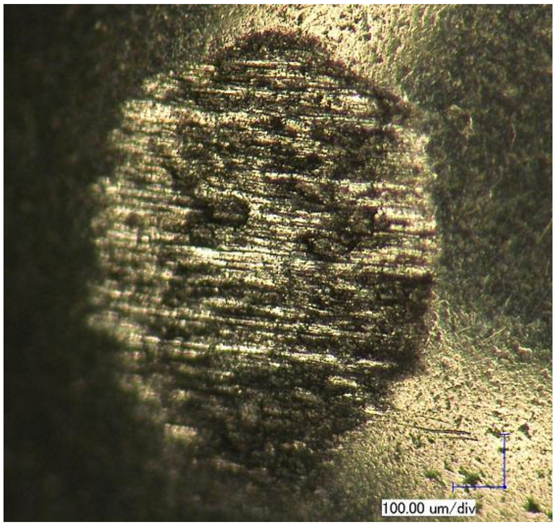

Figure 86 Magnified image (200X) of an abrasive steel ball used to wear a sample of GSG-Al at 150°C

GSG-Al material can be seen built-up as particulate in the darker areas of the abrasive ball image. The lighter areas are abrasive wear lines made in the steel ball by the GSG-Al sample as well as some adhered aluminum phase. GSG-Al particulate did build up on the outer rim of the circular wear scar; however, these particles were loose and easily knocked off. As with the -25°C and 25°C tests, signs of surface fatigue were not seen in the sample of GSG-Al.

When the samples of Al 6061-T651 tested at 150°C were analyzed through a microscope, the results were quite different from the room temperature tests. According to the wear tracks in Figure 87 (multiplied 20X), it can be seen that the wear tracks are far more disordered and inconsistent in their dimensions than the samples worn at a lower temperature.

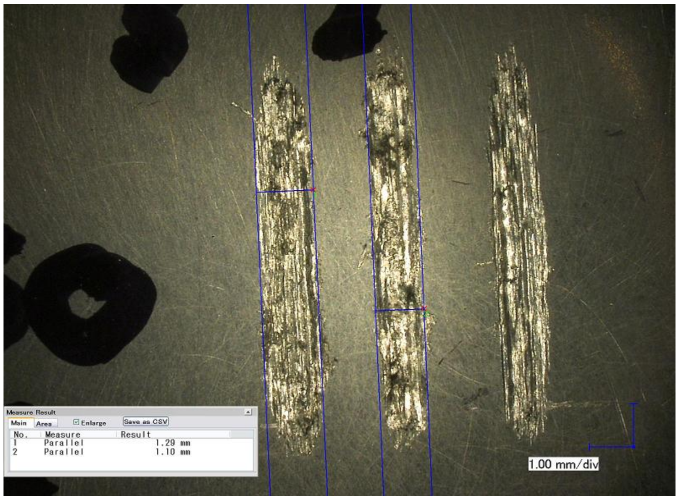

No.	Measure	Result
1	Parallel	1.29 mm
2	Parallel	1.10 mm

Figure 87 Magnified image (20X) of three wear tracks made in a sample of Al 6061-T651 at a temperature of 150°C

As in prior samples and tests, abrasion wear is present due to the formation of linear cut lines along the length of the wear tracks. Adhesive wear, however, was more noticeable and far more detrimental to the overall wear of the material than other previous tests. Figure 88 and Figure 89 show the large amount of wear that occurred as a result of the aluminum adhering to the steel ball bearing (magnified 100X).

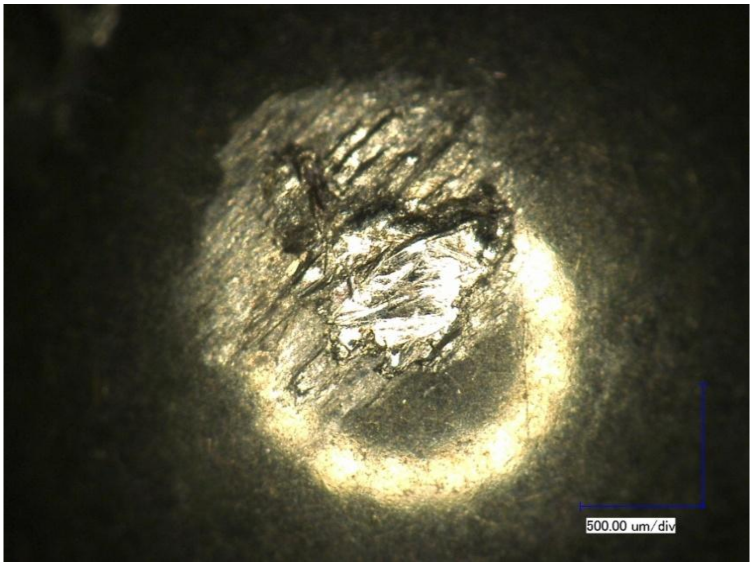

Figure 88 Magnified image (100X) of the abrasive ball used to wear a sample of Al 6061-T651 at a temperature of 150°C with traces of aluminum adhered to its surface

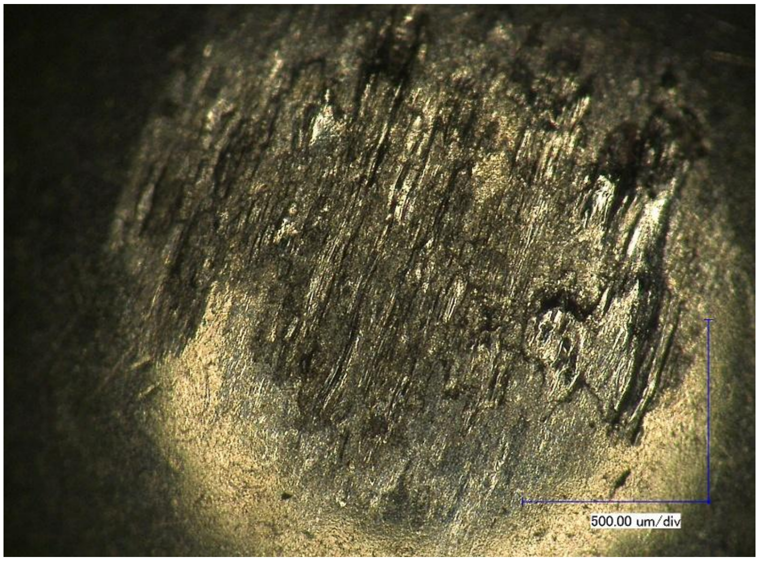

Figure 89 Additional magnified image (100X) of the abrasive ball used to wear a sample of Al 6061-T651 at a temperature of 150°C with traces of aluminum adhered to its surface (broad concentration)

Due to the high irregularities in the wear tracks, cracks were not seen in the material, nor were the plateau-like features seen in the room temperature tests. Debris were formed into flake shaped particulate which suggests that surface underwent cracking as fatigue. The tribometer test at this high temperature resulted in stick- slip. The stick-slip phenomenon is where the adhered rubbing pairs were released to slide over the other. [117] During such a process cracks were developing in the subsurface. Stick-slip was indicated by the jolting motion of the tribometer and confirmed by the adhesion of the aluminum onto the steel ball bearing.

Aluminum is a large constituent element in both samples. It is known that iron has a strong adhesive force to aluminum with a value of 2.5 mN. [102] The adhesive force is a result of the electron transfer and interaction between the materials. So the mating of more noble materials (gold, silver, etc.) would yield a smaller adhesive force. [102] The adhesive force of the iron and aluminum can be said to be comparable to the steel and aluminum interactions in the abrasive ball and sample materials. The adhesive force is affected by the oxide layers and films on the samples and abrasives; thus the forces are reduced. Interfacial interactions between two matting materials are expected to be affected by the contact temperature. In addition, materials behave softer with increased temperature. Softer materials are able to plastically deform easier. As discussed, due to effects of temperature and oxidation, there seem to have three competing mechanisms, the adhesion, softening, and abrasion.

The wear rates behave differently comparing with the coefficient of friction. This is to be expected since friction and wear are not directly related. The mechanisms of wear can influence friction and vice versa in this research due to the fact that the tribo-oxidation is seen for all samples. For the GSG-Al samples, the wear rate decreased gradually as the temperature increased.

As shown in Figure 65, the wear rates of GSG-Al reduce with temperature. With existence of the porosity and the giant strain effects, the composite showed no signs of cracking or fatigue. GSG-Al was less susceptible to adhesive wear than Al 6061-T651with minor adhesion at all temperatures. Overall the GSG-Al composite is superior to the Al alloys in wear resistance. Tests with aluminum alloys have shown a decrease in wear rate with temperature, but eventually reach a point at which the wear rate jumps suddenly due to a strong surge in the adhesive wear. GSG-Al is able to withstand significant adhesion effects up to 150°C, a temperature range typical for common automobile applications.

Al 6061-T651 although harder than GSG-Al experienced far more wear. Al 6061-T651 was prone to high levels of abrasive wear, adhesive wear, and surface fatigue. The detrimental property for Al 6061-T651 was the high surface fatigue. The aluminum alloy suffered from large debris formation due to cracking which only exacerbated the adhesive wear since more particulate was present to adhere to the abrasive's asperities. GSG-Al did not exhibit surface fatigue and thus did not have a significant increase in the adhesive wear. Prior studies with temperature's effect on the wear rate of Al 6061 have indicated similar results in that the wear rate of aluminum was greater at room temperature, began to decrease by a temperature around 50 to 100°C and then increase again by 150°C. Studies of this wear went further with other researchers to include wear temperatures of up to 200°C. [43] It was found in these studies that there is a transition from mild to severe wear between 175°C and 190°C, where there is a large jump in wear rate over the previous temperatures. [43] As with the wear studies of up to 150°C, the higher temperature tests exhibited a strong shift from a dominant abrasive wear mechanism to an adhesive wear mechanism.

The formation of flakes due to fatigue has been previously studied in aluminum alloys. Spalling and pitting can occur due to fatigue as well as a phenomenon known as delamination. Delamination is caused by strain increases in the material due to fatigue. This strain ruptures the aluminum oxide layer and alloys for crack propagation beneath the surface of and parallel to the wear track. [41] The delaminated flakes are then easily adhered to the abrasive ball, which in addition to attributing to surface fatigue, adhesive wear is also increased. Delamination is caused when a critical sliding speed and flash point temperature has been reached. Reaching these points causes a large strain localization effect in the aluminum alloy. [41]

This section discussed the microstructure-property of a new multi-function and mutli-property material GSG-Al. This material was found to be superior in wear resistance to an Al 6061-T651 alloy due to the fact that it was not affected by surface fatigue. The self-healing is unique to Al based alloys. It is also found that there are 2 competing wear mechanisms of this composite attributed by its unique micro and porous structures.

5.6.2.2 Wear Mechanisms

The TEM images of wear debris and EDS results are shown in Figures 66-69 in section 4.8.2.2. This section includes explanations of the shapes and sizes of the debris particulates and explanations. The TEM images of the GSG-Al wear debris at the different temperatures of 25°C, 50°C, and 150°C appear to have some differences. The general shape of the particulate was rounded and lacked sharp corners; however, there does appear to be an increase in particle size as the test temperature increased. The increase in particulate size can be attributed to the adhesive effects as the temperature increases. It is believed that the increasing temperature results in the adhesion between debris particles. This might be due to the oxidation of inclusions. It has been reported that an increasing temperature increased the tendency for adhered particles. [43]

The TEM images, as shown in Figure 69, of the Al 6061-T651 wear debris differ in their view from the GSG-Al wear debris. While GSG-Al debris tended to be more rounded in its shape, the Al 6061-T651 debris had instances of larger, sharp cornered, metallic colored debris along with darker, rounded debris. The darker debris have been studied in prior research as having greater amounts of oxygen and iron (from abrasive) in addition to the aluminum in their EDS studies while the flake-like debris had lower traces of oxygen and no noticeable iron. [41] The flake-like debris is characteristic of that formed from spalling or flake fatigue. This type of flaking can be caused by delamination of the aluminum due to fatigue and crack formation that is parallel to the wear surface. [41] The existence of a brittle oxide (Al_2O_3) and low endurance limits enhance the formation of these flakes. Prior testing by Wilson and Alpas in regarding lamination in other aluminum alloys indicated that delamination of aluminum increased greatly once the critical flash temperature and critical wear velocity had been surpassed. [41] The absence of these large flakes in the GSG-Al wear debris is one of the unique characteristics. The GSG-Al sample wears as small particles are removed through abrading. This subsequently affected the wear rate as compared with the Al 6061-T651 samples.

EDS analysis of the elements, shown in Figure 70, found in GSG-Al wear debris at the wear temperatures of 25, 50, and 150°C yielded the relative weight percentages elements Gd, Al, Ge, Si, O, and Fe. The elements with the greatest weight percentages across all temperatures are Al, Gd, and O. The appearance of oxygen in the EDS and in such a great quantity indicates that the wear debris of GSG-Al was highly oxidized during wear. The oxide layer that formed during the wear tests and the oxidation of the wear debris are the only known sources of oxygen for the sample. Iron was also detected in the samples in small amounts at temperatures of 25°C and 50°C, but in large amounts at the wear temperature of 150°C. The iron element originates from the steel used as the abrasive in the wear tests. There was a sudden jump in iron weight percentage at 150°C. An explanation could be that the oxidation of iron at this high temperature is greatly enhanced, meaning that more elemental iron was oxidized during wear. Aluminum and iron both are strongly attracted to oxygen with Al forming the oxide Al_2O_3 and iron forming the oxide Fe_2O_3. Gd and Ge also have oxides and high attraction to oxygen. Binding enthalpy or bond energy is the amount of energy required per mole of material to separate one atom from another. The elements of Al, Fe, and Ge all have multiple oxidation states, but Gd has only one. The elements readily form bonds with oxygen; gadolinium has the strongest binding enthalpy to oxygen at 719 kJ/mol, followed by germanium at 659.4 kJ/mol, aluminum with a value of 511 kJ/mol, and iron's binding enthalpy is less with a value of around 390 kJ/mol. [116] The oxygen detected by the EDS could have been attracted to any of these elements to form oxides; however, aluminum and gadolinium are the highest producers due the mass of each element in the sample.

CHAPTER VI

CONCLUSIONS AND FUTURE RECOMMENDATIONS

Experimental investigations of new class of composite materials were conducted in the thesis research. Detailed characterization and analysis were carried to understand their properties and performance and to evaluate their potential applications in automobiles. This chapter firstly highlights the major discoveries and the conclusions that have been made regarding the GSG-Al composite. The physical, mechanical, thermal, magnetic, and wear properties of the composite material have been studied and many interesting and noteworthy discoveries have been made. It will then end with future recommendations and impacts statement.

6.1 Discoveries and Conclusions

A new class of composite materials was developed that has a multi-structure and multi-functions. Analysis of the composite formed from GSG and Al has provided insights and opened new ground to future of composite materials. The intention of this research was to design a structurally stable material that exhibits the giant strain effect for use in the automobile industry and other structural applications. The major conclusions are listed in the following:

(1) The GSG-Al that was developed has multiple crystal structures due to the sintering process. The aluminum phases have a face centered cubic structure, the GSG phases have a monoclinic crystal structure above its Curie temperature and an orthorhombic crystal structure below, and GdAlGe

exhibits an α-ThSi-type tetragonal crystal structure at high temperatures and a YAlGe-type orthorhombic structure at low temperatures.

(2) GSG-Al has an average hardness value of 33.5 in the superficial Rockwell 30-T scale. The hardness value indicates that GSG-Al is a soft and ductile material that is less likely to crack from strain.

(3) At a temperature of 0°C (273 K), the thermal expansion coefficient was 7.4E-3/°C indicating a large jump in thermal expansion when compared to the room temperature value. This property indicates a significant phase change within GSG-Al's micro-structure.

(4) Under thermal stress concentration, the GSG-Al does not present any cracking. This was due to the giant strain effects that healed the cracks.

(5) GSG-Al was found to have good wear resistance especially when compared to Al 6061-T651. The wear rates of the sample are almost seven times lower than that of Al 6061-T651 at a certain temperature. The wear rates continuously decrease as the temperature increases up until 150°C (423 K).

(6) Wear for GSG-Al is primarily controlled by abrasive wear which is the dominant form at all temperatures studied. Adhesive wear increased with temperature, yet was still minor; however, wear at -25°C (248 K) is the exception to this trend due to moisture on the sample

(7) The coefficient of friction for GSG-Al varies with temperature and is greater than those of Al 6061-T651 at all temperatures studied, but they are relatively close in their values. The higher friction is attributed to the softness of the

GSG-Al compared to Al 6061-T651. The softness of the GSG-Al alloys is due to its metallic consistency as well as to the sintering process that formed the composite.

The significant discoveries were the rapid thermal expansion that occurred within the low temperature range and the material's good wear properties. Alterations to the sample need to be done and investigations into how to maintain the magnetocaloric effect need to be of the utmost priority in future work with this sample. The rapid expansion at low temperatures; however, may be found to be useful in automobile applications.

6.2 Future Recommendations

A new composite GSG-Al was developed in this research. In order to further develop it with magnetocaloric behavior, there are several steps to be taken for future research.

(1) Studies should be made of the effects of the ratio of GSG to Al on its properties.

(2) Aluminum was chosen as a matrix material due to its paramagnetic behavior, ductility, and high strength to weight ratio. Other materials such as titanium should be used as the primary matrix material in order to observe any potential benefits.

(3) An in situ method studying the phase transformation of GSG over time using XRD is recommended for fundamental study.

(4) Characterization in magnetocaloric effect, such as magnetic and thermal fatigue experiments could be conducted.

This research developed a new class of composite materials that have unique combination of structures and properties. Particularly, the giant strain effects inside the aluminum matrix made the material highly self-healable and highly wear resistant. It brings new approaches in materials design for engineering applications such as automobile power generation and self-sealing crack technology. The research opens new windows of investigation for fundamental studies in phase transfer and multi-structure-properties. This material is expected to attract great attention in the next few years.

REFERENCES

1 N. A. Otto; *Vol. 388372*, edited by U. S. P. Office (United States, 1888).

2 M. Gumus, M. Atmaca, and T. Yimaz, International Journal of Energy Research **33,** 745 (2009).

3 J. Yang and Ieee, *Potential applications of thermoelectric waste heat recovery in the automotive industry* (2005).

4 J. P. Bowman, S. S. Krishnan, R. Nalim, and Asme, *Cooling challenges of modern truck diesel engines* (Amer Soc Mechanical Engineers, New York, 2005).

5 H. Q. Xie, W. Yu, and Y. Li, Journal of Physics D-Applied Physics **42** (2009).

6 Elena Timofeeva, David Smith, Wenhua Yu, a. Jules Routbort, and D. Singh, (United States Department of Energy Laboratory and Argonne National Laboratory, 2009).

7 B. T. Liu, K. H. Chien, and C. C. Wang, Energy **29,** 1207 (2004).

8 A. Schuster, S. Karellas, E. Kakaras, and H. Spliethoff, Applied Thermal Engineering **29,** 1809 (2009).

9 S. Ayyash, Energy Conversion and Management **21,** 163 (1980).

10 I. Kotcioglu, S. Caliskan, and E. Manay, Isi Bilimi Ve Teknigi Dergisi-Journal of Thermal Science and Technology **29,** 109 (2009).

11 E. Samadiani, A. Kakaee, and Asme, *An analytical model to simulate the automotive cooling system* (Amer Soc Mechanical Engineers, New York, 2005).

12 B. Gosolits, R. M. Visinescu, M. Weil, and Vdi, in *Simvec - Numerical Analysis and Simulation in Vehicle Engineering 2008*; *Vol. 2031* (V D I-V D E - Verlag Gmbh, Dusseldorf, 2008), p. 665.

13 A. G. Fedorov and J. M. Meacham, Ieee Transactions on Components and Packaging Technologies **32,** 746 (2009).

14 M. L. M. Simon C. Tung, Tribology International **37,** 517 (2004).

15 U. A. Ming Zheng, Graham T. Reader, Yuyu Tan, Meiping Wang, International Journal of Energy Research **33,** 8 (2009).

16 P. S. J.R.F. Lillywhite, S.B. Saville, Industrial Lubrication and Tribology **42,** 4 (1990).

17 Y. N. Murakami, Kiyotaka; Aihara, Hisamoto, Transactions of the Japan Society of Mechanical Engineers, Part B **56,** 1536 (1990).

18 P. E. Ane M. García-Romero, Angel M. Irisarri, Applied Composite Materials **17,** 15 (2010).

19 V. Angileri, R. Bonavolonta, M. Durando, M. Garganese, G. V. Mariotti, and Asme, *FE calculation methodology for the thermomechanic fatigue analysis of an engine component* (2006).

20 S. U. S. C. Seok Pil Jang, Applied Thermal Engineering **26,** 2457 (2006).

21 C. Wood, Reports on Progress in Physics **51,** 459 (1988).

22 J. H. C. T.C. Harman, M.J. Logan, Journal of Applied Physics **30,** 1351 (1958).

23 H. K. Akio Fukushima, Atsushi Yamamoto, Yoshishige Suzuki, Shinji Yuasa, Ieee Transactions on Magnetics **41,** 2571 (2005).

24 R. E. Sonntag, G. J. Van Wylen, and C. Borgnakke, *Fundamentals of thermodynamics*, 7th ed. (Wiley;John Wiley [distributor], Hoboken, N.J. Chichester, 2008).

25 A. G. Iacopo Vaja, Energy **35,** 1084 (2010).

26 K.-H. C. Bo-TauLiu, and Chi-Chuan Wang, Energy **29,** 1207 (2004).

27 T. C. Hung, Energy Conversion and Management **42,** 539 (2001).

28 J. Soderman and P. Ahtila, Applied Thermal Engineering **30,** 15 (2010).

29 Y. P. Dai, J. F. Wang, and L. Gao, Energy Conversion and Management **50,** 576 (2009).

30 S. Quoilin, V. Lemort, and J. Lebrun, Applied Energy **87,** 1260 (2010).

31 E. Cayer, N. Galanis, and H. Nesreddine, Applied Energy **87,** 1349 (2010).

32 S. V. a. G. Gould, in *Burns & McDonnell: Tech Briefs*.

33 M. Yari, International Journal of Exergy **6,** 323 (2009).

34 G. E. T. D. Scott MacKenzie, *Analytical Characterization of Aluminum, Steel, and Superalloys* (CRC Press, Boca Raton, FL, 2006).

35 C. M. Taylor, Wear **221,** 1 (1998).

36 A. Edrisy, T. Perry, and A. T. Alpas, Wear **259,** 1056 (2005).

37 F. S. Silva, Engineering Failure Analysis **13,** 480 (2006).

38 Z. W. Yu, X. L. Xu, and H. X. Ding, Engineering Failure Analysis **14,** 110 (2007).

39 T. P. A. Edrisy, A.T. Alpas, Wear **259,** 1056 (2005).

40 B. D. J. Jeong Hwan Jang, Jae Ho Lee, Young Hoon Moon, Metallic Materials International **15,** 903 (2009).

41 A. T. A. S. Wilson, Wear **225,** 440 (1999).

42 J. Lei, N. Li, and M. C. Rao, in *Engineering Materials Iii*; *Vol. 51*, edited by Y. J. Lin and W. C. J. Wei (Trans Tech Publications Ltd, Stafa-Zurich, 2008), p. 105.

43 A. T. A. S. Wilson, Wear **196,** 270 (1996).

44 A. M. Garcia-Romero, P. Egizabal, and A. M. Irisarri, Applied Composite Materials **17,** 15 (2010).

45 Y. Z.-x. S. B.-y. D. W.-j. C. Yu-guo, Journal of Dalian University of Technology **45,** 45 (2005).

46 S. J. M. R. C. O'Handley, M. Marioni, H. Nembach, and S. M. Allen, Journal of Applied Physics **87,** 4712 (2000).

47 S. W. O. Nersesse Nersessian, Gregory P. Carman, Scott K. McCall, Wonyoung Choe, Harry B. Radousky, Mike W. McElfresh, Vitalij K. Pecharsky, Alexander O. Pecharsky, , Applied Physics Letters **84,** 4801 (2004).

48 M. Han, J. A. Paulsen, J. E. Snyder, D. C. Jiles, T. A. Lograsso, and D. L. Schlagel, Ieee Transactions on Magnetics **38,** 3252 (2002).

49 D. C. J. M. Han, J.E. Snyder, T.A. Lograsso, D.L. Schlagel, Journal of Applied Physics **95,** 6945 (2004).

50 S. T. N. Kazuki Omoto, Steve Hull, Akimitsu Aoto, Takuya Hashimoto Journal of Solid State Chemistry **183,** 392 (2010).

51 S. T. O. Sigmund, Applied Physics Letters **69,** 3203 (1996).

52 T. B. P. Piskunowicz, T. Wolejko, Phys. Stat. Sol. **114,** 505 (1989).

53 K. A. J.J. Neumeier, K.J. McClellan, Physical Review B **59,** 1701 (1999).

54 H. D. Megaw, Materials Research Bulletin **6,** 1007 (1971).

55 D. C. J. M. Han, J.E. Snyder, T.A. Lograsso, D.L. Schlagel, Journal of Applied Physics **95,** 6945 (2004).

56 J. V. K. Pecharsky and K. A. Gschneidner, Physical Review Letters **78,** 4494 (1997).

57 A. A. L. A. Sozinov, N. Lanska, K. Ullakko, Applied Physics Letters **80,** 1746 (2002).

58 J.-M. B. Robert Dunsch, Sensors and Actuators A **134,** 436 (2007).

59 I. C. Jayant Sirohi, JOURNAL OF INTELLIGENT MATERIAL SYSTEMS AND STRUCTURES **11,** 246 (2000).

60 T. R. S. Seung-Eek Park, Journal of Applied Physics **82,** 1804 (1997).

61 X. S. G. Z. H. Zhou., John Wang, K. Fujihara, S. Ramakrishna, V.Nagarajan, Applied Physics Letters **90** (2007).

62 Y. K. B. Kim, J.M.; Son, S.Y.; Choi, J.H.; Kim, S.G., 3rd International Conference on Micro Opto Electro Mechanical Systems (Optical MEMS). MOEMS 99. Proceedings**,** 107 (1999).

63 J. D. V. Leo Christodoulou, Journal of the Minerals: Metals and Materials Socirty **55,** 1543 (2003).

64 J.-Z. R. Zhang, Bao-Guo; Wang, Ze-Shen; Zheng, Hai-Shan, Journal of Astronautics **29,** 644 (2008).

65 A. K. Pramanick and P. K. Das, International Journal of Heat and Mass Transfer **49,** 1420 (2006).

66 e. a. Francis J. DiSalvo, Science **285,** 703 (1999).

67 H. A. Bao Yang, Thanh N. Tran, HVAC & R Research **14,** 635 (2008).

68 D. M. Rowe, IEEE Reviews **125,** 1113 (1978).

69 L. I. L. Anatychuk, O.J., Proceedings ICT'03. 22nd International Conference on Thermoelectrics 491 (2003).

70 A. I. Hochbaum, R. K. Chen, R. D. Delgado, W. J. Liang, E. C. Garnett, M. Najarian, A. Majumdar, and P. D. Yang, Nature **451,** 163 (2008).

71 L. G. Chen, J. Z. Gong, F. R. Sun, and C. Wu, International Journal of Thermal Sciences **41,** 95 (2002).

72 R. Y. Nuwayhid and F. Moukalled, Energy Conversion and Management **44,** 647 (2003).

73 A. N. Society, Nuclear News **46,** 34 (2003).

74 Amerigon, (Nasdaq.com, Northville, MI, 2009).

75 H. T. Chua, K. C. Ng, X. C. Xuan, C. Yap, and J. M. Gordon, Physical Review E **65** (2002).

76 in *TE Technology Inc.: Thermoelectic Modules*; *Vol. 2010*, edited by I. TE Technology (Traverse City, Michigan, 2010).

77 A. Taylor, Energy Policy **36,** 4657 (2008).

78 H. J. Goldsmid, Applied Physics **9,** 365 (1958).

79 L. G. Chen, J. Li, F. R. Sun, and C. Wu, Applied Energy **82,** 300 (2005).

80 N. Lior, Energy Conversion and Management **43,** 1187 (2002).

81 M. Chen, L. Rosendahl, I. Bach, T. Condra, and J. Pedersen, American Journal of Physics **75,** 815 (2007).

82 K. A. Gschneidner, V. K. Pecharsky, and A. O. Tsokol, Reports on Progress in Physics **68,** 1479 (2005).

83 E. Brueck.

84 K. A. Gschneidner and V. K. Pecharsky, International Journal of Refrigeration-Revue Internationale Du Froid **31,** 945 (2008).

85 P. M. P. Kamasa, Czechoslovak Journal of Physics **52,** 159 (2002).

86 K. Gibson, in *U.S. Department of Energy: Research News* (U.S. Department of Energy).

87 K. A. G. J. V. K. Pecharsky, Advanced Materials **13,** 683 (2001).

88 H. Tang, V. K. Pecharsky, G. D. Samolyuk, M. Zou, K. A. Gschneidner, Jr., V. P. Antropov, D. L. Schlagel, and T. A. Lograsso, Phys Rev Lett **93,** 237203 (2004).

89 M. M. R. D.M. Raj Kumar, R. Gopalan, R. Balamuralikrishnan, A.K. Singh, V. Chandrasekaran, Journal of Alloys and Compounds **461,** 14 (2008).

90 Y. C. Tiebang Zhang, Baohua Teng, Yonggai Tang, Hao Fu, Mingjing Tu, Materials Letters **61,** 440 (2007).

91 G. Chelkowska, Journal of Magnetism and Magnetic Materials **127,** L37 (1993).

92 G. Chelkowska, Journal of Alloys and Compounds **209,** 337 (1994).

93 A. S. f. Metals., *Metals Handbook: Properties and Selection: Nonferrous Alloys and Special-Purpose Materials*, Vol. 2 (ASM International, 1990).

94 S. D. E. Wakil, *Processes and Design for Manufacturing* (Waveland Press, Inc., 1998).

95 J. William D. Callister, *Materials Science and Engineering: An Introduction*, 7th ed. (John Wiley & Sons, Inc., New York, NY, 2007).

96 J. L. L. Zhong Lin Wang, in *Developments in Surface Contamination and Cleaning: Fundamentals and Applied Aspects*, edited by K. L. M. Rajiv Kohli (William Andrew, Inc., Norwich, NY, 2008), p. 531.

97 M. K. B. Kenneth G. Budinski, *Engineering Materials: Properties and Selection*, 8th ed. (Pearson Education, Inc., Upper Saddle River, NJ, 2005).

98 A. International.

99 A. International.

100 D. P. D. Frank P. Incropera, Theodore L. Bergman, Adrienne S. Lavine, *Fundamentals of Heat and Mass Transfer*, 6th ed. (John Wiley & Sons, Inc., Hoboken, NJ, 2007).

101 L. L. K. Gramm, O. Beckman, Physica Scripta **13,** 93 (1976).

102 G. W. Stachowiak and A. W. Batchelor, *Engineering tribology*, 3rd ed. (Elsevier Butterworth-Heinemann, Amsterdam ; Boston, 2005).

103 N. Z. N. E.I. Gladyshevskii, K. Cenzual, R.E. Gladyshevskii, and J.-L. Jorda, Journal of Alloys and Compounds **296,** 265 (1999).

104 Y. L. S. P.S. Song, International Journal of Fatigue **26,** 1333 (2004).

105 I. O. f. Standardization, (2002).

106 R. L. Norton, *Machine Design: An Integrated Approach*, 3rd ed. ed. (Pearson/Prentice Hall, Upper Saddle River, N.J., 2006).

107 Z.-M. W. Ding, Shu-Juan; Shen, Chang-Bin; Chen, Kai-Min; Gao, Hong; Li, Bao-Liang Tribology **29,** 447 (2009).

108 W. J. T. A.J.W. Moore, Mathematical and Physical Sciences **212,** 452.

109 T. K. C. P. N. Bindumadhavan, M. Chandrasekaran, Heng Keng Wah, Loh Nee Lam, O. Prabhakar, Materials Science and Engineering A-Structural Materials Properties Microstructure and Processing **315,** 217 (2001).

110 L. Wang, Y. He, J. Zhou, and J. Duszczyk, Tribology International **42,** 15 (2009).

111 C. Kang and N. S. Eiss, Wear **181,** 94 (1995).

112 W. G. S. L. P. H. Jeurgens, F. D. Tichelaar, and E. J. Mittemeijer, Journal of Applied Physics **92** (2002).

113 J. D. D. Bressan, D.P.; Sokolowski, A.; Mesquita, R.A.; Barbosa, C.A., 205 **1-3** (2008).

114 S. K. Hanim, J.R., International Journal of Impact Engineering **22,** 649 (1999).

115 S. H. S. Kang, T.1; Kato, Y.; Jeong, H.S. , Surface Engineering **17,** 498 (2001).

116 J. A. Kerr, *CRC Handbook of Chemistry and Physics 1999 -2000: A Ready-Reference Book of Chemical and Physical Data*, 81st ed. (CRC Press, Boca Raton, FL, 2000).

117 S. L. V. Zhang, J.M., Tribology Letters **12,** 195 (2002).

VITA

Name: Brady Curtis Barkley

Address:
Department of Mechanical Engineering
c/o Dr. Hong Liang
Texas A&M University
College Station, TX 77843-3123

Email Address: brady.barkley@gmail.com

Education:

M.S., Mechanical Engineering, Texas A&M University, 2010
B.S., Mechanical Engineering, Summa Cum Laude, Oklahoma Christian University, 2008

Employment:

Teaching Assistant, *Engineering Technology Program, Texas A&M*
Office Assistant, *Mechanical Engineering Office, Texas A&M*
Teaching Assistant, *Mechanical Engineering Program, Texas A&M*
Program Management Assistant, *Recaro Aircraft Seating*, Fort Worth, TX
U.S. Congress Intern, *U.S. Congressman Pete Sessions*, Washington D.C.